

Giant Clumps in Simulated High- z Galaxies: Properties, Evolution and Dependence on Feedback

Nir Mandelker^{1*}, Avishai Dekel¹, Daniel Ceverino², Colin DeGraf^{1,3}, Yicheng Guo⁴, Joel Primack⁵

¹Center for Astrophysics and Planetary Science, Racah Institute of Physics, The Hebrew University, Jerusalem 91904, Israel

²Universität Heidelberg, Zentrum für Astronomie, Institut für Theoretische Astrophysik, Albert-Ueberle-Str. 2, 69120 Heidelberg, Germany

³Institute of Astronomy and Kavli Institute for Cosmology, University of Cambridge, Madingley Road, Cambridge CB3 0HA, UK

⁴UCO/Lick Observatory, Department of Astronomy and Astrophysics, University of California, Santa Cruz, CA, USA

⁵Department of Physics, University of California, Santa Cruz, CA 95064, USA

ABSTRACT

We study the evolution and properties of giant clumps in high- z disc galaxies using AMR cosmological simulations at redshifts $z \sim 6 - 1$. Our sample consists of 34 galaxies, of halo masses $10^{11} - 10^{12} M_{\odot}$ at $z = 2$, run with and without radiation pressure (RP) feedback from young stars. While RP has little effect on the sizes and global stability of discs, it reduces the amount of star-forming gas by a factor of ~ 2 , leading to a similar decrease in stellar mass by $z \sim 2$. Both samples undergo extended periods of violent disc instability (VDI) continuously forming giant clumps of masses $10^7 - 10^9 M_{\odot}$ at a similar rate, though RP significantly reduces the number of long-lived clumps (LLCs). When RP is (not) included, clumps with circular velocity $\lesssim 40$ (20) kms^{-1} , baryonic surface density $\lesssim 200$ (100) $M_{\odot} \text{pc}^{-2}$ and baryonic mass $\lesssim 10^{8.2}$ ($10^{7.3}$) M_{\odot} are short-lived, disrupted in a few free-fall times. More massive and dense clumps survive and migrate toward the disc centre over a few disc orbital times. In the RP simulations, the distribution of clump masses and star-formation rates (SFRs) normalized to their host disc is similar at all redshifts, exhibiting a truncated power-law with a slope slightly shallower than -2 . The specific SFR (sSFR) of the LLCs declines with age as they migrate towards the disc centre, producing gradients in mass, stellar age, gas fraction, sSFR and metallicity that distinguish them from the short-lived clumps which tend to populate the outer disc. Ex situ mergers comprise $\sim 37\%$ of the mass in clumps and $\sim 29\%$ of the SFR. They are more massive and with older stellar ages than the in situ clumps, especially near the disc edge. Roughly half the galaxies at redshifts $z = 4 - 1$ are clumpy, with $\sim 3 - 30\%$ of their SFR and $\sim 0.1 - 3\%$ of their stellar mass in clumps.

Key words: cosmology — galaxies: evolution — galaxies: formation — galaxies: kinematics and dynamics — stars: formation

1 INTRODUCTION

The phase of galaxy formation is at redshifts $z = 1 - 4$, when star-formation is at its peak and most of the mass is assembled into galaxies (Madau, Pozzetti & Dickinson 1998; Hopkins & Beacom 2006; Madau & Dickinson 2014). Observations of massive star-forming galaxies (SFGs) of $\sim 10^{11} M_{\odot}$ in baryons at this epoch reveal high star-formation rates (SFRs) of order $100 M_{\odot} \text{yr}^{-1}$

(Genzel et al. 2006; Förster Schreiber et al. 2006; Elmegreen et al. 2007; Genzel et al. 2008; Stark et al. 2008). A large fraction of these galaxies have been spectroscopically confirmed to be rotating discs (Genzel et al. 2006; Shapiro et al. 2008; Förster Schreiber et al. 2009; Wisnioski et al. 2015). They are perturbed, thick and turbulent, with high velocity dispersions of $\sigma \sim 20 - 80 \text{kms}^{-1}$, and low rotation to dispersion ratios of $V/\sigma \sim 2 - 7$, as opposed to $10 - 20$ in today's spiral galaxies (Elmegreen & Elmegreen 2005; Genzel et al. 2006; Förster Schreiber et al. 2006, 2009; Cresci et al. 2009). Estimates of their gas fractions from CO

* E-mail: nir.mandelker@mail.huji.ac.il

measurements are in the range 0.2 – 0.8 (Daddi et al. 2010; Tacconi et al. 2010, 2013; Genzel et al. 2015), much higher than the fractions of 0.05 – 0.1 in today’s discs (Saintonge et al. 2011). Many of these galaxies exhibit irregular morphologies, in both rest-frame UV and rest-frame optical emission (Genzel et al. 2008; Förster Schreiber et al. 2009, 2011), with much of the UV light concentrated in a few large “clumps”, each a few percent of the disc mass and on the order of a kpc in size, much larger than the star-forming complexes observed in local galaxies. Recent observations of over 3000 galaxies in the *Cosmic Assembly Near-IR Deep Extragalactic Legacy Survey* (CANDELS, Grogin et al. 2011; Koekemoer et al. 2011) reveal that roughly 60% of the SFGs at $z \gtrsim 2$ are clumpy, with clumps accounting for ~ 20 –40% of their UV light and $\gtrsim 10\%$ of their SFR (Guo et al. 2015).

According to our developing theoretical framework of high redshift galaxy formation, these SFGs are in a perpetual state of violent-disc-instability (VDI, Dekel, Sari & Ceverino 2009). Intense inflow of cold gas in narrow streams along the filaments of the cosmic web (Birnboim & Dekel 2003; Kereš et al. 2005; Dekel & Birnboim 2006; Ocvirk, Pichon & Teyssier 2008; Dekel et al. 2009) maintains high gas fractions throughout the disc, replenishing losses to star-formation, outflows, and compaction events which drive large amounts of gas into the disc centre (Bournaud et al. 2011; Forbes et al. 2014; Dekel & Burkert 2014; Zolotov et al. 2015; Tacchella et al. 2016a,b). The high gas fraction together with the high density in the early Universe, leads to a violent gravitational disc instability (Toomre 1964), which involves giant clumps and operates on short, orbital timescales (Dekel, Sari & Ceverino 2009; Ceverino, Dekel & Bournaud 2010), as opposed to the slow, secular instability in today’s discs.

The basic idea, summarized in Dekel, Sari & Ceverino (2009), is that during VDI the high surface density of gas and “cold” young stars, Σ , drives the Toomre Q parameter below unity, $Q \sim \sigma\Omega/(\pi G\Sigma) \lesssim 1$, where σ is the one-dimensional velocity dispersion and Ω is the angular frequency, a proxy to the epicyclic frequency κ , which is related to the potential well (Toomre 1964). It has been established that under such conditions the disc will fragment and produce large star-forming clumps. This has been shown using idealized simulations of isolated galaxies (Noguchi 1999; Gammie 2001; Immeli et al. 2004a,b; Bournaud, Elmegreen & Elmegreen 2007; Bournaud & Elmegreen 2009; Elmegreen, Bournaud & Elmegreen 2008; Hopkins et al. 2012), as well as cosmological simulations (Agertz, Teyssier & Moore 2009; Ceverino, Dekel & Bournaud 2010; Ceverino et al. 2012; Genel et al. 2012; Mandelker et al. 2014; Oklopčić et al. 2016). The ratio of clump mass to the mass of the cold disc scales as $M_c/M_d \propto \delta^2$, where $\delta = M_d/M_{\text{tot}}$ is the ratio of the cold disc mass to the total mass within the disc radius, which includes the bulge and dark matter halo

(e.g. Dekel, Sari & Ceverino 2009). This leads to much larger clumps at $z \sim 2$ than the low-redshift giant molecular clouds (GMCs). Gravitational interactions in the perturbed disc drive turbulence causing the disc to self-regulate in a marginally stable state with $Q \lesssim 1$ (Dekel, Sari & Ceverino 2009; Ceverino, Dekel & Bournaud 2010; Krumholz & Burkert 2010; Cacciato, Dekel & Genel 2012; Forbes, Krumholz & Burkert 2012; Forbes et al. 2014) that can last for more than a Gyr so long as the accretion is not interrupted. Some recent works have called into question the validity of linear Toomre analysis in the context of these highly non-linear galaxies (Behrendt, Burkert & Schartmann 2015; Tamburello et al. 2015; Inoue et al. 2016) and others have suggested alternate fragmentation mechanisms related to turbulence (e.g. Hopkins 2013). However, since clump formation is largely determined by the balance between self-gravity, turbulent pressure and the centrifugal force, the largest clumps are always roughly at the Toomre scale. Larger clumps would be disrupted due to the shear and/or tidal forces within the disc, or would not collapse in the first place due to the centrifugal force. Therefore, regardless of the full validity of linear Toomre analysis, it is plausible that the Toomre Q parameter can serve as a crude criterion for instability, possibly with a critical value that is larger than unity.

If clumps survive stellar feedback, their large masses cause them to migrate to the galactic centre on short timescales of $\sim 2 - 3$ orbital times at the disc edge (Dekel, Sari & Ceverino 2009; Ceverino et al. 2012; Bournaud et al. 2014; Mandelker et al. 2014). This was proposed as a mechanism for the formation of galactic spheroids, in parallel with the traditional merger scenario (Bournaud, Elmegreen & Elmegreen 2007; Elmegreen, Bournaud & Elmegreen 2008; Genzel et al. 2008; Dekel, Sari & Ceverino 2009; Ceverino et al. 2015) and the fueling of a central AGN (Bournaud et al. 2011, 2012). However, simulations show that most of the gas inflowing to the galactic centre is in fact inter-clump gas (e.g. Hopkins et al. 2012; Zolotov et al. 2015). Indeed, wet inflows to the galactic centre induced by gravitational torques are a generic feature of VDI, not necessarily associated with clump migration (Krumholz & Burkert 2010; Forbes, Krumholz & Burkert 2012; Forbes et al. 2014; Dekel & Burkert 2014). While clump migration can contribute to the dry growth of the bulge, cosmological simulations indicate that this contribution is limited to $\lesssim 25\%$ of the bulge mass at $z \sim 2$ (Zolotov et al. 2015). Nevertheless, the giant clumps themselves, their properties, and their evolution, are all major observational indicators of VDI. Clump migration is related to the overall inflow, and if signatures of this migration are observed, they would indicate the validity of VDI and VDI-driven gas inflow.

There is much debate regarding the ability of these giant clumps to survive feedback. Based on rather crude arguments, massive clumps of $M_c \gtrsim 10^8 M_\odot$ are not expected to be disrupted by supernova feedback alone

(Dekel, Sari & Ceverino 2009; Ceverino, Dekel & Bournaud 2010; Ceverino et al. 2012; Bournaud et al. 2014; Mandelker et al. 2014). However, winds are observed from giant high- z clumps (Genzel et al. 2011; Newman et al. 2012), with mass loading factors of order unity. If these outflows are very intense on timescales of $\sim 1-2$ free fall times, they could lead to significant mass loss and maybe even disruption of the clump (Genel et al. 2012; Hopkins et al. 2012). Murray, Quataert & Thompson (2010) argued that the high- z clumps are likely to be disrupted by momentum driven feedback, similar to GMCs at low redshift, but Krumholz & Dekel (2010) showed that this was unlikely, unless the star-formation efficiency per free fall time in the clumps is much higher than observed locally, which does not appear to be the case (Freundlich et al. 2013). Furthermore, Dekel & Krumholz (2013) argued that a steady wind generated by radiation pressure was not expected to unbind the clump before it had turned most of its mass into stars. Their argument was based on simulations by Krumholz & Thompson (2012, 2013) which showed that radiation trapping within the giant clumps is negligible because it destabilizes the wind. Thus, the total momentum injection from radiation pressure, stellar winds and supernovae is limited to $\lesssim 5L/c$, significantly lower than the values of $\sim 20-30L/c$ advocated by Hopkins et al. (2012).

In previous work, we studied the formation and evolution of giant clumps at redshifts $z = 1-4$ in the weak feedback limit (Mandelker et al. 2014, hereafter M14), using a large suite of 29 cosmological zoom-in simulations of $\sim 10^{12}M_{\odot}$ haloes at $z \sim 2$, run with adaptive mesh refinement (AMR) with a maximal resolution of $35-70$ pc. Using a three-dimensional clump finder on the gas, we identified clumps in the simulations, distinguishing in situ clumps formed during VDI from ex situ clumps that joined the disc as minor mergers. The simulations included only thermal feedback from supernovae and stellar winds, under which the massive clumps survived and migrated towards the disc centre. Clump evolution during migration generated gradients in clump properties across the disc, so that clumps closer to the centre tended to be more massive, with older stellar populations, lower specific SFR (sSFR), lower gas fractions and higher metallicities. Observational indications for similar gradients (Förster Schreiber et al. 2011; Guo et al. 2012) provided support for the survival of massive clumps.

In a preliminary attempt to study the effect of radiation pressure (RP) feedback on clump survival, we examined a small subset of the simulations used in this work (Moody et al. 2014), consisting of 8 pairs of cosmological zoom-in simulations of $\sim (2-5) \times 10^{11}M_{\odot}$ haloes at $z \sim 2$, with a maximal AMR resolution of $17-35$ pc. Each pair consisted of two simulations run from the same initial conditions, one implementing only thermal feedback from supernovae and stellar winds and the second adding a model for RP feedback from UV photons, with no IR trapping (Ceverino et al. 2014).

Using a two-dimensional clump finder on stellar mass maps, we found that the number of clumps with stellar mass less than 5% of the disc stellar mass was drastically reduced with the inclusion of RP, but that more massive clumps were largely unaffected. We also found that clump counts in mock HST observations of the RP simulations roughly matched observational estimates. However, this study had several limitations. Firstly, we did not account for the significant gas content of clumps, studying only the stellar clumps. Second, while identifying clumps in two-dimensional stellar mass maps is closer to what is done observationally, it limits the analysis of the three-dimensional physical properties of the clumps and the role played by RP in their formation, evolution and disruption.

In this work, we expand on M14 and Moody et al. (2014). We use a large suite of 34 cosmological zoom-in simulations of galaxies, most evolved to $z \sim 1$, whose halo masses are in the range $\sim 10^{11}-10^{12}M_{\odot}$ at $z \sim 2$. These 34 simulations include the same model for RP feedback, in addition to supernova feedback and stellar winds, as in Ceverino et al. (2014) and Moody et al. (2014), and 29 of them have counterparts run from the same initial conditions without the inclusion of RP. We identify clumps in three-dimensions, in both gas and stars, and study their physical properties. By tracking clumps through time using their stellar particles, we study the effect of RP feedback on the formation and evolution of giant clumps and find the conditions leading to clump disruption or survival. Our two main goals are to assess theoretically the conditions for clump survival when RP is included, and to find observational tests that can distinguish short-lived clumps from long-lived clumps and place constraints on models of stellar feedback and clump evolution.

This paper is organized as follows: In §2 we provide an overview of the simulations, including their limitations. In §3 we describe our analysis method and how we define galaxy and clump properties. In §4 we compare global properties of the two galaxy samples, with and without radiative feedback. In §5 we address the effect of radiative feedback on clumps. In §6 we address properties of clumps, observational signatures of clump migration and disc clumpiness. We discuss our results in §7 and summarize our conclusions in §8.

2 SIMULATIONS

We use zoom-in hydro-cosmological simulations of 34 moderately massive galaxies that comprise the VELA simulation suite (Ceverino et al. 2014; Zolotov et al. 2015). The fiducial sample includes an implementation of RP feedback from young stars (RP simulations, hereafter RPs), and 29 of the 34 galaxies were resimulated without RP (NoRP simulations, hereafter NoRPs), but with all other sub-grid physics unchanged. Several recent works have used the VELA suite to study a variety of issues relating to high redshift galaxy formation. These include the stellar to halo

mass relation (Moody et al. 2014); galaxy clumpiness and morphological evolution (Moody et al. 2014; Snyder et al. 2015); the evolution of galaxy shapes (Ceverino, Primack & Dekel 2015; Tomassetti et al. 2016); the link between metal inhomogeneities and gas inflows (Ceverino et al. 2016a); galaxy outflows (Ceverino et al. 2016b); compaction, quenching and the formation of blue and red nuggets (Zolotov et al. 2015) and their relation to the evolution of density profiles (Tacchella et al. 2016a) and the confinement of the main sequence of star formation (Tacchella et al. 2016b); and the relation between clump formation and Toomre instability (Inoue et al. 2016). In this section, we give an overview of the key aspects of the simulations. Further details regarding the numerical methods can be found in Ceverino et al. (2014).

2.1 Simulation Method and Sub-Grid Physics

The VELA simulations utilize the Adaptive Refinement Tree (ART) code (Kravtsov, Klypin & Khokhlov 1997; Kravtsov 2003; Ceverino & Klypin 2009), which accurately follows the evolution of a gravitating N -body system and the Eulerian gas dynamics, with an AMR maximum resolution of 17.5 – 35 pc in physical units at all times¹. The dark matter particle mass is $8.3 \times 10^4 M_\odot$ and the stellar particles have a minimum mass of $10^3 M_\odot$, similar to the stellar mass of an Orion-like star cluster. Each AMR cell is split into 8 cells once it contains a mass in stars and dark-matter higher than $2.6 \times 10^5 M_\odot$, equivalent to 3 dark-matter particles, or a gas mass higher than $1.5 \times 10^6 M_\odot$. This quasi-Lagrangian strategy ends at the highest level of refinement that marks the minimum cell size at each redshift. We often refine based on stars and dark-matter particles rather than gas, so within the central halo and the star-forming disc the highest refinement level is reached for gas densities between $\sim 10^{-2} - 100 \text{ cm}^{-3}$, and occasionally for densities as low as $\sim 10^{-3} \text{ cm}^{-3}$. In the outer circumgalactic medium, near the halo virial radius, the median resolution is ~ 500 pc.

Beyond gravity and hydrodynamics, the code incorporates the physics of gas and metal cooling, UV-background photoionization, stochastic star formation, gas recycling, stellar winds and metal enrichment, and thermal feedback from supernovae (Ceverino, Dekel & Bournaud 2010; Ceverino et al. 2012), plus an implementation of feedback from radiation pressure (Ceverino et al. 2014). A subsample of the full VELA suite, 29 of the 34 galaxies, was run using the same initial conditions and sub-grid physics, but without the implementation of radiative feedback.

We use the CLOUDY code (Ferland et al. 1998)

¹ The minimum cell size is set to 17.5 pc in physical units at expansion factor $a = 0.16$ ($z = 5.25$). Due to the expansion of the whole mesh while the refinement level remains fixed, the minimum cell size grows in physical units, becoming 35 pc at $a = 0.32$ ($z = 2.125$). At this time we add a new level to the comoving mesh, so the minimum cell size becomes 17.5 pc again, and so on.

to calculate the cooling and heating rates for a given gas density, temperature, metallicity, and UV background, assuming a slab of thickness 1 kpc. We assume a uniform UV background, following the redshift-dependent Haardt & Madau (1996) model, except for gas densities higher than 0.1 cm^{-3} where we use a substantially suppressed UV background ($5.9 \times 10^6 \text{ erg s}^{-1} \text{ cm}^{-2} \text{ Hz}^{-1}$) in order to mimic the partial self-shielding of dense gas. This allows dense gas to cool down to temperatures of ~ 300 K. The equation of state is assumed to be that of an ideal monoatomic gas. Artificial fragmentation on the cell size is prevented by introducing a pressure floor, ensuring that the Jeans scale is resolved by at least $N = 7$ cells (Ceverino, Dekel & Bournaud 2010). The pressure floor is given by

$$P_{\text{floor}} = \frac{G\rho^2 N^2 \Delta^2}{\pi\gamma} \quad (1)$$

where ρ is the gas density, Δ is the cell size, and $\gamma = 5/3$ is the adiabatic index of the gas.

Star formation is allowed to occur at densities above a threshold of 1 cm^{-3} and at temperatures below 10^4 K. Most stars (> 90 %) form at temperatures well below 10^3 K, and more than half of them form at 300 K in cells where the gas density is higher than 10 cm^{-3} . New stellar particles are generated with a timestep of $dt_{\text{SF}} \sim 5$ Myr. We implement a stochastic model, where the probability to form a stellar particle in a given timestep is

$$\mathbf{P} = \min\left(0.2, \sqrt{\frac{\rho_{\text{gas}}}{1000 \text{ cm}^{-3}}}\right) \quad (2)$$

In the formation of a single stellar particle, its mass is equal to

$$m_* = m_{\text{gas}} \frac{dt_{\text{SF}}}{\tau} \sim 0.42 m_{\text{gas}} \quad (3)$$

where m_{gas} is the mass of gas in the cell where the particle is being formed, and $\tau = 12$ Myr is a parameter of the simulations which was calibrated to match the empirical Kennicutt-Schmidt law (Kennicutt 1998). We assume a Chabrier 2003 stellar initial mass function. Further details can be found in Ceverino et al. (2014).

The thermal stellar feedback model releases energy from stellar winds and supernova explosions as a constant heating rate over 40 Myr following star formation. The heating rate due to feedback may or may not overcome the cooling rate, depending on the gas conditions in the star-forming regions (Dekel & Silk 1986; Ceverino & Klypin 2009), as we do not explicitly switch off cooling in these regions. The effect of runaway stars is included by applying a velocity kick of $\sim 10 \text{ km s}^{-1}$ to 30 % of the newly formed stellar particles. The code also includes the later effects of Type Ia supernova and stellar mass loss, and it follows the metal enrichment of the ISM.

In the fiducial (RP) models, radiation pressure is incorporated through the addition of a non-thermal pressure term to the total gas pressure in regions where ionizing photons from massive stars are produced

and may be trapped. This ionizing radiation injects momentum in the cells neighbouring massive star particles younger than 5 Myr whose column density exceeds 10^{21} cm^{-2} , isotropically pressurizing the star-forming regions. The expression for the radiation pressure is

$$P_{\text{rad}} = \frac{\Gamma m_*}{R^2 c} \quad (4)$$

where R is set to half the cell size for the cell hosting a stellar mass m_* , and to the cell size for its closest neighbours. The value of Γ is taken from the stellar population synthesis code `STARBURST99` (Leitherer et al. 1999). We use a value of $\Gamma = 10^{36} \text{ erg s}^{-1} M_{\odot}^{-1}$ which corresponds to the time averaged luminosity per unit mass of the ionizing radiation during the first 5 Myr of the evolution of a single stellar population. After 5 Myr, the number high mass stars and ionizing photons declines significantly. Since the significance of radiation pressure also depends on the optical depth of the gas within a cell, we use a hydrogen column density threshold of $N = 10^{21} \text{ cm}^{-2}$, above which ionizing radiation is effectively trapped and radiation pressure is added to the total gas pressure. See the ‘‘RadPre’’ model of Ceverino et al. (2014) for further details.

The initial conditions for the simulations are based on dark-matter haloes that were drawn from dissipationless N-body simulations at lower resolution in three comoving cosmological boxes (box-sizes of 10, 20, and 40 Mpc/h). We assume the standard Λ CDM cosmology with the WMAP5 cosmological parameters, namely $\Omega_m = 0.27$, $\Omega_{\Lambda} = 0.73$, $\Omega_b = 0.045$, $h = 0.7$ and $\sigma_8 = 0.82$ (Komatsu et al. 2009). Each halo was selected to have a given virial mass at $z = 1$ and no ongoing major merger at that time. This latter criterion eliminates less than 10 % of the haloes, which tend to be in dense proto-cluster environments at $z \sim 1$. The target virial masses at $z = 1$ were selected in the range $M_v = 2 \times 10^{11} - 2 \times 10^{12} M_{\odot}$, with a median of $5.6 \times 10^{11} M_{\odot}$. If left in isolation, the median mass at $z = 0$ would be $\sim 10^{12} M_{\odot}$. In practice, the actual mass range is broader, with some of the haloes merging into more massive haloes that host groups at $z = 0$.

2.2 Galaxy Samples

More than half the sample was evolved with RP to $z \leq 1$ and all but 5 were evolved to $z \leq 2$. The NoRP runs were often stopped at higher redshifts, due to an overproduction of stars which slowed the simulations down considerably. The simulation outputs were stored and analyzed at fixed intervals in the cosmic expansion factor $a = (1 + z)^{-1}$, $\Delta a = 0.01$, which at $z = 2$ corresponds to about 100 Myr. Table 1 lists the final available snapshot for each of the 34 RP runs and the 29 corresponding NoRP runs in terms of expansion factor, a_{fin} , and redshift, z_{fin} . We detect the main progenitor in the final available output by using the `AdaptaHOP` group finder (Aubert, Pichon & Colombi 2004; Tweed et al. 2009) on the stellar particles. It is then traced back

in time until it contains fewer than 100 stellar particles, typically between $a = 0.10 - 0.13$ ($z = 6.5 - 9$).

In §4 and §5 we directly compare the RP and NoRP samples using only snapshots available in both sets of simulations. In these cases, visual inspection of each snapshot is performed to ensure that the same galaxy is being traced in both samples. Occasionally, when there is a roughly equal mass merger, the automated algorithm may trace different progenitors in the RP and NoRP samples. Whenever this happens, we change the NoRP version to track the same galaxy as in the RP sample. In §6 we analyze the RPs independently of their NoRP counterparts, making use of the full sample.

2.3 Limitations of the Current Simulations

The cosmological simulations used in this paper are state-of-the-art in terms of high-resolution AMR hydrodynamics and the treatment of key physical processes at the subgrid level, highlighted above. However, like other simulations, they are not yet perfect in their treatment of the star formation and feedback processes. While the SFR recipe was calibrated to reproduce the KS relation and a realistic SFR efficiency per free fall time (Ceverino et al. 2014), the code does not yet follow in detail the formation of molecules and the effect of metallicity on SFR (Krumholz & Dekel 2012). Additionally, the resolution does not allow the capture of Sedov-Taylor adiabatic phase of supernova feedback. The radiative stellar feedback assumed no infrared trapping, in the spirit of low trapping advocated by Dekel & Krumholz (2013) based on Krumholz & Thompson (2012, 2013). Other works assume more significant trapping (Murray, Quataert & Thompson 2010; Hopkins et al. 2012; Hopkins, Quataert & Murray 2012), which makes the strength of the radiative stellar feedback here lower than in other simulations². Finally, AGN feedback and feedback associated with cosmic rays and magnetic fields are not yet incorporated. Nevertheless, the star formation rates, gas fractions, and stellar to halo mass ratios are all in the ballpark of the estimates deduced from abundance matching and provide a better match to observations than earlier simulations (Ceverino et al. 2014; Moody et al. 2014 and Fig. 3).

The uncertainties, and any possible remaining mismatches by a factor of order 2, are comparable to the observational uncertainties. For example, the

² On the other hand, unresolved inhomogeneities and substructure within star-forming clumps could create low-density ‘‘chimneys’’ from which photons would leak out, thus lowering the effective boost-factor. For reasonable parametrizations of the unresolved density distributions within typical star-forming regions and expected values of the cloud-averaged optical depth, photon-leakage could easily lower the effective trapping factor by a factor of $\gtrsim 2$ (Hopkins, Quataert & Murray 2011, appendix B). Thus, while our model for RP feedback is not formally a ‘‘lower limit’’, it is still weaker than what is assumed in other simulations, with both more significant trapping and no accounting of photon-leakage.

stellar-to-halo mass fraction is not well constrained observationally at $z \sim 2$. Recent estimates by Burkert et al. (2015) (see their Fig. 5) based on the observed kinematics of $z \sim 0.6 - 2.8$ SFGs reveal significantly larger ratios than the estimates based on abundance matching (Conroy & Wechsler 2009; Moster et al. 2010; Moster, Naab & White 2013; Behroozi, Conroy & Wechsler 2010; Behroozi, Wechsler & Conroy 2013) at $M_v < 10^{12} M_\odot$. In §4, we present a detailed comparison of the stellar-to-halo mass relation in our simulations and the observational data (Fig. 3). We conclude that our simulations produce values that are in the ballpark of the observational estimates, and within the observational uncertainties.

If the SFR at very high redshifts is still overestimated, then this may lead to more clumps forming at earlier times when the gas fractions are still high, and less efficient clump formation at $z \lesssim 2$ when gas fractions are underestimated. However, we find that the fraction of clumpy galaxies as a function of redshift roughly matches observations (§6). Additional sources of feedback, from infrared trapping and AGN, may affect the lifetimes and properties of clumps. However, our simulations with intermediate feedback have the advantage of forming both long-lived bound clumps and short-lived disrupting clumps in the same galactic environment. By studying these two populations, we deduce observable differences between them (§6), which will place tighter constraints on models for clump evolution and for feedback. Furthermore, Ceverino et al. (2014) showed that photon trapping with boost factors of ~ 3 above the UV radiation, as advocated by Dekel & Krumholz (2013), changes the final stellar mass by $\lesssim 20\%$ and has only a minor effect on the density distribution of ISM gas. We therefore suspect that our current simulations capture the majority of the effect.

3 ANALYSIS

In this section we describe how physical properties of the virial haloes, the galactic discs and the clumps are defined. We also describe the clump finding algorithm, the method for tracking clump histories and the distinction between in situ, ex situ and bulge clumps.

3.1 Physical Quantities

The virial mass, M_v , is the total mass within a sphere of radius R_v that encompasses an overdensity of $\Delta(z) = (18\pi^2 - 82\Omega_\Lambda(z) - 39\Omega_\Lambda(z)^2)/\Omega_m(z)$, where $\Omega_\Lambda(z)$ and $\Omega_m(z)$ are the cosmological parameters at z (Bryan & Norman 1998). The virial properties for the 34 RP galaxies are listed in Table 1, together with the stellar mass, M_* , gas mass, M_g , and star-formation rate, SFR, within $0.15R_v$. These are quoted at $z = 2$ except for the 5 galaxies that were stopped at higher redshift, marked by *, for which we quote the properties at $z = z_{\text{fin}}$.

The stellar mass, M_* , is the instantaneous mass in stars, after accounting for stellar mass loss. The simulation calculates stellar mass loss using an analytic fitting formula, where 10%, 20% and 30% of the initial mass of a stellar particle is lost after 30 Myr, 260 Myr and 2 Gyr respectively. We refer to the birth mass of stars, *without* accounting for stellar mass loss, as $M_{*,i}$.

The SFR is obtained by $\text{SFR} = \langle M_{*,i}(t_{\text{age}} < t_{\text{max}})/t_{\text{max}} \rangle_{t_{\text{max}}}$, where $M_{*,i}(t_{\text{age}} < t_{\text{max}})$ is the mass at birth in stars younger than t_{max} . The average $\langle \cdot \rangle_{t_{\text{max}}}$ is obtained for t_{max} in the interval $[40, 80]$ Myr in steps of 0.2 Myr in order to reduce fluctuations due to the ~ 5 Myr discreteness in stellar birth times in the simulation. The t_{max} in this range are long enough to ensure good statistics. This represents the SFR on ~ 60 Myr timescales, which is a crude proxy for H α based SFR measurements, while UV based measurements are sensitive to stars younger than ~ 100 Myr.

We define the specific SFR as $\text{sSFR} = \text{SFR}/M_*^3$ and the gas fraction as $f_g = M_g/(M_g + M_*)$. The stellar age of a system is defined as the instantaneous mass-weighted mean age of its stellar particles.

3.2 The Galactic Disc

We define a disc in each snapshot using gas with temperatures $T < 1.5 \times 10^4$ K and stars younger than 100 Myr. Varying these thresholds in the range $(1 - 5) \times 10^4$ K and 50 - 150 Myr has no significant impact on any of our results. We hereafter refer to this as the “cold” component of the system. The disc plane is determined by the angular momentum vector of the cold component. This vector, along with the disc radius, R_d , and height (half thickness), H_d , are computed iteratively until all converge to within 5%, following the prescription in Appendix B of M14. Briefly, the disc radius, R_d , contains 85% of the cold mass within a cylinder of radius $r_0 = 0.15R_v$ and height $h_0 = 1$ kpc. The disc thickness, $2H_d$, contains 85% of the cold mass within a cylinder of radius and height $r_1 = h_1 = R_d$. The disc angular momentum is that of the cold material within a cylinder of radius R_d and height H_d . We varied r_0 in the range $0.1 - 0.2R_v$, h_0 in the range $0.5 - 1.5$ kpc as well as the value of H_d from the previous iteration, and the cold mass fraction in the range 80 - 90%, and found no significant effect on our main results. See M14 for further details.

All gas within the final cylinder is assigned to the disc. However, a stellar particle is assigned to the disc only if it meets an additional kinematic criterion, whereby the z -component of its specific angular momentum (parallel to the disc angular momentum), j_z , is higher than a fraction f_j of the maximum specific angular momentum for the same orbital energy, $j_{\text{max}} = |v|r$. Here, $|v|$ is the magnitude

³ Note that this is not the inverse formation timescale of the stellar system, which is $\text{SFR}/M_{*,i}$. However, since the mass loss rate is small compared to the SFR in our galaxies, this makes only a small difference.

The VELA suite of 34 simulated galaxies with radiative feedback (RP)

Galaxy	R_v kpc	M_v $10^{12} M_\odot$	$M_{s, 0.15R_v}$ $10^{10} M_\odot$	$M_{g, 0.15R_v}$ $10^{10} M_\odot$	$SFR_{0.15R_v}$ $M_\odot \text{ yr}^{-1}$	a_{fin}	z_{fin}	$a_{\text{fin, NoRP}}$	$z_{\text{fin, NoRP}}$
01	58.25	0.16	0.22	0.20	2.65	0.50	1.00	0.50	1.00
02	54.50	0.13	0.19	0.24	1.81	0.50	1.00	0.50	1.00
03	55.50	0.14	0.42	0.15	3.72	0.50	1.00	0.50	1.00
04	53.50	0.12	0.09	0.13	0.48	0.50	1.00	—	—
05	44.50	0.07	0.09	0.11	0.58	0.50	1.00	0.50	1.00
06	88.25	0.55	2.19	0.49	20.60	0.37	1.70	0.30	2.33
07	104.25	0.90	6.23	1.62	25.86	0.54	0.85	0.35	1.86
08	70.50	0.28	0.35	0.21	5.69	0.57	0.75	0.42	1.38
09	70.50	0.27	1.07	0.43	3.93	0.40	1.50	0.39	1.56
10	55.25	0.13	0.63	0.18	3.22	0.56	0.79	0.44	1.27
11	69.50	0.27	0.92	0.70	14.59	0.46	1.17	0.46	1.17
12	69.50	0.27	2.03	0.28	2.88	0.44	1.27	0.44	1.27
13	72.50	0.31	0.78	0.90	13.88	0.51	0.96	0.51	0.96
14	76.50	0.36	1.33	0.70	25.40	0.42	1.38	0.37	1.70
15	53.25	0.12	0.55	0.15	1.57	0.56	0.79	0.56	0.79
16 *	62.75	0.50	4.27	0.67	20.26	0.24	3.17	0.24	3.17
17 *	105.75	1.13	8.97	1.55	64.82	0.31	2.23	—	—
19 *	91.25	0.88	4.52	0.88	40.78	0.29	2.45	0.26	2.85
20	87.50	0.53	3.84	0.62	7.15	0.44	1.27	—	—
21	92.25	0.62	4.21	0.68	9.50	0.50	1.00	0.41	1.44
22	85.50	0.49	4.50	0.32	12.07	0.50	1.00	—	—
23	57.00	0.15	0.82	0.24	3.28	0.50	1.00	0.50	1.00
24	70.25	0.28	0.92	0.42	4.31	0.48	1.08	—	—
25	65.00	0.22	0.73	0.13	2.30	0.50	1.00	0.50	1.00
26	76.75	0.36	1.61	0.40	9.63	0.50	1.00	0.50	1.00
27	75.50	0.33	0.83	0.61	7.92	0.50	1.00	0.46	1.17
28	63.50	0.20	0.24	0.32	5.70	0.50	1.00	0.50	1.00
29	89.25	0.52	2.56	0.49	18.49	0.50	1.00	0.36	1.78
30	73.25	0.31	1.67	0.52	3.80	0.34	1.94	0.30	2.33
31 *	38.50	0.23	0.81	0.24	16.18	0.19	4.26	0.19	4.26
32	90.50	0.59	2.71	0.56	14.89	0.33	2.03	0.26	2.85
33	101.25	0.83	5.04	0.63	32.68	0.39	1.56	0.30	2.33
34	86.50	0.52	1.66	0.62	14.66	0.35	1.86	0.29	2.45
35 *	44.50	0.23	0.59	0.35	23.60	0.22	3.55	0.22	3.55

Table 1. Quoted are the virial radius, R_v , the total virial mass, M_v , the stellar mass, M_* , the gas mass, M_g and the star formation rate, SFR, for the 34 VELA simulations with RP. M_* , M_g and SFR are quoted within $0.15R_v$. Also listed are the final simulation scale factor, a_{fin} , and redshift, z_{fin} , as well as the final scale factor and redshift of the NoRP counterpart if one exists, $a_{\text{fin, NoRP}}$ and $z_{\text{fin, NoRP}}$. All physical properties are quoted at $z = 2$, except for the five cases marked *, where they are quoted at the final simulation output, $z_{\text{fin}} > 2$.

of the velocity of the stellar particle and r is its cylindrical distance from the galactic centre. We adopt $f_J = 0.7$ (Ceverino, Dekel & Bournaud 2010, M14). Whenever there is a well defined disc, the vast majority of the cold mass obeys this criterion (see Ceverino, Primack & Dekel 2015 and Tomassetti et al. 2016 for the typical stellar mass and redshift when galaxies develop well defined discs).

3.3 Clump Analysis

We identify clumps in 3D using a method similar to that of M14. The main difference is that in that work we only identified clumps in gas, while here we identify clumps in both the cold component and the stellar component. As was highlighted in M14 and in Moody et al. (2014), there is typically not a one-to-one correspondence between gas and stellar clumps, making it important to study both populations. We briefly

review the clump finding method here and refer the reader to M14 for further details.

3.3.1 Clump finder

We detect clumps within a cube of side $L = \max(4R_d, 10 \text{ kpc})$ centred on the main galaxy. Using a cloud-in-cell (CiC) interpolation, we deposit mass in a uniform grid with a cell size of $\Delta = 70 \text{ pc}$, so between 2 and 4 times the maximal AMR resolution, whose z axis is aligned with the normal to the disc plane. We then smooth this grid with a spherical Gaussian filter whose full width at half maximum (FWHM) is $F_W = \min(2.5 \text{ kpc}, 0.5R_d)$, and calculate the density residual at each point $\delta_\rho = (\rho - \rho_W)/\rho_W$, where ρ and ρ_W are the unsmoothed and smoothed density fields respectively. We do this once for the cold mass and once for the stellar mass, and at each point take the maximum of the two residual values. We define clumps as connected regions containing at least 8 grid

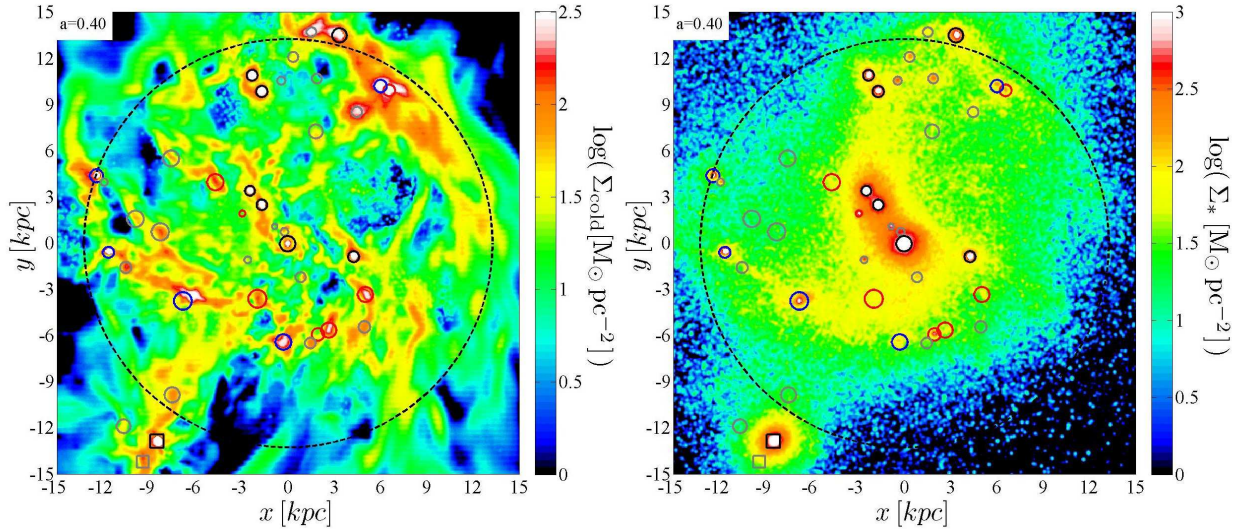


Figure 1. Clump identification. Shown is a face-on view of the RP version of V13 at $a = 0.40$ ($z = 1.5$). The disc radius, $R_d \simeq 13.3$ kpc, is marked by a dashed circle. The integration depth is $\pm 2R_d$. The left panel shows the surface density of the cold component and the right panel shows the stellar surface density. Note the different scale of the color bar in both panels. All clumps with baryonic densities $n_c > 1 \text{ cm}^{-3}$ and masses $M_c > 10^7 M_\odot$ are marked in both panels, in situ clumps with circles and ex situ clumps with squares. The size of the marker shows the clump radius, R_c . Clumps with masses $10^7 < M_c < 10^{7.5} M_\odot$ are marked in grey, clumps with $10^{7.5} < M_c < 10^8 M_\odot$ are marked in red, clumps with $10^8 < M_c < 10^{8.5} M_\odot$ are marked in blue, and clumps with $10^{8.5} < M_c$ are marked in black. The marked clumps agree with a by-eye inspection of the galaxy, and highlight the fact that clumps identified in the cold component (or in gas) do not necessarily match clumps identified in stars.

cells, corresponding to between 64 and 512 cells at the maximal AMR refinement, above a residual threshold of $\delta_\rho^{\text{min}} = 10$. This technique selects regions that are at least 10 times denser than their local surroundings in cold and/or stellar mass. A discussion on the sensitivity of our results to variations in the parameters of the algorithm, Δ , F_W and δ_ρ^{min} , is provided in §A.

Gas, stars and dark matter particles are deposited in the clump cells using CiC interpolation, and no attempt was made to remove unbound material from the clumps. We remove from the sample all clumps with baryonic mass $M_c < 10^6 M_\odot$. Hereafter, when we discuss clump mass we refer to the baryonic mass unless explicitly stated otherwise.

We define the clump centre as the baryonic density peak and the clump radius, R_c , as the radius of a sphere with the same volume as the clump: $(4\pi/3)R_c^3 = N \times (70 \text{ pc})^3$, where $N \geq 8$ is the total number of grid cells within the clump. This translates to a minimum clump diameter of ~ 180 pc, which is on the order of 7 cells at the maximal AMR resolution of ~ 25 pc. Since the pressure floor ensures the Jeans length is always resolved by at least 7 cells, this is the minimal clump size where we could in principle have a complete sample.

We assign a shape parameter to each clump, S_c , using its inertia tensor, $I_{i,j} = \sum_{n=1}^N m_n (r_n^2 \delta_{i,j} - r_{n,i} r_{n,j})$. The sum is over all cells in the clump, m_n is the baryonic mass in the n -th cell, \vec{r}_n is the displacement vector of the n -th cell relative to the clump centre, $r_n^2 = \vec{r}_n \cdot \vec{r}_n$, and $\delta_{i,j}$ is the Kronecker Delta. We diagonalize the tensor and find the three eigenvalues, $I_1 \geq I_2 \geq I_3$. Finally, we define $S_c \equiv I_3/I_1$. For a perfect sphere, $S_c = 1$. For a

flattened, oblate clump, $S_c \simeq 0.5$. For a very prolate or filamentary clump, $S_c \ll 1$.

The clump finder is illustrated in Fig. 1, for one of the galaxies in the RP sample, V13 at $a = 0.40$ ($z = 1.5$). On the left we plot the surface density of the cold component in a face on projection and on the right we plot the stellar surface density in the same projection. Besides being a large, clumpy, star-forming disc, this example highlights the importance of detecting clumps in multiple tracers, since there is not a one-to-one correspondence between stellar and cold clumps.

The disc radius, $R_d \simeq 13.3$ kpc, is marked in both panels, as are all identified clumps with baryonic volume densities $n_c > 1 \text{ cm}^{-3}$ and masses $M_c > 10^7 M_\odot$. These thresholds were introduced here for clarity, because many low-mass, low-density clumps are not visible in 2D projection plots (recall that clumps are identified in 3D), and in any case for most of our analysis in §5 and §6 we will focus on clumps above these thresholds. There are two ex situ clumps (defined below) in this galaxy, which are marked with squares. The rest of the off-centre clumps are all in situ and are marked with circles, as is the central bulge clump (defined below). The size of the marker corresponds to the clump radius, R_c , while the color represents its mass. Clumps with $10^7 < M_c < 10^{7.5} M_\odot$ are marked in grey, clumps with $10^{7.5} < M_c < 10^8 M_\odot$ are marked in red, clumps with $10^8 < M_c < 10^{8.5} M_\odot$ are marked in blue, and clumps with $10^{8.5} M_\odot < M_c$ are marked in black. The disc mass is $M_d \simeq 2.5 \times 10^{10} M_\odot$ and the gas fraction is $\sim 40\%$.

3.3.2 Tracking individual clumps through time

The time between consecutive outputs is typically about half an orbital time at the disc edge. Since the expected migration time for clumps is roughly 2 disc orbital times, we are occasionally able to track individual clumps across several snapshots, which allows us to directly study the evolution and lifetimes of clumps. As the simulations were run with an Eulerian, grid based, code we cannot trace gas elements through time, and therefore track clumps using their stellar particles. We only attempt to track clumps that contain at least 10 stellar particles. For each such clump in a given snapshot, we search the preceding snapshot for all “progenitor clumps”, defined as clumps that contributed at least 25% of their stellar particles to the clump in question⁴. If a given clump has more than one progenitor clump in the same snapshot, we rank them by baryonic mass, consider the most massive one the main progenitor and the others as having merged, thus creating a clump merger tree. If a clump has no progenitors in the preceding snapshot, we search the previous snapshots until we either find a progenitor or reach the initial timestep of the simulation.

We define the clump time, t_c , as the time since clump formation. In the first snapshot when the clump is identified, we set t_c to the stellar age of the clump, provided this is less than the time since the previous snapshot, when the clump was not identified. Otherwise, we set $t_c = 0$. In later snapshots when the clump is identified, we add to t_c the physical time that has elapsed since its initial identification. Note that clump *time* differs from clump *age*, which is given by the mean stellar age and is thus affected by ongoing star-formation and tidal stripping of older stars (see Fig. 12 and Bournaud et al. 2014). The clump *lifetime*, $t_{c, \max}$, is the clump time at the final snapshot where the clump is identified. We refer to clumps that were identified in only one snapshot and have $t_{c, \max} = 0$ as zero-lifetime-clumps, or ZLCs. In §5 we will show that most of these are false positives, characterised by low densities and masses.

3.3.3 In situ, ex situ and bulge clumps

Following M14 we divide clumps into central “bulge” clumps, and off-centre clumps. A bulge clump forms the nucleus of the galactic bulge and is defined as a clump whose centre is within 2 grid cells of the galaxy centre. If there is more than one such clump, the most massive is considered the bulge clump and the rest are considered off-centre clumps. We discuss the prevalence of bulge clumps in the simulations in §5.

The off-centre clumps are divided into “in situ” clumps which formed within the disc through VDI,

⁴ As stellar particles are deposited on the grid using CiC interpolation, we only consider particles that have contributed at least half their mass to the clump for the purpose of clump tracking. This is to ensure that no stellar particle is associated with more than one clump in a given snapshot.

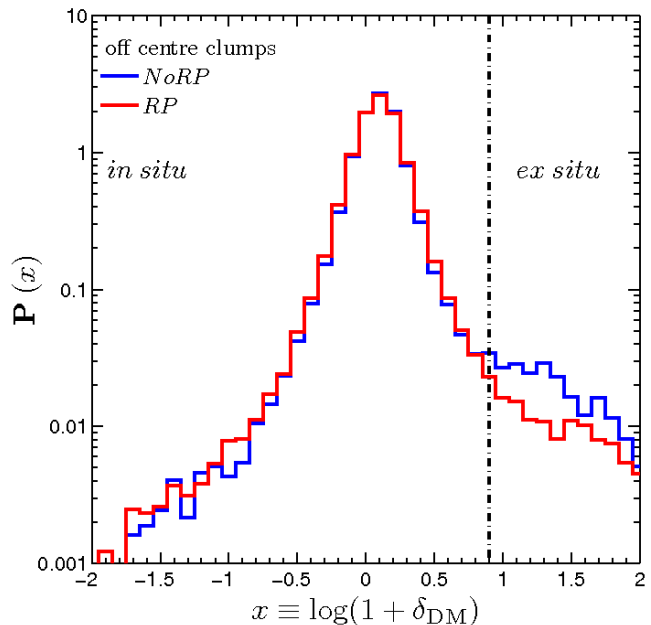


Figure 2. In situ vs ex situ clumps. Probability density of $x = \log(1 + \delta_{\text{DM}})$ (see text for details) for the off-centre clumps in the NoRPs (blue) and RPs (red). The vertical dash-dotted line marks the threshold between in situ and ex situ clumps at $x = 0.9$.

and “ex situ” clumps which are external mergers. As in M14 we distinguish in situ from ex situ clumps by their dark matter content. We compare the mean dark matter density within the clump, $\rho_{\text{DM}, c}$, to the mean dark matter density in a spherical shell (concentric with the host halo) 1 kpc thick around on the clump, $\rho_{\text{DM}, s}$, and define the dark matter overdensity $1 + \delta_{\text{DM}} \equiv \rho_{\text{DM}, c} / \rho_{\text{DM}, s}$. Figure 2 shows the probability density⁵, $\mathbf{P}(x)$ where $x = \log(1 + \delta_{\text{DM}})$, for the off-centre clumps in the NoRPs (blue line) and the RPs (red line). In both samples, the in situ clumps exhibit a roughly log-normal distribution centred on $x \sim 0.1$ with a dispersion of $\sigma_x \sim 0.13$, while the ex situ clumps form an extended tail to high values. We define ex situ clumps as clumps with $x_{\max} > 0.9$, where x_{\max} is the maximal value of x during the clump lifetime, and mark this threshold in Fig. 2. We discuss the contribution of ex situ clumps to the total clump population in §5.

An alternate definition of ex situ clumps could have been based on the birth place of the stellar particles within the clump. Among clumps with $M_c > 10^7 M_\odot$ and $\bar{\delta}_c > 25$, where our sample is complete and ZLCs are rare (see §5), these two definitions agree well. In $\sim 78\%$ (88%) of ex situ clumps selected by dark matter in the RPs (NoRPs), more than half the baryonic mass consists of stars formed outside the disc, as defined at the snapshot closest to the star particle’s birth. On the other hand, in both the RPs and the NoRPs, only $\sim 9\%$ of in situ clumps selected by dark matter have more than half their baryonic mass in ex situ stars.

⁵ The probability for a clump to have a value in the interval Δx about x is $\mathbf{P}(x)\Delta x$.

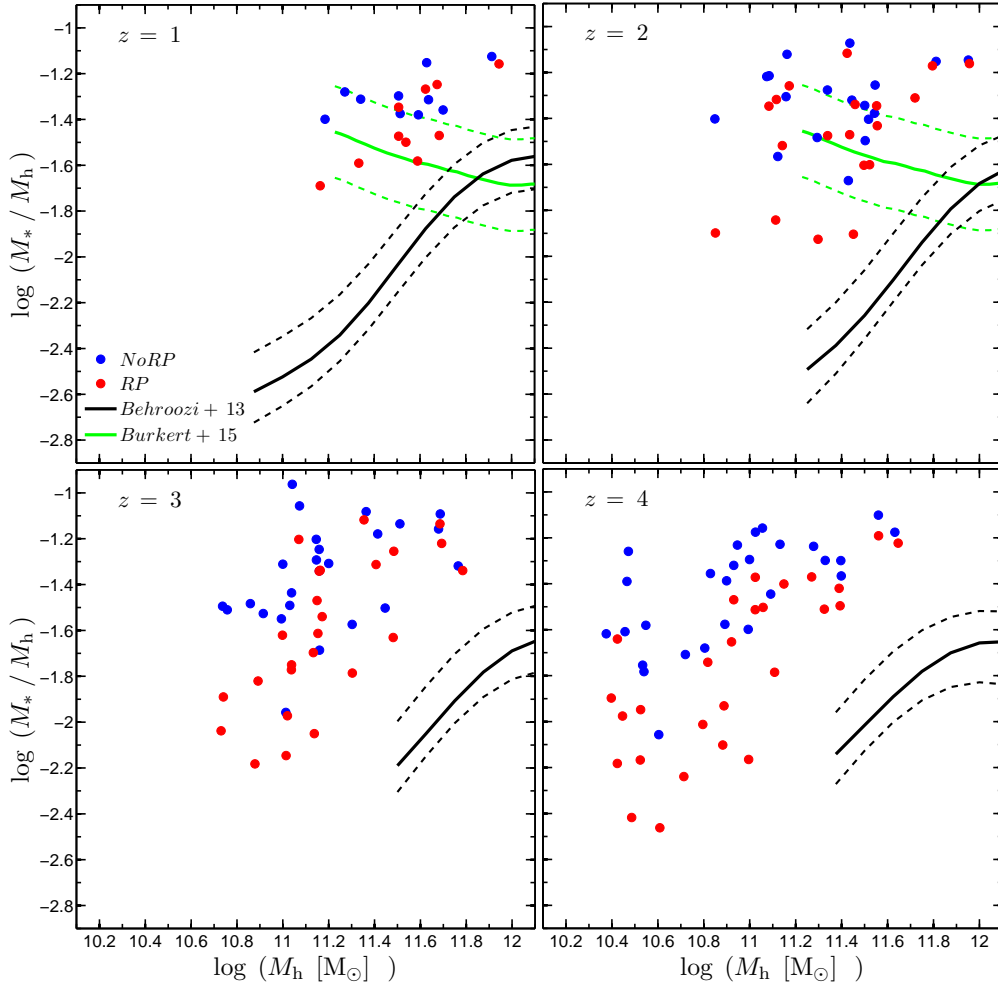


Figure 3. Ratio of stellar mass to halo mass in the NoRPs (blue points) and the RPs (red points), at redshifts $z = 1, 2, 3, 4$, in clockwise order from the top left. The solid black line is the mean relation from Behroozi, Wechsler & Conroy (2013) and the dashed black lines are the $1\text{-}\sigma$ scatter. The green solid and dashed lines are the median relation and $1\text{-}\sigma$ scatter from the “full” sample of 359 SFGs at $0.8 \lesssim z \lesssim 2.6$ from Burkert et al. (2015). The stellar mass is reduced in the RPs, typically by a factor of ~ 2 , and by up to a factor of ~ 10 in low mass haloes at early times. The RPs are still a factor of $\lesssim 2$ above the Behroozi, Wechsler & Conroy (2013) relation at $z \sim 1 - 2$, but are in much better agreement with Burkert et al. (2015), reflecting a factor ~ 2 uncertainty in observational estimates.

4 GLOBAL PROPERTIES OF THE GALAXY SAMPLES

In this section we examine the global effect of RP feedback on the galaxies in our sample, before studying its effect on giant clumps in §5. We limit our analysis here to snapshots that have both a RP and a NoRP version, which leaves 798 snapshots: 255 at $4 \leq z$, 131 at $3 \leq z < 4$, 168 at $2 \leq z < 3$, 244 at $0.8 \leq z < 2$.

4.1 Stellar Mass

Figure 3 shows the stellar-to-halo mass ratio as a function of halo mass for the two galaxy samples at four redshifts, $z = 1, 2, 3, 4$.⁶ Stellar

mass is defined here as the total within $0.15R_v$. For comparison, we show the abundance matching predictions of Behroozi, Wechsler & Conroy (2013), and recent estimates from (Burkert et al. 2015) which are based on observed kinematics of several hundred SFGs at redshifts $0.8 \lesssim z \lesssim 2.6$ from KMOS^{3D}, with similar masses to our simulated galaxies. RP feedback typically lowers the stellar mass by a factor of $\gtrsim 2$ (see also Moody et al. 2014). At low halo masses at high redshifts, the stellar mass can be decreased by up to a factor of ~ 10 , suggesting that radiative feedback is more efficient in low mass galaxies.

At redshifts $z \leq 2$, the RPs are still a factor of $\lesssim 2$ above the Behroozi, Wechsler & Conroy (2013) curve, though they appear consistent with the estimates of Burkert et al. (2015), at least for halos with $M_v < 4 \times 10^{11} M_\odot$, where most of our data lies. This reflects a factor of ~ 2 uncertainty in the observational estimates of the stellar-to-halo mass ratio for these halo masses

⁶ In practice, for each simulation we use the closest snapshot to each redshift, in the range $|\Delta z| < 0.1$.

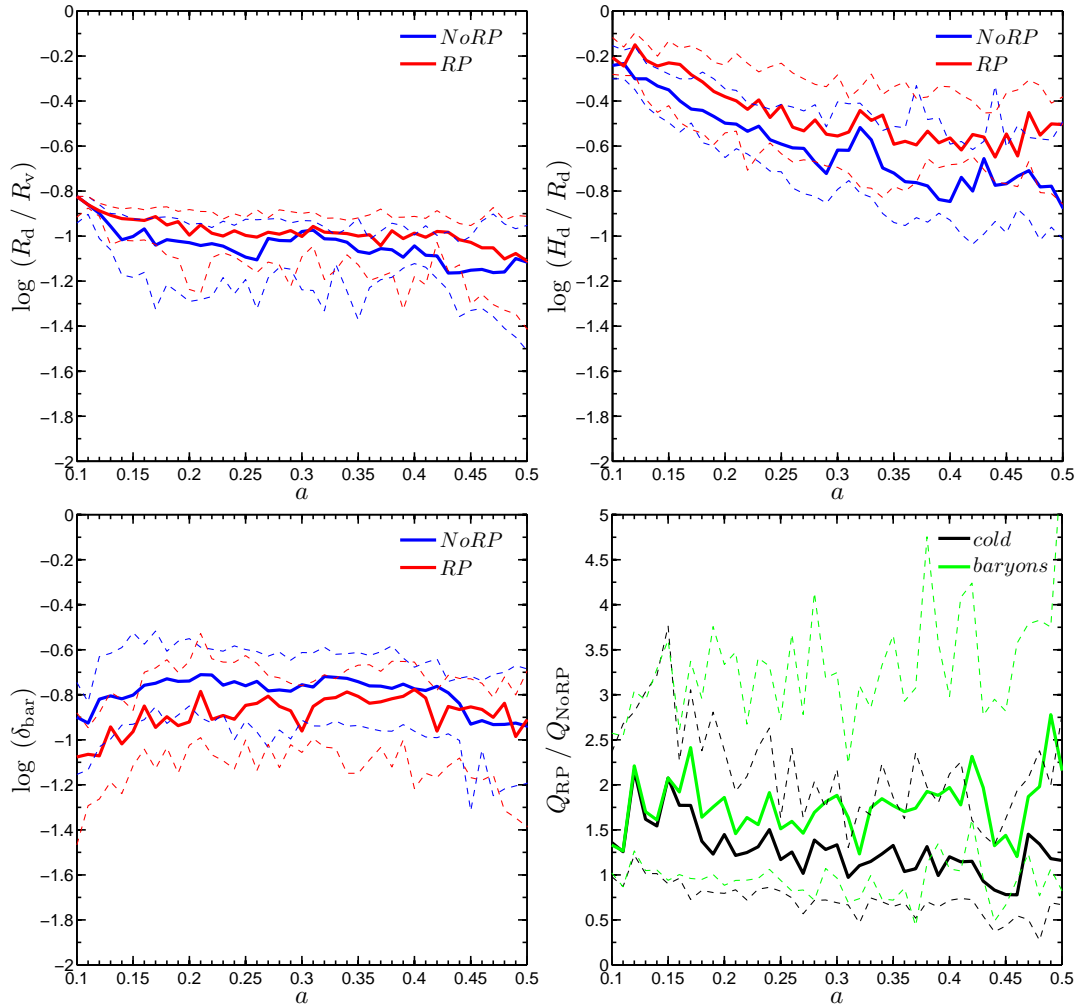


Figure 4. Disc properties in RPs and NoRPs. Each panel examines a different property related to the disc structure or stability: the disc radius normalized to the virial radius, R_d/R_v (top left), the disc height normalized to its radius, H_d/R_d (top right), and the baryonic disc mass normalized to the total mass within the disc radius $\delta_{\text{bar}} = M_d/M_{\text{tot}}(R_d)$ (bottom left). We show as a function of time represented by the expansion factor, a , the evolution of each property for the NoRP sample (blue) and the RP sample (red). The thick solid lines show the median and the thin dashed lines show the 67% scatter. In the bottom right we show the ratio of the global Toomre Q parameter between the two samples, using $Q \propto \delta^{-1}H_d/R_d$. In this panel, the green line refers to δ calculated using all baryons in the disc as shown in the bottom left panel, while the black line refers to δ calculated using only the cold mass in the disc. Both simulations produce thinner, more relaxed discs at later times. The NoRPs have a slight tendency for smaller, thinner discs, but are a higher fraction of the total mass within the disc radius. The global Toomre parameter in the RPs is typically $\lesssim 70\%$ larger than in the NoRPs, indicating that while RP may affect VDI and clump formation, the effect is not dramatic.

and redshifts, and our simulations produce values within the observational uncertainties. At $3 \leq z$, most of our sample lies at low halo masses where no direct comparison with existing predictions can be made. By extrapolating the Behroozi, Wechsler & Conroy (2013) relation towards lower halo masses, the off-set between our sample and the prediction is comparable to that at $z \leq 2$. We conclude that the RPs produce stellar masses that are in the ballpark of realistic values, within the observational uncertainties of a factor ~ 2 .

4.2 Disc Properties and Toomre Q

In Fig. 4 we compare the galaxy samples in terms of global disc structure and stability. We examine as a function of time, represented by the expansion factor a , the disc radius, thickness, mass fraction with R_d and Toomre Q parameter, as described below. For each of these properties we show the median and 67% scatter among all snapshots at a given expansion factor.

In the top left panel we examine the disc radius normalized to the virial radius, R_d/R_v . On average, the disc sizes are very similar in the two galaxy samples. The NoRPs have a very slight tendency to produce smaller discs than the RPs, by ~ 0.05 dex at all times. However, given the scatter in the data this does not

appear significant. Most of the scatter is caused by small differences in the times of major mergers and compaction events between the two samples, which mostly occur after $z \sim 4$ (Zolotov et al. 2015).

The top right panel examines the disc thickness, normalized to its radius H_d/R_d . To first order, this represents the velocity dispersion within the disc, $H_d/R_d \sim \sigma_z/V$. As R_d and H_d were both calculated using the cold component, this refers to the gas velocity dispersion, rather than the stellar value. The stronger feedback in the RPs results in thicker and more turbulent discs, especially at later times. The median ratio between individual snapshots paired in both sets of simulations increases monotonically from ~ 0.08 dex at $4 < z$ to ~ 0.19 dex at $z < 2$. However, the scatter is large, $\sigma \sim 0.14$ dex at $4 < z$ and ~ 0.19 dex at $z < 2$. It is unclear how much of this trend is the result of instantaneous feedback driving additional turbulence, and how much is the result of decreased gas fractions in NoRPs due to excessive star-formation at early times. Surely the latter contributes to the increased discrepancy at later times. However, this distinction is beyond the scope of the current paper.

The bottom left panel examines the ratio of the disc mass to the total mass within the disc radius, including the spheroid and dark matter halo components, $\delta_{\text{bar}} \equiv M_d/M_{\text{tot}}(R_d)$. This is an important indicator of disc instability (e.g. Dekel, Sari & Ceverino 2009). At early times, the NoRPs have a more prominent disc, which results from earlier settling of the galaxies into oblate structures (Tomassetti et al. 2016). Detailed analysis of the shapes of galaxies in the RPs indicate that galaxies tend to maintain a prolate shape at early times, developing a disc only after the first compaction event, when the baryons dominate the mass and potential at the inner radii (Ceverino, Primack & Dekel 2015). This happens earlier in the NoRP galaxies (Tomassetti et al. 2016). At late times, the two sets of simulations have comparable δ_{bar} . It is interesting to characterise the cold component in the disc by defining instead $\delta_{\text{cold}} = M_{\text{cold,d}}/M_{\text{tot}}(R_d)$. At $4 < z$, the NoRPs and the RPs have $\log(\delta_{\text{cold}}) \sim -0.9$ and -1 respectively. At $z \sim 3.5$, both have comparable values of $\log(\delta_{\text{cold}}) \sim -1.1$. By $z < 1.5$, the NoRPs have saturated at $\log(\delta_{\text{cold}}) \sim -1.5$, while the RPs have saturated at $\log(\delta_{\text{cold}}) \sim -1.3$. This indicates that the gas fractions in the RP discs are $\sim 60\%$ higher than in the NoRP discs at these redshifts.

The bottom right panel shows the ratio of the global Toomre Q parameter in the RPs to Q in the NoRPs, using the crude approximation (e.g. Dekel, Sari & Ceverino 2009):

$$Q \propto \frac{\sigma\Omega}{\Sigma} \propto \frac{\sigma}{V} \frac{M_{\text{tot}}}{M_d} \propto \delta^{-1} \frac{H_d}{R_d} \quad (5)$$

We do this once for the cold component only, using δ_{cold} , and once for the baryonic disc mass, using δ_{bar} (which still only includes stars that are co-rotating with the gas disc). This crudely approximates Q for a one-component model, assuming the gas and stars have comparable velocity dispersions. Since the discs contain dynamically hot stars as well, a two component Toomre analysis is

required to fully address the issue of disc instability. However, eq. (5) is not applicable for a two component system, and a more detailed analysis is beyond the scope of this paper. Therefore, rather than focus on the absolute values of Q , we only address the relative values in the two simulation suites, in order to compare the predicted strength of VDI. We note that in the RPs, the two component Q is not very different from Q computed using the cold component only (Inoue et al. 2016).

The NoRPs have slightly lower values of Q , indicating that they may be slightly more prone to instability and clump formation than the RPs. However, this difference is not large, $\sim 70\%$ when considering all baryons in the disc and less than that when considering only the cold component. We conclude that RP does not fundamentally stabilize the discs against VDI, so clump formation is not expected to be greatly suppressed.

4.3 ISM Structure

Figure 5 shows the density probability distribution function (PDF) of the ISM gas in the NoRPs and RPs, stacked over all common snapshots. We consider all gas with temperatures $T < 10^6$ K located within the disc cylinder at each snapshot⁷. Hot gas, with $T > 10^6$ K, contains only $\sim 1\%$ of the gas mass in the ISM and is not important for disc instability or for clump detection. We show both the mass-weighted PDF, $dm_{\text{gas}}/d\log(n)$ (left), and the volume weighted PDF, $dV_{\text{gas}}/d\log(n)$ (right). These are the mass fraction and volume fraction per logarithmic density interval, respectively.

At low to intermediate densities, the mass-weighted PDF of the NoRPs and the RPs have a very similar shape. Both are well fit by a log-normal distribution which has a mean density of $\log(n \cdot \text{cm}^3) \simeq 0$ and a standard deviation of $\sigma_{\log(n)} \simeq 0.74$. The mean density decreases from $\sim 3 \text{ cm}^{-3}$ at $4 < z$ to $\sim 0.6 \text{ cm}^{-3}$ at $z < 2$, in agreement with the cosmological scaling, while the standard deviation decreases from $\sigma_{\log(n)} \simeq 0.85$ to 0.64 in the same redshift range. We note that the adopted density threshold for star formation, $n_{\text{SF}} = 1 \text{ cm}^{-3}$, is at the peak of the mass weighted PDF. A log-normal shape for the density PDF is characteristic of isothermal, supersonic turbulence (Vazquez-Semadeni 1994; Padoan, Nordlund & Jones 1997; Scalo et al. 1998; Federrath, Klessen & Schmidt 2008; Price, Federrath & Brunt 2011; Hopkins et al. 2012) with the width of the distribution weakly depending on the Mach number as $\sigma_{\log(\rho)} \propto \sqrt{\ln(1 + 0.25M^2)}$ (Padoan, Nordlund & Jones 1997; Federrath, Klessen & Schmidt 2008).

At high densities, $n > 10 - 30 \text{ cm}^{-3}$, the distributions deviate from log-normality and develop power law tails, with slopes of ~ -0.5 and ~ -0.6 in the RPs and NoRPs respectively. The transition density increases with redshift, maintaining a factor $\gtrsim 10$ above the mean. The development of a power law tail at high densities is typical when self-gravity becomes

⁷ Note that this is a slightly larger volume in the RPs (Fig. 4).

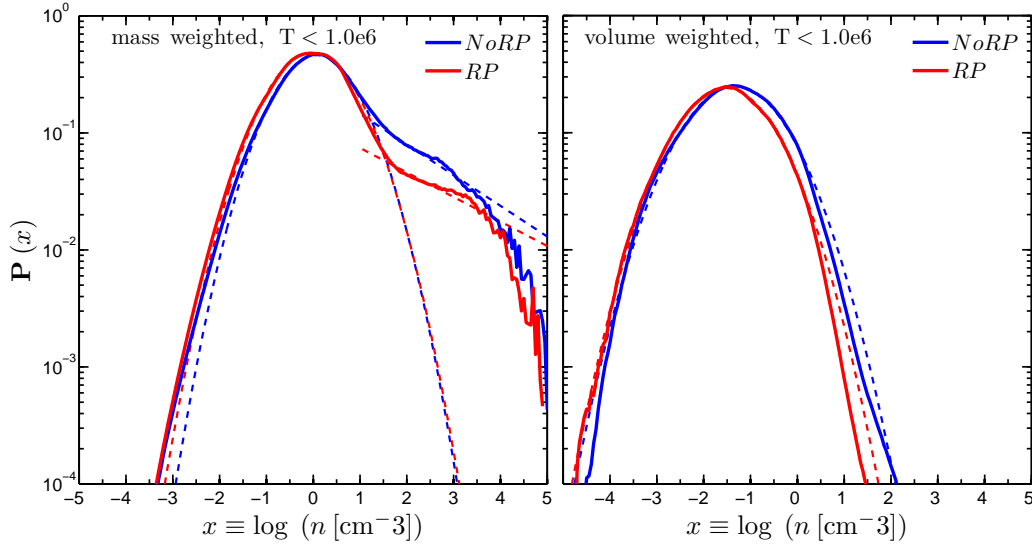


Figure 5. Density distribution of ISM gas with temperatures $T < 10^6$ K, stacked over the all common snapshots of NoRP (blue) and RP (red) galaxies. Solid lines are the data and dashed lines show best fit models. Left: mass-weighted density PDF, $dm_{\text{gas}}/d\log(n)$. In both sets of simulations, the distribution of gas with $n < 10 \text{ cm}^{-3}$ is well fit by a log-normal distribution with a mean density of $\log(n \cdot \text{cm}^3) \simeq 0$ and a dispersion of $\sigma_{\log(n)} \simeq 0.74$ (dashed lines). At high densities, $n \gtrsim 10 \text{ cm}^{-3}$, the distributions deviate from log-normality and are well fit by power laws, with slopes of ~ -0.5 and -0.6 for RP and NoRP respectively (dashed lines). While both models have a similar range of densities, RP decreases the amount of dense gas by roughly a factor of ~ 2 , heating it to temperatures $T > 10^6$ K and driving it to lower densities. Right: volume-weighted density PDF, $dV_{\text{gas}}/d\log(n)$. Less than 1% of the volume has densities $n > 10 \text{ cm}^{-3}$. Both models are well fit by log-normal distributions, which peak at $\log(n \cdot \text{cm}^3) \simeq -1.34$ and -1.54 in the NoRPs and RPs respectively (dashed lines), though densities as high as $\log(n \cdot \text{cm}^3) \gtrsim -0.5$ are common.

important and the gas can no longer be held up by turbulence (Vázquez-Semadeni et al. 2008; Elmegreen 2011; Hopkins et al. 2012). Radiation pressure regulates the distribution of very dense, star-forming gas. As a result, the mass fraction of dense, self-gravitating gas in the power law tail is reduced by a factor of $\gtrsim 2$ in the RPs, consistent with the typical decrease in the amount of stars formed in the simulations (Fig. 3). The mass in the hot component, with $T > 10^6$ K (not shown), is roughly twice as high as in the RPs compared to the NoRPs. Similar results have been obtained in studies of isolated galaxy simulations (Hopkins et al. 2012; Rosdahl et al. 2015) and in one of the cosmological simulations used here (Ceverino et al. 2014).

Both distributions are attenuated at the highest densities of $\log(n \cdot \text{cm}^{-3}) \gtrsim 3.5 - 4$, with a slight tendency for a higher threshold in the RPs vs the NoRPs, and at lower redshifts. This is likely due to the pressure floor (eq. (1)), to which we can associate an effective velocity

$$\sigma_{\text{floor}} = \sqrt{\gamma \frac{P_{\text{floor}}}{\rho}} \simeq 120 n_4^{1/2} \Delta_{25} \text{ km s}^{-1} \quad (6)$$

where $n_4 = n/(10^4 \text{ cm}^{-3})$ and $\Delta_{25} = \Delta/(25 \text{ pc})$.⁸ In the RPs, the radial velocity dispersion, σ_r , is typically $\sim 50 \text{ km s}^{-1}$ before compaction and $\sim 100 \text{ km s}^{-1}$ after compaction (Zolotov et al. 2015, figure 11). So at densities of $n \sim (3 \times 10^3) - 10^4 \text{ cm}^{-3}$, the pressure

floor becomes comparable to the turbulent pressure, preventing cells from reaching higher densities.

The volume-weighted PDF is well fit by a log-normal in both NoRPs and RPs, with peak densities of $\log(n \cdot \text{cm}^3) \simeq -1.34$ and -1.54 respectively, and standard deviations of $\sigma_{\log(n)} \simeq 0.87$ and 0.72 . Dense gas, with $n \gtrsim 10 \text{ cm}^{-3}$ comprises less than 1% of the total volume. The volume filling factor of star-forming gas, with $n \gtrsim 1 \text{ cm}^{-3}$, is reduced by a factor of ~ 2 in the RPs, which in turn reduces the star formation in the RPs, as seen in Fig. 3. The hot component, with $T > 10^6$ K (not shown) occupies a comparable volume to the cooler component, despite containing only $\sim 1\%$ of the mass. The distribution of densities is also log-normal, with mean densities of $\log(n \cdot \text{cm}^3) \simeq -3$ and -3.4 in the NoRPs and RPs respectively, and corresponding standard deviations of $\sigma_{\log(n)} \simeq 0.57$ and 0.72 . The volume fraction of this hot gas is roughly 10 times higher in the RPs than in the NoRPs, showing that RP heats the gas and drives it to lower densities.

To summarise, we expect bound star-forming clumps to form at densities $n > 10 \text{ cm}^{-3}$, while most of the volume in the ISM is at densities of $10^{-3} \lesssim n \lesssim 1 \text{ cm}^{-3}$. Our threshold density residual for clump detection, $\delta_\rho^{\text{min}} = 10$ (§3.3), is thus well suited to detect the vast majority of clump candidates. Naturally, given the wide range of low densities, we also expect to detect many unbound, low density, transient structures, which form the bulk of the ZLCs discussed earlier.

⁸ The highest level of refinement is always reached for gas densities $n > 100 \text{ cm}^{-3}$ and often even at lower densities (§2.1).

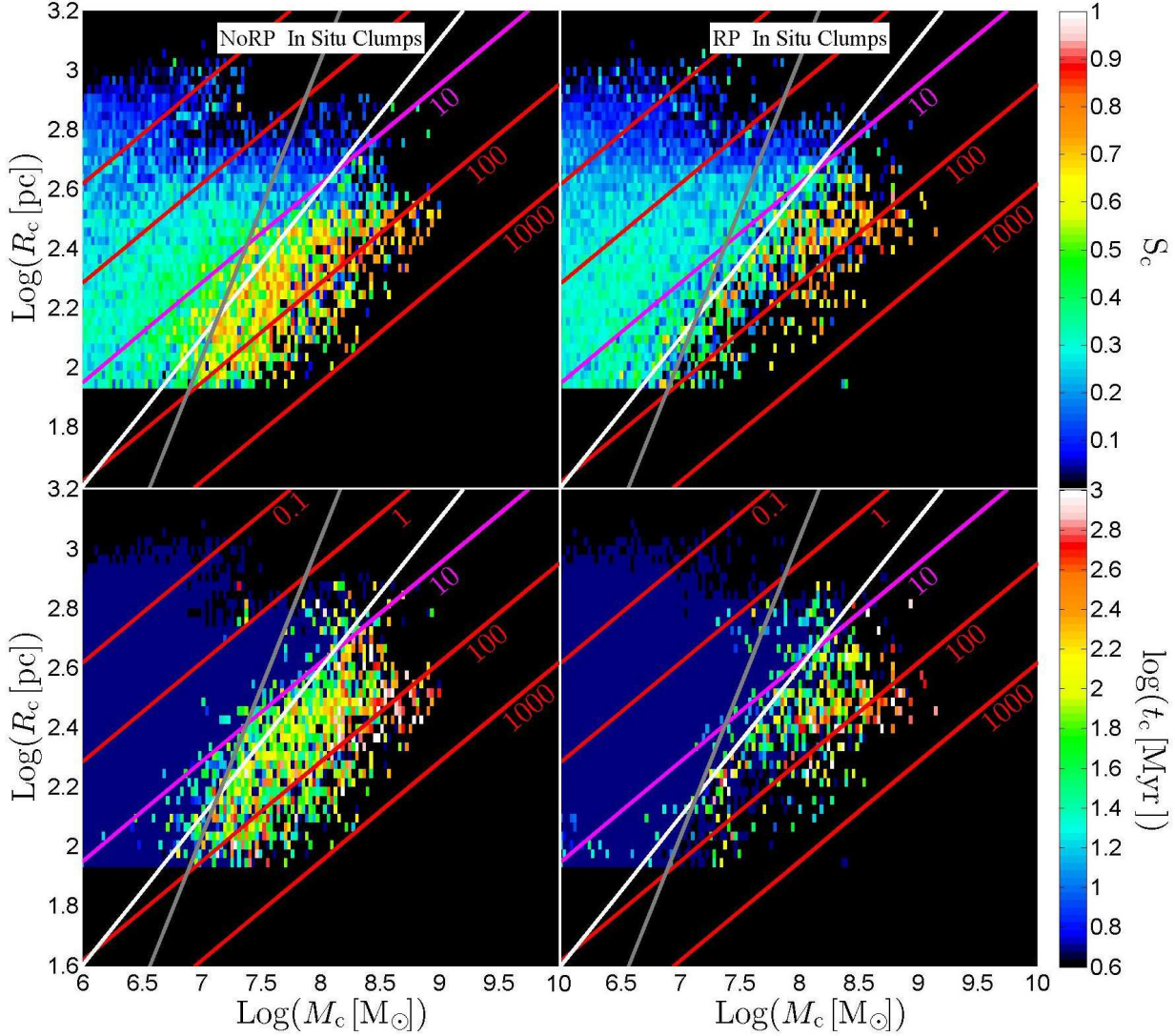


Figure 6. In situ clumps in NoRPs (left) and RPs (right). Each panel shows the distribution of clumps in the mass-radius plane. The red and magenta lines represent constant baryonic density, $n_{\text{bar}} \cdot \text{cm}^3 = 0.1 - 1000$ from top to bottom, as marked in the figure. In each panel, the grey line represents a constant circular velocity $V_{\text{circ}} = 20 \text{ km s}^{-1}$ while the white line represents a constant baryonic column density of $\Sigma_{\text{bar}} = 200 M_{\odot} \text{ pc}^{-2}$. The color bar in each panel represents the median value per pixel of the respective property. The top row refers to the clump shape parameter, S_c , and the bottom row to the clump time, t_c in Myr. Clumps with $t_c = 0$ were artificially set to dark blue so that they show up on the plot. Clumps do not have densities greater than $n_c \gtrsim 300 \text{ cm}^{-3}$, so the sample is complete at masses $M_c \gtrsim 10^{7.5} M_{\odot}$. In both feedback models, clumps with $t_c > 0$ are round/oblate with average densities $n_c \gtrsim 10 \text{ cm}^{-3}$. RP affects clumps with $M_c \lesssim 10^{8.3} M_{\odot}$, reducing their densities and making them more prolate, thus leading to their rapid disruption. More massive clumps are largely unaffected by the additional feedback. In NoRPs, the number of clumps with $t_c > 0$ declines for circular velocities $V_{\text{circ}} \lesssim 20 \text{ km s}^{-1}$, while in RPs it declines for surface densities $\Sigma \lesssim 200 M_{\odot} \text{ pc}^{-2}$.

5 THE EFFECT OF RADIATIVE FEEDBACK ON CLUMPS

In this section we examine the effect of RP feedback on the formation, lifetime, and properties of giant clumps in high- z disc galaxies. As in the previous section, we limit our analysis to the snapshots with both RP and NoRP versions, and discuss separately the effects on in situ, ex situ and bulge clumps.

5.1 In Situ Clumps

5.1.1 Mass-size plane and sample completeness

Figure 6 shows the distribution of in situ clumps in the mass-radius plane, for the NoRPs (left) and the RPs (right). In all panels, the color represents the median value within each pixel of a respective property. The top row shows the clump shape, S_c , and the bottom row shows the clump time, t_c . Cases where $t_c = 0$ were artificially assigned a value of $\log(t_c) = 0.7$ so that they appear on the plot in dark blue. The red and magenta lines represent constant baryonic volume densities of

$n_{\text{bar}} = 0.1 - 1000 \text{ cm}^{-3}$ as marked. RP feedback reduces the typical density of in situ clumps by roughly 0.5 dex, similar to the factor by which the typical ISM density (by volume) is reduced (Fig. 5, right). This is expected since we define clumps based on local overdensity.

It is clear from the distribution of pixels in each diagram that our sample of clumps is incomplete at masses $M_c \lesssim 10^{7.5} M_\odot$, due to our minimal clump volume, $V_{\text{min}} = 8 \times (70 \text{ pc})^3$. At a given mass, M_c , we can only resolve clumps with densities $n_c < M_c/V_{\text{min}}$. Due to the maximal ISM density we resolve, there is a maximal clump density, n_{max} , so that we are complete for all masses $M_c > V_{\text{min}} n_{\text{max}}$. For $M_c = 10^{7.5}$, $10^{7.2}$ and $10^7 M_\odot$, we can resolve all clumps with $n_c \lesssim 340$, 200 and 110 cm^{-3} respectively. We estimate the incompleteness at these three masses by calculating the fraction of clumps with $M_c > 10^{7.5} M_\odot$ that have densities above these thresholds. The corresponding fractions are $\sim 1\%$, 4% and 9% , and are very similar in both sets of simulations. We conclude that our sample is reasonably complete for clumps with $M_c \gtrsim 10^7 M_\odot$. Hereafter, when we discuss the sample of clumps, we refer only to this mass complete sample.

5.1.2 Clump lifetimes

From Fig. 6, we learn that clumps with $t_c > 0$ are rather round and oblate, $S_c \gtrsim 0.5$, and dense, $n_c \gtrsim 10 \text{ cm}^{-3}$. This corresponds to the scale where the ISM becomes self-gravitating, allowing clumps to collapse to bound, oblate, long-lived structures. At lower densities, turbulence prevents the clumps from collapsing, and they remain extended, typically prolate structures. Such structures are rapidly mixed back into the ISM through a combination of turbulence and shear, or are torn apart by tidal forces. The oldest clumps are typically $\sim 300 - 500 \text{ Myr}$ old, comparable to the expected migration time for clumps in high redshift discs (Dekel, Sari & Ceverino 2009). This will be discussed further in §6.2.

Figure 7 shows the distribution of clump lifetimes in the NoRPs (blue) and the RPs (red). The y axis shows the average number of clumps per snapshot per bin of $\log(t_{c, \text{max}})$, shown on the x axis. The clump lifetime has been normalized by the mass-weighted average free-fall time during its lifetime

$$t_{\text{ff}} = \sqrt{\frac{3\pi}{32G\rho}} \simeq \frac{0.54}{\sqrt{G\rho}} \quad (7)$$

There is a bi-modal distribution with a minimum near $t_{c, \text{max}} \simeq 20t_{\text{ff}}$. This is in the ball park of the output time step in the simulations, and it can therefore separate clumps that were identified in one or multiple snapshots. We also note that $t_{c, \text{max}} \simeq 20t_{\text{ff}}$ is the maximal clump lifetime observed in isolated galaxy simulations with much stronger radiative feedback (Hopkins et al. 2012). We therefore use this threshold to distinguish short-lived clumps (SLCs) from long-lived clumps (LLCs). In both sets of simulations, only $\sim 6\%$ of clumps that can be tracked for more than one

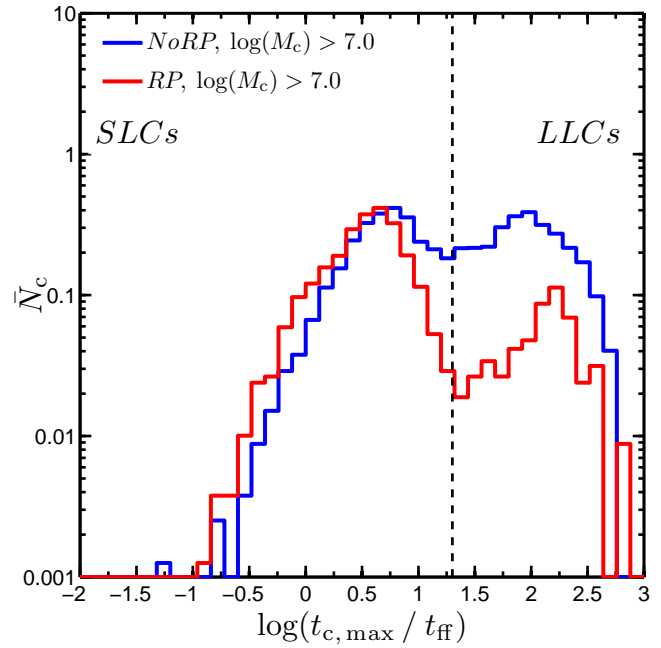


Figure 7. Distribution of clump lifetimes, $t_{c, \text{max}}$, normalized to the (mass-weighted average) clump free fall time, $t_{\text{ff}} \simeq 0.54/\sqrt{G\rho}$. Blue (red) curves show the distribution for NoRPs (RPs). There is a bi-modal distribution, separated at $t_{c, \text{max}} \sim 20t_{\text{ff}}$ as marked by the vertical dashed line, which distinguishes short-lived (SL) from long-lived (LL) clumps. The RPs have $\sim 54\%$ as many clumps as the NoRPs, but only $\sim 19\%$ as many LLCs.

timestep fall into the SLC category, and these make up less than 1% of the SLCs themselves.

Ignoring ZLCs, the RPs have $\sim 54\%$ as many clumps as the NoRPs, and $\sim 19\%$ as many LLCs. In the NoRPs, $\sim 49\%$ of clumps are LLCs compared to only $\sim 17\%$ in the RPs. We conclude that RP has a minor effect on clump formation, but it dramatically reduces the number of long-lived clumps.

5.1.3 Clump structural and virial properties

In Fig. 8, we compare structural and virial properties of clumps in the RPs and NoRPs, to try and discern what causes clump disruption. In each panel we show the distribution of a different property, represented on the x axis, where the y axis shows the average number of clumps per snapshot per bin of x , as in Fig. 7. In clockwise order from the top left the properties are clump shape, S_c ; mass, M_c ; circular velocity, $V_{\text{circ}, c} = \sqrt{GM_c/R_c}$; surface density, $\Sigma_c = M_c/(\pi R_c^2)$; volume density, $n_c = 3M_c/(4\pi R_c^3)$; and virial parameter $\alpha_v = 2E_K/|U|$, i.e. twice the ratio of kinetic to potential energies within the clump. For each property, we show the distributions including ZLCs, the distributions for non-ZLCs, and the distributions for LLCs only, as marked in the legend.

The virial parameter is measured in a sphere of radius R_c centered on the peak baryonic density within the clump. This is a valid approximation for nearly spherical clumps and can serve as an order of magnitude

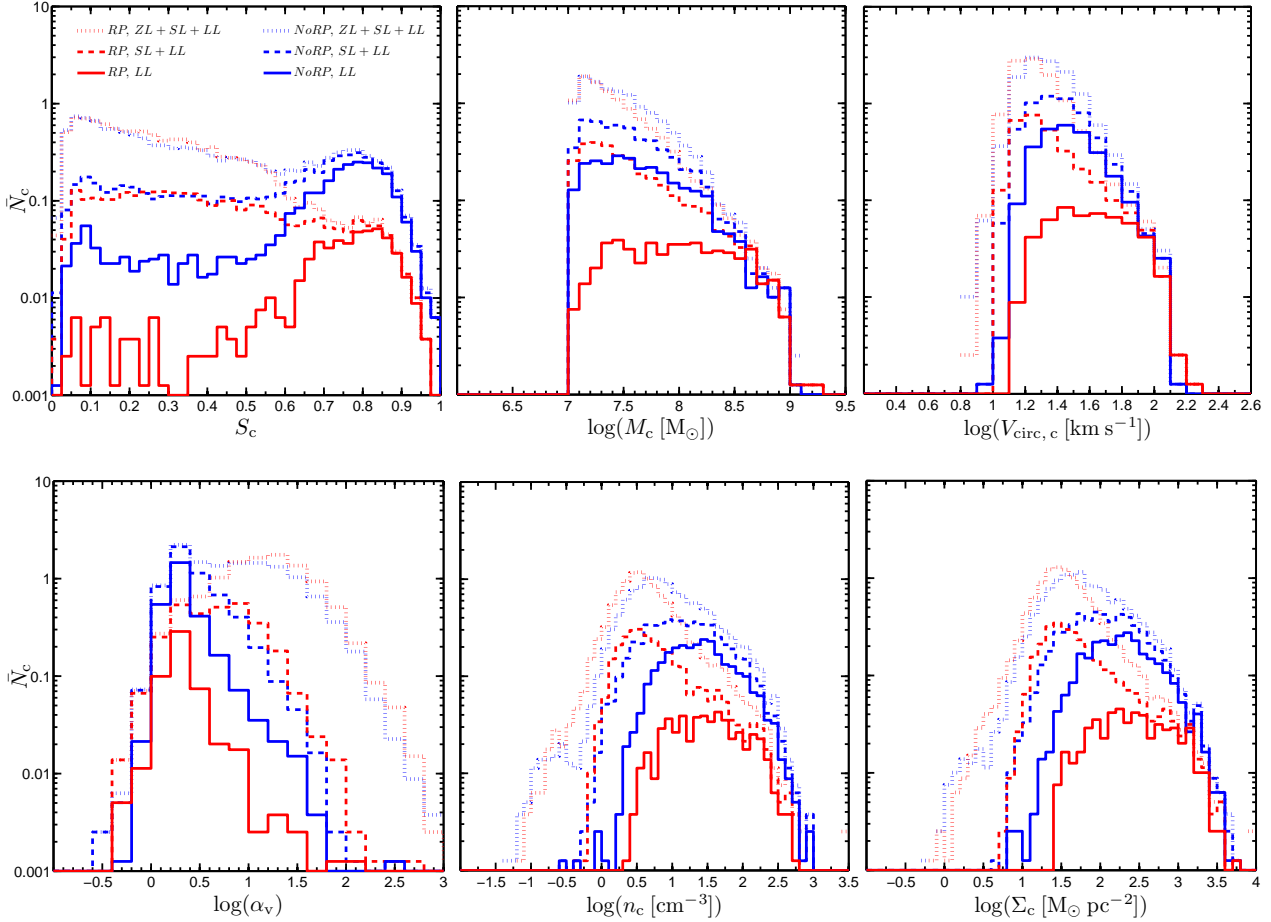


Figure 8. Properties of clumps in NoRP vs. RPs. In each panel we show the distribution of a different property, x , among in situ clumps in the simulations. The y axis is the average number of clumps per snapshot per bin of x . In all panels, the blue/red lines show the distributions for NoRPs/RPs respectively. The dotted lines refer to all clumps including ZLCs, the dashed lines refer to non-ZLCs with $t_{c, \max} > 0$, and the solid lines refer to LLCs only. *Top left:* Clump shape, S_c . *Top centre:* Clump mass, M_c . *Top right:* Clump circular velocity, $V_{\text{circ}, c} = \sqrt{GM_c/R_c}$. *Bottom left:* Clump virial parameter $\alpha_v = \sigma^2 R_c / (GM_c)$. *Bottom centre:* Clump baryonic volume density, $n_c = 3M_c / (4\pi R_c^3)$. *Bottom right:* Clump baryonic surface density, $\Sigma_c = M_c / (\pi R_c^2)$. The ZLCs have low densities and elongated shapes and are clearly unbound with $\alpha_v \sim 10 - 1000$. LLCs typically have densities $n_c \gtrsim 10 - 30$ and are oblate or close to spherical, in agreement with Fig. 6. Most of them are close to virial equilibrium, with $\alpha_v \sim 1 - 3$. RP feedback rapidly unbinds clumps with surface densities below $\sim 30 M_\odot \text{pc}^{-2}$, and these SLCs have virial parameters $\alpha_v \sim 3 - 30$. Clumps with $\Sigma_c \gtrsim 300 M_\odot \text{pc}^{-2}$, more massive than $\sim 10^{8.5} M_\odot$, appear unaffected by RP, while clumps with $V_{\text{circ}, c} \lesssim 20 \text{ km s}^{-1}$ are rapidly disrupted even in NoRPs.

estimate for elongated clumps as well. In the rest-frame defined by the center of mass velocity of baryons within the sphere, we measure the total baryonic kinetic energy, which gives us the mass-weighted 3D velocity dispersion, $\sigma^2 = 2E_K / M_c$. The virial parameter is

$$\alpha_v = a \frac{\sigma^2 R_c}{GM_c}, \quad (8)$$

where a is a constant of order unity that depends on the density profile within the clump. If the density profile is a power law in the clump-centric radius, $\rho \propto r^{-\beta}$, then

$$a = \frac{5 - 2\beta}{3 - \beta}. \quad (9)$$

For a constant density sphere, $\beta = 0$ and $a = 5/3$. Previous studies of clumps in similar simulations to the ones used here as well as high-resolution simulations of isolated galaxies suggest that most clumps can be

well approximated as having $\beta = 2$ (Ceverino et al. 2012). We adopt this approximation, which yields $a = 1$ and $\alpha_v = \sigma^2 R_c / (GM_c)$, i.e. 0.6 times the value for a constant density sphere.

The ZLCs comprise the majority of the sample, $\sim 84\%$ and $\sim 74\%$ in the RPs and NoRPs respectively. However, they are characterised by low masses and densities, filamentary shapes, and very large virial parameters, $\alpha_v \sim 10 - 1000$, well above the SLCs which have $\alpha_v \sim 3 - 30$. We conclude that the majority of ZLCs are slightly overdense patches of the disc, expected in any turbulent medium, and were not at any point gravitationally bound clumps. We hereafter ignore them, and use “clumps” to refer only to SLCs and LLCs, with masses $M_c > 10^7 M_\odot$.

LLCs appear to be close to virial equilibrium, with $\alpha_v \sim 1 - 3$. Had we assumed a slope of $\beta = -2.3$ rather than -2 for the density profile, the peak of the

distribution would have been at $\alpha_v = 1$. Other studies which have claimed that all clumps are short-lived (Hopkins et al. 2012; Oklopčić et al. 2016) measured the virial parameters of clumps in their simulations assuming constant density, i.e. $\beta = 0$. They found that all clumps have $\alpha_v > 1$, while many have $\alpha_v \lesssim 3$, and claim this shows all clumps to be unbound. In our case, assuming $\beta = 0$ shifts the peak of the distribution for LLC to $\alpha_v = 3$, consistent with these other studies. This shows that it is important to account for the density profile in the clump when using the virial parameter to assess whether or not the clump is bound.

LLCs have a strong tendency to be oblate or spherical, as we saw as well in Fig. 6. In both RPs and NoRPs, clumps with $S_c \gtrsim 0.8$ are almost all long-lived, while clumps with $S_c \lesssim 0.6$ are almost all short-lived. Since clump shape correlates with density so that rounder clumps are denser, the LLCs are less prone to disruption by shear and tidal forces within the disc.

Very massive clumps, with $M_c \gtrsim 10^{8.5} M_\odot$, are unaffected by the inclusion of RP. The number of such clumps is the same in the NoRPs and RPs, and $\sim 76\%$ of them are long-lived. Below this mass, there are fewer clumps in the RPs, and the slope of the mass function is slightly shallower. This is in qualitative agreement with the shallower slope in the high density power-law tail of the ISM mass-weighted density PDF (Fig. 5). Below $\log(M_c) \sim 7.3$, the SLC mass function flattens and the number of LLCs begins to decline. This must be due in part to incompleteness, though there may be an additional physical effect disrupting clumps below this mass scale even without RP, as discussed below.

Due to an overall decrease in densities, clumps in RPs have shallower potential wells, making them more susceptible to ejective feedback from supernova. The number of LLCs begins to decline at $V_{\text{circ}} \lesssim 25 \text{ km s}^{-1}$, suggesting a typical scale for clump disruption by SN feedback. In the range $40 \lesssim V_{\text{circ}} \lesssim 65 \text{ km s}^{-1}$, nearly all clumps in the NoRPs are long-lived while there is a non-negligible fraction of SLCs in the RPs. This suggests that RP feedback boosts the efficiency of supernova feedback, by lowering the typical densities.

When RP is included, there are fewer very dense clumps, consistent with the overall decrease in ISM densities. Most LLCs have densities $n_c \sim 10 - 30 \text{ cm}^{-3}$, as expected from the power-law portion of the ISM density PDF (Fig. 5), though densities in the range $n_c \sim 3 - 200 \text{ cm}^{-3}$ are common. Nearly all clumps with densities greater than $\sim 50 \text{ cm}^{-3}$ or surface densities greater than $\sim 300 M_\odot \text{ pc}^{-2}$ are LLCs, in both RP and NoRPs. On the other hand, in the RPs there is a sharp decrease in the number of LLCs with surface densities below $\sim 30 M_\odot \text{ pc}^{-2}$.

5.1.4 Clump disruption scale

The grey lines in each panel of Fig. 6 represent a constant circular velocity of $V_{\text{circ}} = 20 \text{ km s}^{-1}$. This seems to mark a transition between ZLCs and non-ZLCs in the NoRPs (bottom left panel), seen

as well in the top-right panel of Fig. 8. Based on Dekel & Silk (1986), Dekel, Sari & Ceverino (2009) showed that if the star-formation efficiency per free-fall time in the clump is $\epsilon_{\text{ff}} \sim 10\%$, then clumps with circular velocities $V_{\text{circ}} \lesssim 30 \text{ km s}^{-1}$ can be disrupted by supernova feedback. In our simulations, the star formation efficiency averaged over clumps is typically $\epsilon_{\text{ff}} \sim 0.03 - 0.04$, though values as high as 10% are not uncommon. This yields a minimum potential depth of $V_{\text{circ}} \sim 20 - 30 \text{ km s}^{-1}$ below which clumps should be susceptible to ejective feedback from supernova, which may explain why the number of LLCs decreases below this value even in NoRPs.

This may also be related to the decrease in the number of LLCs below $M_c \sim 10^{7.3} M_\odot$ (Fig. 8). On the one hand, clumps must have $V_{\text{circ},c} = \sqrt{GM_c/R_c} \gtrsim 20 \text{ km s}^{-1}$ to survive. On the other hand, the self-gravitating regime of the ISM is at densities $n_c = 3M_c/(4\pi R_c^3) \gtrsim 10 \text{ cm}^{-3}$ and the number of LLCs declines towards lower densities (Fig. 8). These two scales meet at a unique mass, which is $M_c \simeq 10^{7.4} M_\odot$. At lower masses, clump survival is limited by the potential-well $\propto M_c/R_c$, while at higher masses the clumps are limited by density $\propto M_c/R_c^3$, resulting in a kink in the mass function. Unfortunately, as this is very close to our incompleteness limit, it is difficult to draw firm conclusions from the simulations.

When RP is included, clump survival becomes limited by surface density. This is apparent in Fig. 6, where the white lines mark a constant surface density of $\Sigma_c = 200 M_\odot \text{ pc}^{-2}$, and the number of non-ZLCs in the RPs sharply declines to the left of this line (bottom right panel). Figure 8 shows that above $\Sigma_c = 300 M_\odot \text{ pc}^{-2}$, nearly all clumps are long lived while there are hardly any LLCs with $\Sigma_c < 30 M_\odot \text{ pc}^{-2}$. A clump with $\Sigma_c = 300 M_\odot \text{ pc}^{-2}$ and $n_c = 10 \text{ cm}^{-3}$ has a mass of $M_c \sim 10^{8.5} M_\odot$, explaining why above this mass, nearly all clumps are long-lived.

To get a rough understanding of where this scale comes from, we consider the very simple case of a clump of mass M and radius R that forms stars in a single burst in a small region at its centre, and ask when the radiation pressure from this burst is enough to unbind the remaining clump. Equating the inward gravitational force acting on a spherical shell at radius R to the outward force of the radiation pressure, assuming a single scattering per photon, yields the equation

$$\frac{GM}{R^2} = \frac{L}{4\pi R^2 c \tilde{\Sigma}} \quad (10)$$

where $\tilde{\Sigma} = M/(4\pi R^2)$ is the mass per unit area which the radiation is pushing. This yields a critical surface density of

$$\Sigma = 4\tilde{\Sigma} = \frac{L}{M\pi Gc} = \frac{\Gamma f_*}{\pi Gc} \simeq 380 f_* M_\odot \text{ pc}^{-2} \quad (11)$$

where $\Gamma = 10^{36} \text{ erg s}^{-1} M_\odot^{-1}$ is the parameter used in our simulations (eq. (4)), and $f_* = M_*/M$ is the fraction of the clump mass turned into stars. Clumps with $\Sigma \sim 30 M_\odot \text{ pc}^{-2}$ become unbound after turning only $\sim 10\%$ of their mass into stars, while clumps with

$\Sigma \sim 200M_{\odot} \text{ pc}^{-2}$ are able to turn half their mass into stars before blowing out the remaining gas, allowing them to remain bound.

This model is too simplistic because the radiation pressure in the simulations only affects the cells neighbouring star particles younger than 5 Myr old, and not all the stars form in a single cell in a single timestep. In addition, the clump is non-spherical, the medium is non-uniform and supersonic turbulence also adds effective pressure as does the net effect of supernova feedback. Nevertheless, this crude estimate gives a sense for the range of surface densities observed in LLCs. We also note that more realistic models which estimate the scale for rapid disruption of giant clumps assuming weak radiation trapping (e.g. Krumholz & Dekel 2010, and references therein), also predict that clumps with $\Sigma \gtrsim 100M_{\odot} \text{ pc}^{-2}$ and $M_c \gtrsim 10^{7.5}$ with $\epsilon_{\text{ff}} \sim 0.03$ are rapidly disrupted, while clumps with $\Sigma \gtrsim 300M_{\odot} \text{ pc}^{-2}$ and $M_c \gtrsim 10^{8.5}$ are not.

To summarise, bound star-forming clumps only form at densities $n_c \gtrsim 10 \text{ cm}^{-3}$ where the ISM is self-gravitating. Clumps with $V_{\text{circ}, c} \lesssim 20 \text{ km s}^{-1}$ are rapidly disrupted by ejective feedback from supernovae, and in the RPs, clump disruption can occur even $V_{\text{circ}, c} \lesssim 40 \text{ km s}^{-1}$. Radiation pressure introduces a critical surface density for clump survival, where clumps with $\Sigma_c < 30M_{\odot} \text{ pc}^{-2}$ are rapidly disrupted, while clumps with $\Sigma_c > 300M_{\odot} \text{ pc}^{-2}$ are all long lived. The interplay between these three scales results in a kink in the clump mass function at $M_c \sim 10^{7.3}M_{\odot}$ and in massive clumps with $M_c \gtrsim 10^{8.5}$ being long-lived. However, we note that the number of LLCs in the NoRPs decreases below $\Sigma_c \sim 30M_{\odot} \text{ pc}^{-2}$ as well, albeit less sharply than in the RPs, since these clumps also have circular velocities close to the threshold. It is therefore difficult to quantitatively assess to what extent RP feedback alters the fundamental physical property responsible for clump disruption.

5.2 Bulge and Ex Situ Clumps

RP has little effect on the central bulge clumps. A central clump is identified in $\sim 83\%$ (96%) of all galaxies in the RPs (NoRPs) respectively, and in $\sim 97\%$ (100%) of the galaxies at $z < 4$. Nearly all the bulge clumps have high densities and masses, $n > 10 \text{ cm}^{-3}$ and $M_c > 10^{8.5}$, and are thus largely unaffected by the RP feedback, showing similar distributions in both sets of simulations. Their typical masses are $\sim 10^{9.5}M_{\odot}$, or $\sim 0.3 - 0.5M_{\text{d}}$, and their typical SFRs are $\sim 0.5\text{SFR}_{\text{d}}$.

On the other hand, RP feedback greatly reduces the number of ex situ clumps. Ex situ clumps are merging galaxies, and we may have expected similar numbers in the two sets of simulations, since the cosmic evolution is meant to be the same. However, even among very massive clumps with $M_c > 10^{8.5}M_{\odot}$ in baryons, which based on the fate of the in-situ clumps with such high masses are not expected to be strongly affected by RP, there are ~ 3.5 times as many ex situ clumps in the NoRPs. The reduction in the number of ex situ clumps likely results from RP acting on these merging dwarf

galaxies at early times, when they were less massive, and puffing them up. The increased feedback causes more intense outflows and lowers the central densities of the merging galaxies, making them more vulnerable to tidal stripping as they merge with the main host. A detailed study of the evolution of these ex situ clumps is beyond the scope of this paper.

Ex situ clumps are $\sim 10\%$ and $\sim 5\%$ of the off centre clumps in number, $\sim 35\%$ and $\sim 37\%$ in mass and $\sim 15\%$ and $\sim 29\%$ in SFR in the NoRPs and RPs, respectively. Among the most massive clumps with $M_c > 10^{8.5}M_{\odot}$, the ex situ contribution increases to $\sim 58\%$ and $\sim 36\%$ in number, $\sim 75\%$ and $\sim 60\%$ in mass, and $\sim 51\%$ and $\sim 56\%$ in SFR. This is comparable to the ex situ contribution found by M14, where the simulated galaxies were more massive by a factor of $\sim 5 - 10$, and the typical clump mass was $M_c \gtrsim 10^8M_{\odot}$.

6 PROPERTIES OF CLUMPS IN RP SIMULATIONS

In this section we study physical properties of clumps that may be related to observations. We focus on the RPs as a better representation of the real Universe, and therefore use the full RP sample which consists of 1130 snapshots: 320 at $4 \leq z$, 161 at $3 \leq z < 4$, 241 at $2 \leq z < 3$, 408 at $0.75 \leq z < 2$.

6.1 Mass Functions and SFR Functions

Figure 9 shows the distribution of masses and SFRs for in situ clumps normalized to the corresponding values in their host discs, $m \equiv M_c/M_{\text{d}}$ and $s \equiv \text{SFR}_c/\text{SFR}_{\text{d}}$, for different redshift bins. While we refer here to the clump baryonic mass, we note that the stellar mass functions are rather similar, especially at $z < 3$.

The peak of the mass function decreases from $\log(m) \sim -2.5$ at $z > 3$ to ~ -3.5 at $z < 2$. While this roughly coincides with the predicted fragmentation mass relative to the disc mass of δ_{cold}^2 (Dekel, Sari & Ceverino 2009), it seems likely that the peak in the mass function is due to the fact that our disc masses grow monotonically in time, while the minimal resolved clump mass remains fixed. Thus the characteristic value of m becomes smaller at later times. In the range $-2 \lesssim \log(m) \lesssim -1$, where we are complete, the mass function can be described by a power-law, $dN/dm \propto m^{-\alpha}$ with $\alpha \sim 1.7 - 1.8$, roughly independent of redshift. This is similar to observed slopes of GMC mass functions in the local galaxies (e.g. Williams & McKee 1997; Rosolowsky 2005). Note that a mass function with a slope of $\alpha = -2$ has equal mass on all scales, and tends to emerge generically in systems dominated by gravitational collapse (e.g. Press & Schechter 1974; Bond et al. 1991; Hopkins 2013).

The distribution of SFR is broader, though it exhibits the same general shape as the mass function. The overall behaviour appears similar at all redshifts,

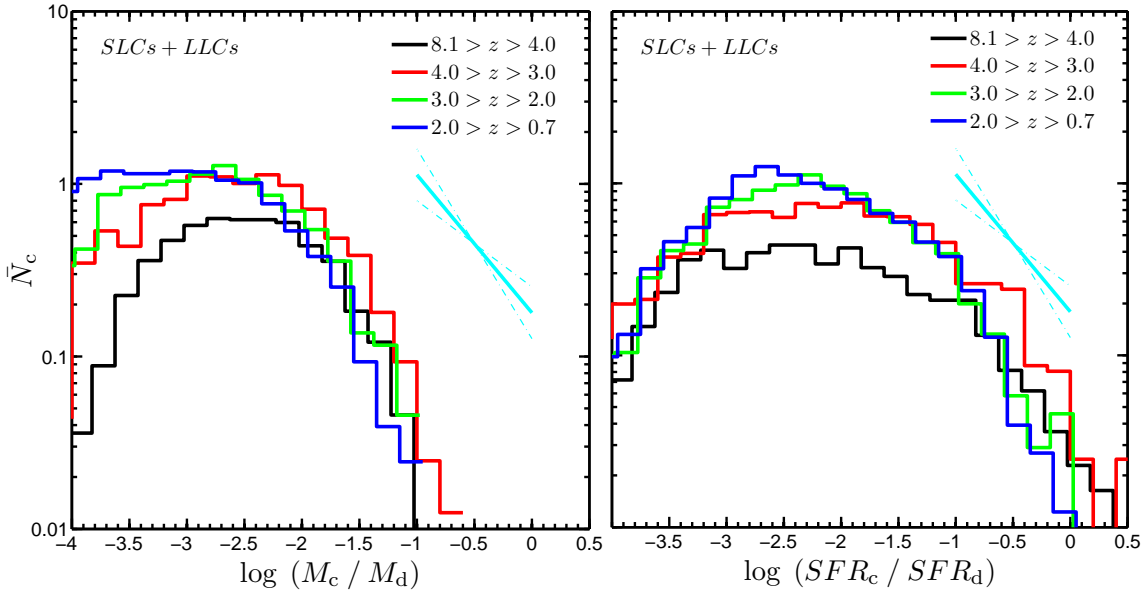


Figure 9. Mass function and SFR function for in situ clumps in the RPs. The x axes show the clump mass normalized to the disc mass, $m = M_c/M_d$ (left), and the clump SFR normalized to the disc SFR, $s = SFR_c/SFR_d$ (right). The y axis shows the average number of clumps per snapshot per logarithmic interval of x . Different colours represent different redshift bins, as marked in the legend. The cyan lines mark slopes of $\alpha = 1.5, 1.8, 2.1$ where $dN/dx \propto x^{-\alpha}$. The peak of the mass function decreases from $\log(m) \sim -2.5$ at $z > 3$ to ~ -3.5 at $z < 2$, likely due to the fact that our disc masses grow monotonically in time, while the minimal resolved clump mass remains fixed. In the range $-2 \lesssim \log(m) \lesssim -1$ the mass function can be described by a power-law with a slope slightly shallower than -2 , and independent of redshift. The overall behaviour of the SFR function appears similar at all redshifts, and is nearly identical in the two latest redshift bins, at $2 < z < 3$ and $z < 2$ (green and blue lines respectively). The peak is shifted slightly from $\log(m) \sim -2$ at $z > 3$ to ~ -2.5 at $z < 2$, though as with the mass function, this peak may be due to our limited resolution for clump detection while our galaxies grow monotonically with time. At values of $-2 \lesssim \log(s) \lesssim -1$, the distribution can be described as a power law with a slope slightly shallower than -2 , while the relation steepens at $-1 \lesssim \log(s)$.

and is nearly identical in the two latest redshift bins, $2 < z < 3$ and $z < 2$ (green and blue lines respectively). The peak decreases slightly with time, from $\log(m) \sim -2$ at $z > 3$ to ~ -2.5 at $z < 2$, though as with the mass function, this may be due to our limited resolution for clump detection while our galaxies grow monotonically with time. At values of $-2 \lesssim \log(s) \lesssim -1$ the distribution can be described as a power law with a slope of ~ -1.6 , slightly shallower than the mass function, though this steepens towards higher values. The maximal value of s seems to decrease by ~ 0.5 dex from $4 < z$ to $z < 2$, indicating that individual giant clumps contribute less to the total SFR at later times. Values of $\log(s) > 0$ can occur if clumps are not co-rotating with the disc, so that their stars are not considered “disc stars” with $j_z/j_{\max} > 0.7$ and therefore are not counted towards the disc SFR. Associating SFR with UV luminosity, our SFR functions can be compared with observed UV luminosity functions of clumps. At $z < 3$, more than 60% of the clumpy galaxies in our sample have $9.8 < \log(M_d) < 10.6$, and our SFR function is similar to the UV luminosity function of clumpy galaxies in the same mass and redshift ranges (Guo et al. 2015, figures 7-9).

6.2 Migration of Long-Lived Clumps

M14 predicted gradients in clump properties such as mass, stellar age and sSFR, with galactocentric distance due to clump migration. Observations of such gradients by Förster Schreiber et al. (2011) and Guo et al. (2012) have been interpreted as evidence of clump survival and migration in real galaxies. However, M14 did not track clumps in time and did not directly address gradients that may be present in the properties of SLCs at birth, due to gradients in the underlying disc properties. Here, we are able to directly compare LLCs and SLCs, and determine stronger observational constraints for the clump migration scenario. We also examine properties of the ex situ clump population and address differences between in situ and ex situ clumps.

6.2.1 Sample selection

We restrict our analysis in this section to the mass limited sample of clumps with $M_c > 10^7 M_\odot$. This selection leaves $\sim 92\%$ of LLCs, but only $\sim 30\%$ of SLCs and $\sim 32\%$ of ex situ clumps.

Furthermore, since the time between consecutive snapshots, $\Delta a = 0.01$, is a larger fraction of the disc dynamical time at earlier times, our ability to track clumps for multiple timesteps and properly distinguish LLCs from SLCs becomes compromised at

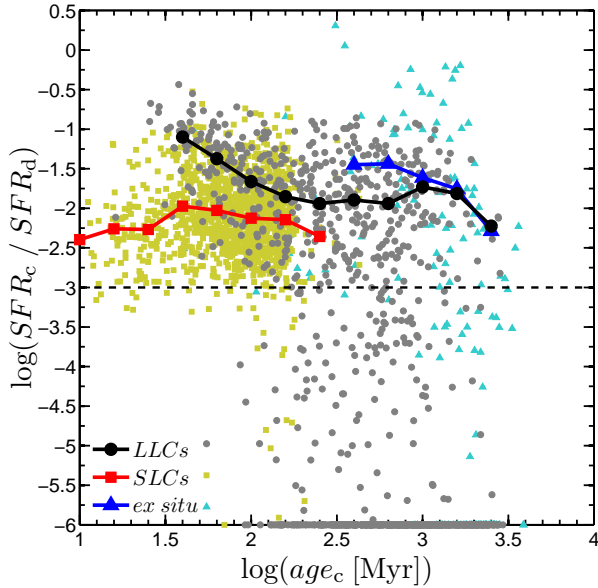


Figure 10. Clump SFR normalized to disc SFR, $s = SFR_c/SFR_d$, as a function of clump stellar age. Shown are LLCs (grey circles), SLCs (orange squares) and ex situ clumps (blue triangles), with masses $M_c > 10^7 M_\odot$ in discs with masses $M_d > 10^{10} M_\odot$ at redshifts $z < 2.5$. Clumps with $s = 0$ have been artificially placed at $\log(s) = -6$ so they show up on the plot. The horizontal dashed line at $\log(s) = -3$ marks our distinction between star-forming and quenched clumps. The thick black, red, and blue lines show the median values of $\log(s)$ in bins of stellar age for the LLCs, SLCs, and ex situ clumps respectively. Only star-forming clumps with $\log(s) > -3$ were considered when computing the medians. The bins have $\Delta \log(\text{age}_c) = 0.2$ and the centres have been marked with corresponding symbols. We only include bins that contain at least 7 clumps. SLCs typically contribute $\sim 1\%$ of the disc SFR, with no significant age dependence, but with a large scatter of ± 0.5 dex. Young LLCs outshine SLCs, each contributing $\gtrsim 10\%$ of the disc SFR, but their SFR declines roughly as $\text{age}^{-1.5}$ and after ~ 100 Myr they saturate at $\sim 1.5\%$, slightly higher than the median SLC. Ex situ clumps have ages of ~ 1 Gyr with a very wide range of SFR.

high redshifts. To avoid this issue, we limit our analysis to $z < 2.5$, where the time between snapshots is roughly half an orbital time at the disc edge, and LLCs can be followed for an average of 3 – 4 timesteps. This reduces the mass limited sample of LLCs by only $\sim 6\%$, consistent with our concern that properly identifying LLCs is more difficult at high redshift. The mass limited samples of SLCs and ex situ clumps are reduced by a further $\sim 34\%$ and $\sim 23\%$ respectively.

We reduce the sample further by only examining clumps in massive discs with $M_d > 10^{10} M_\odot$. This disc mass roughly corresponds to the transition between pre-compact and post-compact galaxies. Each galaxy in these simulations undergoes at some point one or more compaction events, where large amounts of gas flow towards the disc centre and lead to a compact starburst (a “blue” nugget). This is followed by gas depletion from the central galaxy and the formation of an extended, massive star-forming ring (Zolotov et al. 2015; Tacchella et al. 2016a,b). This event marks major

changes in galaxy properties and disc properties, and may well lead to systematic differences in clump properties. A detailed comparison of pre-compact and post-compact VDI is beyond the scope of this paper and is left for future work. To avoid this distinction, we limit our analysis to post-compact discs, approximated here as $M_d > 10^{10} M_\odot$. This has a small affect on the LLC sample, reducing it only by an additional $\sim 4\%$. The SLC and ex situ samples are reduced by a further $\sim 37\%$ and $\sim 34\%$ respectively.

Finally, we further reduce the sample to account only for star-forming clumps. From Fig. 9 we see that many clumps have very low SFRs, well below the total disc SFR. Since observations target star-forming clumps, we wish to remove quenched clumps from the sample. In Fig. 10 we show the SFR in clumps normalized to the disc SFR, $s = SFR_c/SFR_d$, as a function of the mean stellar age in the clump. We separate LLCs, SLCs and ex situ clumps according to the legend. Focusing on the LLCs, it is evident that there is a star-forming sequence and a population of quenched clumps with ages greater than 100 – 200 Myr. The row of points at $\log(s) = -6$ represents upper limits for clumps with even lower SFRs. Most quenched clumps consist of relatively low mass LLCs that have very perturbed orbits taking them to large distances from the disc plane. These clumps often have average gas densities below the threshold density for star-formation, $n_{\text{gas},c} \lesssim 1 \text{ cm}^{-3}$, which artificially results in $s = 0$. These clumps can survive for very long timescales of several Gyr and many of them have not yet migrated to the disc centre at $z = 1$. It is possible that these clumps may evolve to become globular clusters at $z \sim 0$ as proposed by Shapiro, Genzel & Förster Schreiber (2010). However, the study of quenched clumps is beyond the scope of this paper, which focuses on the star-forming clumps that are observed at high- z . We defer the study of quenched clumps to future work, selecting here only star-forming clumps with $\log(s) > -3$. Selecting clumps with gas mass $M_{\text{gas},c} > 10^6 M_\odot$ or gas density $n_{\text{gas},c} > 1 \text{ cm}^{-3}$ both result in very similar populations. This removes an additional $\sim 43\%$ of the LLCs and $\sim 56\%$ of the ex situ clumps, but only $\sim 4\%$ of the SLCs.

To summarize, we select star-forming clumps with $SFR_c > 10^{-3} SFR_d$, in a mass limited sample with $M_c > 10^7 M_\odot$, in massive post-compact discs with $M_d > 10^{10} M_\odot$ at redshifts $z < 2.5$. Counting each appearance of every clump as an independent measurement, separated by roughly half a disc orbital time, our final sample (hereafter referred to as our “clean sample”) consists of 85 ex situ clumps, 1209 SLCs, and 461 LLCs. However, the number of unique clumps in the sample is 56 ex situ clumps, 1086 SLCs and 150 LLCs.

We note that since most observations tend to target UV bright clumps, this can introduce a bias in their sample of clumps. We discuss this in §B.

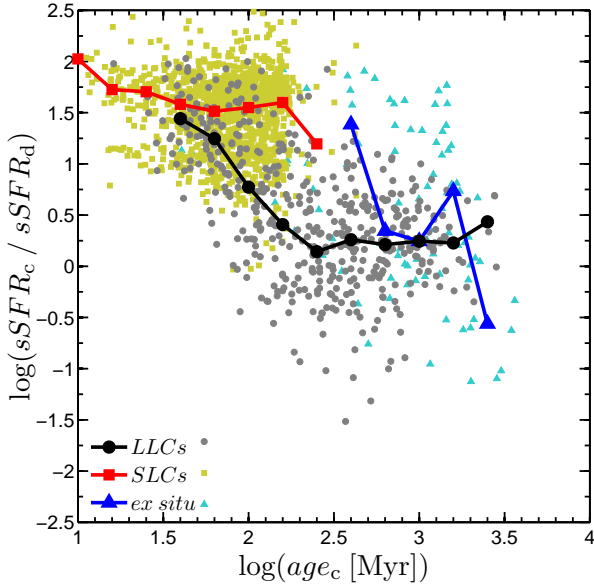


Figure 11. sSFR in clumps normalized to the disc value for our clean sample. Symbols and lines are the same as in Fig. 10. SLCs have very high sSFR, ~ 10 – 100 times higher than their host disc, with a median ratio of ~ 30 , and no dependence on stellar age. The youngest LLCs have similar values, but their sSFR decreases rapidly, scaling roughly as age^{-2} , and is $\lesssim 2$ times the disc average after ~ 100 – 200 Myr. Ex situ clumps have old ages of ~ 0.5 – 1 Gyr and a wide range of sSFR values, though the median is similar to LL in situ clumps.

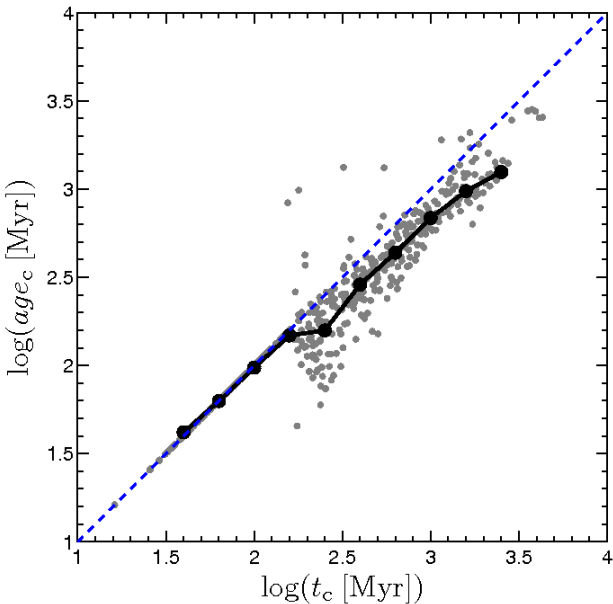


Figure 12. Mass-weighted mean stellar age in clumps as a function of clump time, for the LLCs in our clean sample. Grey points and the black line and symbols are the same as in Fig. 10. The blue dashed line corresponds to $age_c = t_c$. In the first timestep when the clump is identified, t_c is set to the stellar age by construction. In later timesteps, the stellar age is typically ~ 0.1 – 0.2 dex lower than the actual time since clump formation, due to continued star-formation and stripping of old stars.

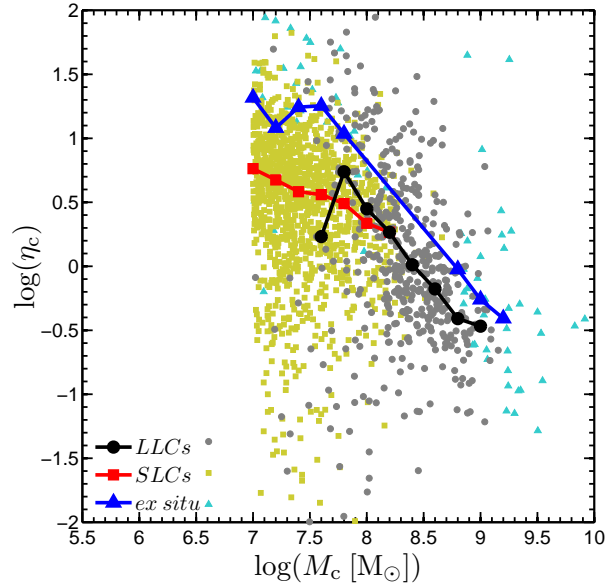


Figure 13. Outflows from clumps. We show the mass loading factor, $\eta = \dot{M}_{\text{gas, out}}/\text{SFR}$, for clumps as a function of clump mass, M_c . Symbols are the same as in Fig. 10 and the lines show the medians in bins of $\log(M_c)$. Most clumps with $M_c \gtrsim 10^8 M_\odot$ are long-lived. The mass loading factor tends to decrease with mass, though the scatter is extremely large, especially for the SLCs. Massive LLCs, $M_c \lesssim 10^{8.5} M_\odot$, have mass loading factors $\eta \sim 0.3$ – 3 , with a median value of ~ 1 . The most massive clumps with $M_c \sim 10^9 M_\odot$ exhibit smaller values, $\eta \sim 0.2$ – 2 , with a median of ~ 0.3 .

6.2.2 Clump SFR and stellar age

From Fig. 10, we see that the three species of clumps, SLCs, LLCs, and ex situ clumps, can be distinguished by their stellar ages. SLCs typically have stellar ages of ~ 50 – 100 Myr with a median age of ~ 85 Myr, and the very oldest have ages of ~ 150 Myr. LLCs have median stellar ages of ~ 240 Myr and the oldest have ages of up to ~ 1 Gyr, which is the median age of ex situ clumps, that can be up to ~ 3 Gyr old.

We have marked in the figure the median value of $\log(s)$ in bins of stellar age, for each of the three clump species. During their short lifetime, the SFR of SLCs does not vary systematically, and the median is $\sim 1\%$ with a scatter of $\sim \pm 0.5$ dex. The evolution of LLCs, on the other hand, is more well defined. The youngest clumps contribute $\lesssim 20\%$ to the disc SFR, and this value steadily decreases as $s \propto age^{-\alpha}$ with $\alpha \sim 1.5$, until it saturates at $\sim 2\%$ after ~ 100 Myr, slightly higher than SLCs. Ex situ clumps have a very broad range of SFRs that are not correlated with the disc.

In Fig. 11 we show clump sSFR normalized by the sSFR in the host disc for our clean sample, as a function of clump stellar age. SLCs form a cloud, with ages uniformly distributed between ~ 30 – 150 Myr and a tail down to 10 Myr. Their sSFR values are ~ 10 – 100 times greater than the disc, with a median ratio of 30 , independent of age. The youngest LLCs have comparable sSFR values, but these very quickly decline, scaling as $s\text{SFR} \propto age^{-\alpha}$ with $\alpha \sim 2$ in the age range

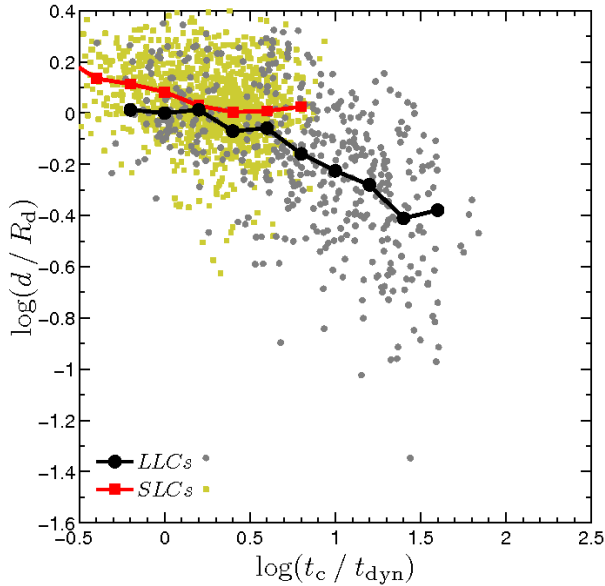


Figure 14. Clump migration. We show the clump galactocentric distance normalized by the disc radius as a function of the clump time normalized by the disc dynamical time. SLCs are typically at the disc edge, where most new clumps are formed, but can be found at distances as small as $\sim 0.5R_d$. LLCs clearly migrate closer to the disc centre as time goes by. After $\sim 30t_{\text{dyn}}$, at the end of migration, most LLCs are at $\sim 0.3R_d$ and the innermost clumps are at $\sim 0.1R_d$.

40 – 250 Myr, after which it saturates at only slightly higher values than the disc average. The ex situ clumps have comparable ages and sSFR ratios to the oldest in situ clumps.

It is important to realize that the stellar age of LLCs is typically younger than the true time that has elapsed since the formation of the clump. This is due to ongoing star-formation in the clump as well as stripping of old stars, as was pointed out by Bournaud et al. (2014). In Fig. 12 we show the stellar age as a function of clump time for the LLCs in our clean sample, together with the median age in bins of time. For the first ~ 150 Myr, the two agree by construction, since this is how we initialize the clump time when it is first identified. However, at later times, the stellar ages are ~ 0.2 dex below t_c . This makes the scaling of sSFR with time for LLCs slightly shallower than seen in Fig. 11.

6.2.3 Outflows from clumps

In Fig. 13 we show the mass loading factor, defined as $\eta = M_{\text{gas, out}}/\text{SFR}$, for the clumps in our clean sample as a function of clump mass, M_c . We computed the outflow rate of gas through thin spherical shells with width $\Delta r = 140$ pc centred at radii $r = R_c$, $1.5R_c$ and $2R_c$, only considering gas that is outflowing, $V_r > 0$, with velocity magnitude larger than the escape velocity from the clump at each shell, $V > V_{\text{esc}} = (2GM_c/r)^{1/2}$. Since the clump is not isolated but located within a dense disc, this is not the true escape velocity from the system, but it does give a rough approximation

for the outflows generated at the clump base. The value used in η is the average of the value obtained from the three shells, which have a typical scatter of ~ 0.1 dex between them. The mass loading factor decreases with mass, so that LLCs tend to have lower values than SLCs, though the scatter is very large. At masses $M_c \lesssim 10^{8.5}M_\odot$, the median mass loading factor is of order unity, $\eta \sim 1$, and values as high as $\eta \gtrsim 3$ are common. These clumps are the launching sites of galaxy-scale outflows, whose extent is correlated with the distribution of clumps (Ceverino et al. 2016b). The most massive clumps with $M_c \sim 10^9M_\odot$ have median values of $\eta \sim 0.3$, though values of $\eta \gtrsim 1$ are not uncommon. These may correspond to observations of very massive clumps with strong outflows (Genzel et al. 2011; Newman et al. 2012).

6.2.4 Clump migration and gradients of clump properties

Figure 14 examines the migration of in situ clumps, LLCs and SLCs, in our clean sample. We show the clump galactocentric distance normalized by the disc radius, d/R_d , as a function of the clump time normalized by the disc dynamical time, t_c/t_{dyn} . The dynamical time is defined as $t_{\text{dyn}} = R_{\text{rot}}/V_{\text{rot}}$, where R_{rot} and V_{rot} are the mass-weighted mean radius and rotational velocity of cold gas in a cylindrical ring 1 kpc thick in the vertical direction and extending from $0.5R_d$ to R_d in the radial direction⁹. We also show the median distance in bins of clump time. The median lifetime of a SLC is $\sim 2t_{\text{dyn}}$ and the oldest of them live for $\sim 4t_{\text{dyn}}$. They are mostly located at $d \simeq R_d$, though many of them can be found at $d \sim 0.5R_d$. There is no trend of distance with time, so any radial migration of SLCs during their lifetime is negligible. The youngest LLCs have a similar radial distribution to the SLCs, reflecting the star-forming ring where clumps are formed. After $\sim 4t_{\text{dyn}}$ there is clear radial migration, and the median distance scales as $d \propto t^{-\alpha}$ with $\alpha \sim 0.5$. We do not identify any LLCs older than $\sim 30t_{\text{dyn}} \sim 4 - 5t_{\text{orb}}$, comparable to the expected migration time, $t_{\text{mig}} \simeq \delta^{-2}t_{\text{dyn}}$ (Dekel, Sari & Ceverino 2009), where $\delta \sim 0.15$ in our simulations. At this time, LLCs are typically found at $\sim 0.3 - 0.4R_d$, but can be found as close to the centre as $\sim 0.1R_d$. We do not find any SLCs at such small distances, showing that clump formation is limited to the external disc, and the existence of clumps at such small radii is a clear sign of migration. This is a consequence of limiting our analysis to massive post-compactification discs. These have developed a central bulge and begun to stabilize in their centres, while VDI and clump formation is limited to a star-forming ring at radii $0.5 - 1 \times R_d$. At higher redshifts, in pre-compactification discs that lack a central mass concentration, our simulations do show

⁹ For a uniform disc, $R_{\text{rot}} \simeq 0.78R_d$. For an exponential disc where $R_d = 2R_{1/2}$, which is the radius that contains $\sim 85\%$ of the mass, $R_{\text{rot}} \simeq 0.71R_d$. Assuming a flat rotation curve, this means that the dynamical time used here is roughly 75% of the dynamical time at R_d , where most new clumps are formed.

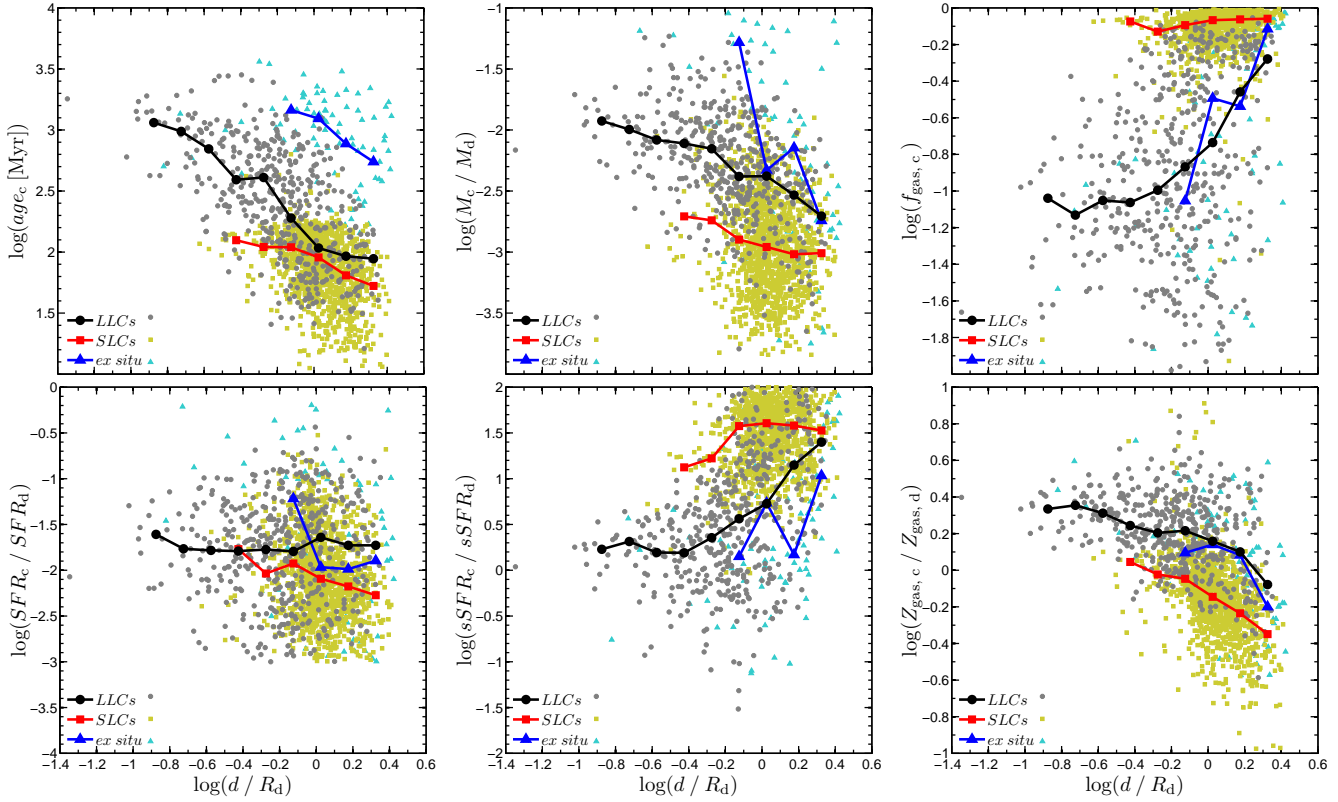


Figure 15. Gradients of clump properties with galactocentric distance. In each panel, the x axis is the distance from the galaxy centre normalized by the disc radius, d/R_d and the y axis refers to a different clump property. *Top left:* Mass-weighted mean stellar age; *top centre:* Baryonic clump mass normalized to the disc mass; *top right:* Gas fraction; *bottom left:* Clump SFR normalized to the disc SFR; *bottom centre:* Clump sSFR normalized to the disc sSFR; *bottom right:* Clump metallicity normalized to the mean disc metallicity. Lines and symbols are the same as in Fig. 10. The medians were calculated in equally spaced bins of 0.15 dex in $\log(d/R_d)$. There are hardly any SLCs within $\sim 0.5R_d$ while LLCs can be found at $\sim 0.1R_d$ at the end of migration. LLCs have a strong mass gradient, gaining a factor of $\sim 2 - 3$ in mass during migration, while SLCs show no such gradient. LLCs also exhibit a steep age gradient, where clumps closer to the disc centre have older stellar ages, while the corresponding gradient for SLCs is much shallower. SLCs have much higher gas fractions than LLCs which rapidly turn an order unity fraction of their mass into stars. While there is no strong trend of SFR with distance, the sSFR of LLCs steadily declines during migration while the SLCs have a roughly constant value. LLCs have a shallower metallicity gradient and higher metallicity values than SLCs. Ex situ clumps are much older, more massive and appear concentrated near the outer disc, though they are similar to LLCs in other properties.

clump formation at smaller radii. It is possible that these clumps may behave differently to the ones studied here, but as stated previously this is beyond the scope of the current analysis. Observations of clumpy unstable discs at $z \sim 2$ show similar unstable rings around stable centres (Genzel et al. 2014), and our predictions should be compared to such systems.

Figure 15 shows gradients of clump properties for all clumps in our clean sample. In each panel, the x axis shows the galactocentric distance normalized by the disc radius, $X \equiv d/R_d$, and the y axis shows different clump properties. We show points for individual clumps as well as the median value in equally spaced bins of distance. For each property discussed below, we quote the logarithmic slope of the radial dependence of the median values, i.e. α where $y \propto X^\alpha$.

Stellar Age: The top left panel shows stellar age. For SLCs, the clump time and age are by construction the same, so this can be easily compared with Fig. 14.

Exterior to $\sim 0.8R_d$, the median SLC ages have a slope of $\alpha \sim -0.6$, though the scatter about this relation is very large, and interior to $0.8R_d$ there is no radial trend. The LLC profile is steeper, the median ages exhibiting a slope of $\alpha \sim -1$, very similar to the slope found by M14 in simulations with weaker feedback. We conclude that an age gradient in the outer disc is not by itself evidence of clump migration, but migration causes a steeper age gradient which extends to smaller radii in the disc. Ex situ clumps have much older ages than in situ clumps, comparable to the mean stellar age of the disc, and show no systematic gradient. This is consistent with them being mergers, and consistent with the results of M14.

Mass: The top centre panel shows clump baryonic mass normalized by the disc mass. The mass range of SLCs is roughly 1 dex with a median at $\sim 0.1\%$ of the disc mass and no appreciable trend with distance, except for the innermost SLCs, which can in fact be identified for 2 snapshots. On the other hand, the LLCs grow in mass by ~ 0.7 dex during migration. In the

outer disc, $d > 0.5R_d$, the slope is $\alpha \sim -0.9$, while in the inner disc it flattens to $\alpha \sim -0.4$, very similar to the mass profile found by M14. Fitting a single slope from R_d to $0.1R_d$ results in $\alpha \sim -0.6$. LLCs grow in mass during migration by accreting gas from the disc (Dekel & Krumholz 2013, M14). While it has been suggested that a mass gradient could be present at birth, due to higher velocity dispersions closer to the disc centre leading to a larger Jeans mass (e.g. Genel et al. 2012), we find no evidence for this among our clean sample of SLCs (though see §B for how observationally selecting only the brightest clumps may introduce such a gradient). Ex situ clumps are more massive than in situ clumps at all radii, and they also exhibit a trend for more massive clumps to be located closer to the centre, as found by M14. This can be caused by mass growth of ex situ clumps that join the disc rotation and migrate in a similar manner to in situ clumps, or by more massive mergers sinking to the centre faster.

Gas fraction: The top right panel shows the gas fraction. SLCs have very high gas fractions. the median values decrease from near unity at the outer disc to $\sim 70\%$ for the innermost SLCs, with a flat slope of $\alpha \sim 0.10$. The 67% scatter about the median is $0.64 - 0.88$, so SLCs turn only $\lesssim 30\%$ of their mass into stars before being disrupted. Since the oldest SLCs are $\sim 10t_{\text{ff}}$, this translates to a time averaged SFR efficiency per free fall time of $\sim 3\%$. Even the most gas rich LLCs rarely have gas fractions greater than $\sim 65\%$, and their median profile shows a dramatic decline very early on. By the end of migration, LLCs have median gas fractions of $\sim 8\%$, almost a factor of 10 lower than at the disc outskirts, and the 67% scatter about the median is $\sim 4 - 24\%$. LLCs turn most of their mass into stars which is why they are able to remain bound. Ex situ clumps have similar gas fractions to LLCs.

SFR: The bottom left panel refers to the clump SFR normalized to the disc total. SLCs have a tendency for higher SFRs closer to the disc centre, with a slope of $\alpha \sim -0.65$, though the scatter is very large. The median SFR of LLCs is constant with distance at a value of $\sim 1 - 2\%$ of the disc total, though here too the scatter is large, ~ 1 dex. The constancy of the SFR during migration reflects a steady state between inflows from the disc and SF+outflows, and is consistent with Fig. 10.

sSFR: The bottom centre panel refers to sSFR, normalized to the disc mean, and can be compared to Fig. 11. SLCs have very high sSFRs of ~ 30 times the disc average, except for the innermost clumps which actually survive for two timesteps. The LLCs have comparable sSFR to the SLCs at birth, but this value steadily declines during migration, with a typical slope of $\alpha \sim 1.6$. Interior to $\sim 0.4R_d$, the sSFR saturates at roughly $1 - 2$ times the disc mean. The median sSFR for ex situ clumps is slightly lower than that of LLCs.

metallicity: The bottom right panel examines clump gas metallicity normalized by the mass weighted mean metallicity in the disc. The SLCs exhibit a slope of $\alpha \sim -0.6$ exterior to $0.8R_d$, saturating at the average

disc value at smaller radii. This is very similar to the metallicity gradient in the underlying disc, since the SLCs do not self-enrich much. In fact, SLCs at large radii acquire gas with very low metallicities from primordial gas inflow (Ceverino et al. 2016a). Averaged over the whole disc, the LLCs have a shallower gradient of $\alpha \sim -0.3$, similar to the gradient found by M14, though exterior to $0.8R_d$ their gradient appears similar to that of the SLCs. They have higher metallicity values than SLCs overall since they continually form stars and can self-enrich during their migration. Observations of gradients in clump metallicity that are shallower than the underlying disc may thus be evidence for clump migration. However, ex situ clumps have very similar behaviour to LLCs, with nearly identical distributions, presumably because ex situ clumps can join the disc rotation and migrate towards the disc centre while accreting fresh gas from the underlying disc, similar to migrating LLCs (M14).

To summarize, LLCs in our simulations exhibit very similar gradients to those predicted by M14 in most of their properties. SLCs can also show gradients in stellar age and gas fraction, though these are typically much shallower, while their metallicity gradient is steeper. SLCs do not show a gradient in mass (though see §B) or sSFR, contrary to LLCs. Furthermore, SLCs are not expected within $\sim 0.5R_d$ in post-compaction discs, while LLCs exist at distances $d \gtrsim 0.1R_d$ where they have higher masses, older ages, lower gas fractions and lower sSFRs. These can be used to observationally test the clump migration scenario. Ex situ clumps have comparable SFRs, gas fractions and metallicities to LLCs, but they are more massive and older, and are typically located at large distances similar to SLCs.

6.3 Clumpiness of Galaxies

An important observational constraint of cosmological models of VDI is the fraction of clumpy discs as a function of galaxy mass and redshift and the total contribution of clumps to the galaxy SFR and mass. We address this in Fig. 16. As in the previous section, we limit this analysis to the mass limited sample of star-forming clumps, i.e. clumps with $M_c > 10^7 M_\odot$ and $s = SFR_c/SFR_d > 10^{-3}$. In addition, we only account for clumps within a sphere of radius R_d . However, unlike the previous section, we do not limit the disc mass or redshift range. The ex situ clumps comprise only $\sim 4\%$ of the clumps in the sample, though they contribute $\sim 38\%$ of the mass and $\sim 22\%$ of the SFR.

The two left panels in Fig. 16 show the fraction of clumpy galaxies in our sample, f_{clumpy} , i.e. the fraction of galaxies that contain at least one clump obeying the above criteria. In the top panel we show this as a function of redshift in bins of stellar mass and on the bottom we show this as a function of stellar mass in bins of redshift. Stellar mass here refers to the total stellar mass within R_d . The error bars refer to the Poisson error within each bin. We caution, however, that while we have many snapshots, they are from a limited number of independent galaxies, especially below $z \sim 2$. Therefore,

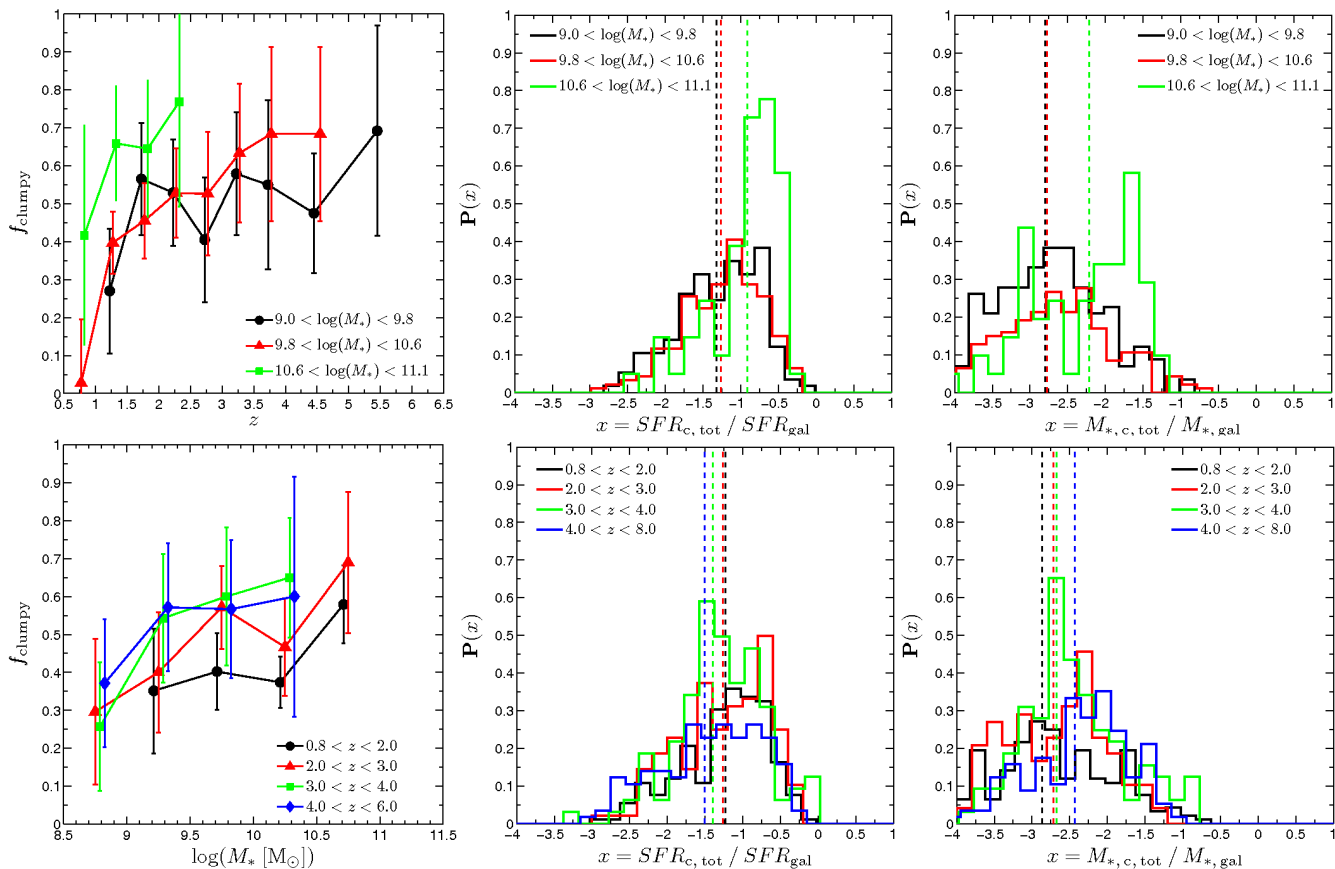


Figure 16. Clumpiness of simulated galaxies. We show various measures of the clump contribution to the galaxy population, using clumps within a sphere of radius R_d that have $M_c > 10^7 M_\odot$ and $SFR_c/SFR_d > 10^{-3}$. On the left we show the fraction of clumpy galaxies as a function of redshift in three bins of stellar mass (top) and as a function of stellar mass in four redshift bins (bottom). Galaxy stellar mass is computed within a sphere of radius R_d . The error bars are Poissonian, and we only show bins where we have data from at least 5 snapshots among at least 3 different simulations. The clumpy fraction is $\sim 40 - 60\%$ over a broad range of stellar masses and redshifts, though it tends to decrease towards low redshifts and low mass galaxies. The middle column shows the combined contribution of clumps to the SFR of clumpy galaxies (computed in the same sphere). We show the distributions in the same bins of galaxy mass (top) and redshift (bottom) used previously. Each histogram is normalized to an integral equal to the clumpy fraction in the bin. Vertical dashed lines show the median values of each bin, according to the color legend. The distributions are very similar at all redshifts, with median contributions of $\sim 3 - 6\%$ and a slight trend for higher values at lower redshifts. High mass galaxies have a higher contribution from clumps, $\sim 12\%$ compared to $\sim 6\%$ in lower mass galaxies. On the right we show distributions for the combined contribution of clumps to the stellar mass of clumpy galaxies, in the same bins used previously. Vertical dashed lines show the median values of each bin. The distributions are overall similar at all redshifts, but the median value declines towards lower redshift by ~ 0.4 dex from $4 < z$ to $z < 2$. Again, the contribution of clumps to the high mass galaxies is larger than the low mass galaxies, by roughly ~ 0.5 dex in the median, though the low end of the distribution is very similar.

the fraction of clumpy galaxies is a somewhat biased measure, because whether a particular galaxy is clumpy or not in a particular snapshot will influence the chances that it will be clumpy in the next snapshot. We try to mitigate this by only plotting bins where we have at least 5 snapshots from at least 3 independent galaxies. Nevertheless, the errors on f_{clumpy} may be larger than indicated by the error bar.

There is a tendency for galaxies to become less clumpy with time, though the fraction of clumpy galaxies among low mass galaxies is fairly constant at $\sim 50\%$ from $z \sim 1.5 - 4$. Intermediate mass galaxies have comparable clumpy fractions at $z \sim 1 - 3$, and slightly higher fractions at higher redshifts, though this is within the scatter. The clumpy fraction is higher

among massive galaxies, though this declines steeply from $z \sim 2.5 - 1$, and is also within the scatter. The clumpy fraction is also fairly constant at $f_{\text{clumpy}} \sim 40 - 60\%$ over a large range in stellar mass, with a tendency for the most massive galaxies to be clumpier than the least massive galaxies.

In the middle two panels, we examine the total contribution of clumps to the galaxy SFR, calculated within a sphere of radius R_d . We show the distributions for the same bins of stellar mass (top) and redshift (bottom) used in the f_{clumpy} measurements. Each histogram is normalized to an integral equal to the fraction of clumpy galaxies in the respective bin. The distribution is only weakly dependent on redshift. The median contribution of clumps to the total SFR grows

from $\sim 3 - 6\%$ between $4 < z$ and $z < 2$, while the FWHM of the distribution is $\lesssim 1$ dex at all redshifts. On the other hand, there is a tendency for the most massive galaxies to have a higher contribution to their SFR from clumps, $\gtrsim 12\%$ as opposed to $\sim 6\%$ for less massive galaxies. However, as before, the distributions are wide with a FWHM of ~ 1 dex.

In the right two panels we show the total contribution of clumps to the galaxy stellar mass, in the same mass and redshift bins as above. These are lower than the SFR contributions by $1 - 1.5$ orders of magnitude. The distributions are similar at all redshifts, though the median contribution increases towards higher redshift, from $\sim 0.15\%$ at $z < 2$ to $\sim 0.35\%$ at $4 < z$. The two low mass bins have a very similar distribution, as they did for the SFR contribution, while the highest mass bin is again skewed towards high values, with a median of $\sim 0.55\%$ compared to $\sim 0.2\%$.

7 DISCUSSION

7.1 Clump Survival vs Disruption

There are two extreme scenarios concerning the life and fate of high-redshift giant clumps formed by VDI. In one scenario, the clumps, despite undergoing outflows, remain intact and even grow by accretion as they migrate into the disc centre on an orbital timescale, $\sim 250 - 500$ Myr at $z \sim 2$. In the competing scenario, the clumps disrupt on a dynamical timescale, $\sim 50 - 100$ Myr at $z \sim 2$, well before they complete their migration. Most previous numerical studies of VDI and high- z clump formation have typically fallen into one of these two categories. In simulations that incorporated only supernova feedback (e.g. Bournaud, Elmegreen & Elmegreen 2007; Agertz, Teyssier & Moore 2009; Ceverino, Dekel & Bournaud 2010; Ceverino et al. 2012; Mandelker et al. 2014; Tamburello et al. 2015), all massive clumps were long lived and migrated towards the disc centre where they coalesced in the bulge. In simulations that incorporated strong momentum driven feedback, either using sub-grid models for galactic scale winds (Genel et al. 2012) or models for RP feedback with very high trapping factors (Hopkins et al. 2012; Oklopčić et al. 2016), all clumps were rapidly destroyed. The simulations used in this study fall into an intermediate category, where RP feedback is implemented but without the additional boost from photon trapping. Recent simulations of isolated galaxies by Bournaud et al. (2014) which employed only a moderate boost factor fall into a similar category. This offers a compromise between the two extreme scenarios, where low mass clumps with low surface densities are disrupted in only a few free fall times, while massive, dense clumps are long lived.

Theoretically, the effect of radiation pressure and the strength of photon trapping in different environments is unclear. Idealized radiation hydrodynamics (RHD) simulations

by Krumholz & Thompson (2012, 2013) showed that radiation trapping in clump-like environments is negligible because the wind destabilizes due to radiation Rayleigh-Taylor instability and radiation escapes through optically-thin holes in the wind. On the other hand, Davis et al. (2014) simulated a similar setup to Krumholz & Thompson (2013), but using a different method for closing the RHD equations. They found that in very dense regions with very large optical depths, the effective photon trapping may be a factor of a few higher than advocated by Krumholz & Thompson (2013). However, it is unclear if the physical conditions they studied are relevant for high- z clumps. Recently, Rosdahl et al. (2015) performed RHD simulations of isolated galaxies, using yet a third method for closing the RHD equations, and found that the net effect of RP is gentler and less effective than often assumed in subgrid models.

Several analytic studies have attempted to estimate the effect of feedback on clumps. Murray, Quataert & Thompson (2010) argued that momentum-driven radiative feedback could disrupt the clumps on a dynamical timescale, as it does in local giant molecular clouds. Then Krumholz & Dekel (2010) showed that such an explosive disruption is not expected to occur in the high-redshift giant clumps unless the SFR efficiency in a free-fall time is $\epsilon_{\text{ff}} \sim 0.1$, much larger than what is implied by the Kennicutt relation at $z = 0$. Such a deviation from the local Kennicutt law is inconsistent with observations (Tacconi et al. 2010, 2013; Freundlich et al. 2013). Dekel & Krumholz (2013) proposed instead that the observed outflows from high-redshift clumps (Genzel et al. 2011; Newman et al. 2012), with mass loading factors of order unity, are driven by steady momentum-driven outflows from stars over many tens of free-fall times. Their analysis was based on the findings of Krumholz & Thompson (2013) and assumed that each photon can contribute to the wind momentum only once, so the radiative force is limited to $\sim L/c$. When combining radiation, protostellar and main-sequence winds, and supernovae, Dekel & Krumholz (2013) estimated the total direct injection rate of momentum into the outflow to be $\sim 2.5L/c$. The adiabatic phase of supernovae and main-sequence winds can double this rate. They conclude that most clumps are expected to complete their migration prior to gas depletion.

Given the uncertainties in the theoretical analysis, it is worthwhile to simulate and compare different scenarios with varying feedback strengths and study the effect on clumps. In this respect, our simulations are extremely useful because they produce both SLCs and LLCs, and by studying the different properties of these two populations, we can observationally constrain the longevity of clumps in the real Universe. Detailed observations of clump properties such as age, mass, metallicity, gas fraction and SFR, their correlations with each other and their radial variation across the disc will be able test for the existence of long-lived migrating clumps, and thus place constraints on stellar feedback.

7.2 Comparison With Observations

Many of the results presented in this work can be directly compared to existing observations, and make predictions for upcoming observations. We review here some of the more recent observational studies targeting high- z SFGs and compare our results with theirs.

7.2.1 Clumpiness of galaxies

Using a mass complete sample of 649 massive ($M_* > 10^{10} M_\odot$) at $0.5 < z < 2.5$, Wuyts et al. (2012) estimated the overall fraction of clumpy discs, finding it to range from $\sim 40 - 75\%$ at redshifts $z = 1.5 - 2.5$ and $\sim 15 - 80\%$ at $z = 0.5 - 1.5$, depending on the band used to identify clumps, with redder bands being less clumpy than bluer bands, and stellar mass maps being the least clumpy. However, in this study clumps are not detected individually as in our work, but are rather defined as off-centre pixels with heightened surface density in stacked, pixelated images of the galaxy population. Observations of several thousand galaxies in the CANDELS/GOODS-S and UDS fields in the redshift range $0.5 - 3$, where clumps are detected both visually and using an automated algorithm similar in spirit to the one implemented in this work (Guo et al. 2015), reveal clumpy fractions of $\sim 40 - 60\%$ for galaxies in a similar mass and redshift range as studied in this work. They find that for low mass galaxies ($M_* < 10^{9.8}$), this fraction is constant in time from $z = 0.5 - 3$. Higher mass galaxies have comparable clumpy fractions at $z \gtrsim 2$, but these decline towards lower redshifts, reaching $20 - 40\%$ at $z \sim 0.5$. Shibuya et al. (2016) used HST to study ~ 17000 galaxies at $z = 0 - 8$ and found that the fraction of clumpy galaxies increases from $z = 8$ to $z = 1 - 3$ where it is $\sim 50 - 60\%$, and then declines at $z \lesssim 1$ down to $\lesssim 30 - 40\%$ by $z \sim 0.5$. Given the uncertainties in the observations and the simulations, the clumpy fractions predicted by our simulations (Fig. 16) are consistent with the data, though a larger sample of simulations covering a broader mass range is needed to place tighter constraints.

7.2.2 Clump Masses and SFRs

Wuyts et al. (2012, 2013) and Guo et al. (2015) have measured the contribution of clumps to the total SFR of SFGs, accounting for variations in dust extinction across the disc and between clump regions and off-clump regions. They find that in clumpy galaxies, the clumps contribute $\sim 5 - 15\%$ of the total SFR. Guo et al. (2015) find a slight tendency for higher contributions at lower redshifts, but no systematic dependence on galaxy mass. These results are in good agreement with our simulations (Fig. 16).

Wuyts et al. (2012) estimated a total contribution of clumps to the stellar mass of clumpy galaxies to be $\lesssim 5\%$, when observing in blue wavelengths. This is quite a bit higher than the mass fractions in our simulations. However, this study did not attempt to resolve individual clumps, but rather studied stacked,

pixelated images of galaxies, so a one-to-one comparison is difficult. Much of what we deem as off-clump material, as well as many of our ZLCs would likely be included in this mass estimate. We also note that we find a comparable contribution of clumps to the disc mass of clumpy galaxies, so the very low ratios of clump mass to total stellar mass may be influenced by our bulge to disc ratios being somewhat higher than observed galaxies, rather than by our clumps not being massive enough.

Guo et al. (2015) examined the UV luminosity functions of clumps as a function of galaxy mass and redshifts. Livermore et al. (2015) studied a sample of strongly lensed galaxies at $1 < z < 4$ and also measured the UV luminosity function of clumps, down to much smaller scales than available in other works, due to the magnification afforded by lensing. Their results are extremely similar to the shape of the SFR function for our simulated clumps. The rising slopes at the faint end, the declining slope at the bright end, and the increase of the high-end cutoff towards higher redshift are all very consistent with our results. A quantitative comparison requires detailed treatment of dust in the simulations, which is ongoing. However, the inescapable conclusion is that individual clumps contribute more to the galaxies UV light and SFR at higher redshifts. This is likely a result of the higher fragmentation scale at high redshifts due to the increased dust fractions (Livermore et al. 2015). On the other hand, lower redshift galaxies contain more clumps, each of which is less bright, but which combined can contribute more to the total galaxy light.

7.2.3 In Situ vs Ex Situ Clumps

As already pointed out by M14, we find that in situ clumps and merging ex situ clumps are distinguishable. In order to get a clean sample of in situ clumps with which to test the predictions presented here, separating the two populations is desirable. As advocated by M14, clumps near the disc edge that are massive, $\lesssim 0.1 M_d$, with old stellar populations ~ 1 Gyr old and low sSFRs of $\lesssim 0.1 \text{ Gyr}^{-1}$ are likely to be ex situ. While in situ clumps can develop comparable properties late in their life, this only occurs deep within the disc.

In many cases, young stellar ages and high sSFRs and gas fractions should translate to observed blue colors and vice versa. However, realistic luminosities and colors will depend on the effects of dust. In an ongoing work, dust and radiative transfer is incorporated into the simulated galaxies using the SUNRISE code (Jonsson 2006), thus creating realistic mock observations comparable to CANDELS data (Moody et al. 2014). Preliminary results show that in situ clumps are not affected much by dust near the disc edge in face-on images and they indeed tend to appear very blue, so the distinctions between in situ and ex situ discussed above should be observable. Similar conclusions were reached by Wuyts et al. (2013) who found dust extinction to be weaker in UV selected clumps than in the interclump regions. However, in edge on views and toward the central parts of the disc,

the in situ clumps are reddened, and the differences between the clump types become less pronounced. Observations find most off-centre clumps to be blue (Elmegreen & Elmegreen 2005; Förster Schreiber et al. 2011; Guo et al. 2012; Wuyts et al. 2012; Guo et al. 2015). Based on our analysis of the simulations and the preliminary SUNRISE images, this suggests that the majority of the observed off-centre clumps are, indeed, in situ.

A few of the observed off-centre clumps are redder and more massive (Genzel et al. 2011; Förster Schreiber et al. 2011), and these may well be ex situ clumps. It is also possible that more ex situ clumps have been observed, but classified as mergers rather than clumps. In addition, central massive red clumps have been observed (Elmegreen et al. 2009; Guo et al. 2012; Wuyts et al. 2012) which seem to resemble our bulge clumps.

Given the mounting theoretical and observational evidence that most of the high- z SFGs are extended discs undergoing VDI and that external mergers are responsible for only a part of the clump population, it would not make sense to classify the high- z SFGs using the familiar classification schemes used at low redshifts. In particular, the high- z VDI phase with giant clumps is unlikely and therefore unaccounted for at low redshift, where disc instability takes the form of a bar and spiral arms associated with secular evolution (though see Green et al. (2014) for a sample of low- z analogues to the high- z clumpy discs). This calls for a new classification scheme for high redshift galaxies, which recognizes the dominance of VDI systems and explicitly differentiates between VDI galaxies and merging systems. Such a scheme will be devised using the SUNRISE images of the simulated galaxies together with the complete merger history of all the clumps.

7.2.4 Clump Migration

The stellar ages of clumps and their predicted lifetimes are being estimated observationally, though with very large uncertainties. Elmegreen & Elmegreen (2005) observed ten clump-cluster galaxies in the HUDF at $1.6 < z < 3.0$ with 5-10 clumps each, and estimated clump ages of 100 – 800 Myr, with an average of 340 Myr, hosted in older discs of 1.4 – 3 Gyr. Then Elmegreen et al. (2009) found a very large range of ages for star-forming clumps, centred around 100 Myr but reaching values as high as 1 Gyr. Genzel et al. (2011), who examined five $z \sim 2.2$ clumpy SFGs with SINFONI, estimated clumps to be between 10 and a few hundred Myr old, with typical clumps having stellar ages of 100 – 200 Myr and an upper envelope of 300 Myr. Additional considerations led them to estimate the average lifetime of clumps to be ~ 500 Myr. Förster Schreiber et al. (2011) obtained ages for 7 clumps in one galaxy from the SINS survey, which ranged from a few tens to about ~ 250 Myr, centred on just below 100 Myr. Wuyts et al. (2012) pixelated and stacked galaxy images and defined clumps as off-centre pixels with elevated surface brightness

above the background. At $z \sim 2$, the clump pixels have ages of ~ 200 Myr, far younger than the off-clump pixels. At $z \sim 1$, both the clumps and the discs are older by about a factor of 2. Guo et al. (2012) collected data on ~ 40 clumps from ten galaxies in the HUDF and found the distribution of clump ages to be roughly lognormal, centred on ~ 300 Myr, but covering a wide range from 10 Myr to a few Gyr, while the disc ages were concentrated in the range 0.3 – 1 Gyr.

Zanella et al. (2015) observed a massive, $M_c \gtrsim 2.5 \times 10^9 M_\odot$, off centre clump at $z \sim 2$. They estimated its sSFR to be 30 times higher than the underlying disc, with a gas consumption timescale 10 times faster. They were also able to obtain robust age measurements, finding the stellar population to be ~ 10 Myr old and suggesting that the clump is in the process of formation. Using this short time window for their discovery, together with the fact that they found one such case in a sample of 68 galaxies, they estimated the frequency of formation of such a massive clump to be $\sim 2.5 \text{ Gyr}^{-1}$ per galaxy. Given the observations of 1 – 2 clumps per galaxy with similar masses, they estimated a clump lifetime of ~ 500 Myr.

These studies use different methods for estimating the clump stellar ages, and all agree that their uncertainties are very large. Nevertheless, the fact that the clumps exhibit such a wide range of ages in any particular study and that even low estimates on clump ages are rarely far below 100 Myr seem to favour a scenario where clumps are long lived. This is especially true when one considers that the observed stellar ages of clumps are likely underestimates of the true time since clump formation, due to continued star formation in the clump and tidal stripping of the older stars (Fig. 12 and Bournaud et al. 2014).

Some of these studies (Förster Schreiber et al. 2011; Guo et al. 2012) have even attempted to measure radial variations of clump properties within the discs. They find evidence for older, redder and more massive clumps to be located closer to the disc centre. Förster Schreiber et al. (2011) find a logarithmic slope for the ages of seven clumps in a single galaxy of -2.06 ± 0.63 , much steeper than the radial variation of the background disc. They note that even if the absolute values for clump ages are wrong, the relative trend should hold. In another galaxy from their sample, also containing seven clumps, they found clumps to become redder closer to the centre, with increased mass-to-light ratios. Clumps near the disc edge have masses of $\sim 10^8 M_\odot$ while close to the centre the masses are $\gtrsim 6 \times 10^8 M_\odot$. Guo et al. (2012) find that clumps closer to the disc centre have lower sSFRs, older ages, higher dust extinctions and higher stellar surface densities. Moreover, they find the radial variation in clump properties steeper than the global gradients in the background disc, and deduce that the clumps must have evolved separately from the disc in a state of quasi-equilibrium. They find clumps within 0.1 times the disc radius to have sSFR values 5 times lower and stellar surface densities 25 times higher than clumps in the outer half of the disc, very similar to the LLCs

produced in our simulations. The clumps near the disc centre have ages of roughly 700 Myr as opposed to ~ 100 Myr in the outer disc. These studies, while crude and preliminary, are in good agreement with the predictions of clump migration, which seems to indicate that massive clumps survive for extended periods longer than an orbital time and evolve as they migrate inwards.

7.3 Caveats and Future Prospects

As detailed in §2.3, these simulations are still not doing the best job in terms of feedback and star-formation. The same simulations studied in this work in the NoRP and RP versions are currently being run in a third version which includes additional radiation trapping, with an effective boost factor of a few in dense regions, as well as photoheating from UV photons (Ceverino et al. 2014). These simulations will be analyzed in a similar way to the NoRP and RP versions used here to determine the effect on clump survival. However, preliminary tests reveal that this new feedback has only a minor effect on the stellar masses of the galaxies. Furthermore, Ceverino et al. (2014) showed that the effect of these additional feedback mechanisms on the density and temperature of ISM is less severe than the initial effect of RP as implemented here. Therefore, we do not expect the main conclusions of this work to change, namely that massive clumps will survive and migrate towards the centre.

However, the weak feedback may underestimate the importance of winds in LLCs. In work in preparation, we use an analytic bathtub toy model to predict the evolution of giant clumps subject to feedback driven winds, star formation and mass accretion from the surrounding disc. We find that for realistic mass loading factors, the clump mass should be constant during migration, with accretion balancing the outflows. However, in these simulations we find a strong mass gradient for LLCs, similar to the very weak feedback simulations studied in M14. This may affect the properties of LLCs, and must be tested in future studies of simulations with more realistic feedback.

Finally, our analysis has been performed in 3D, taking full advantage of the information available in the simulations. While this method has helped us develop a theoretical understanding of VDI, one should now worry about how to directly compare our results with realistic 2D observations that also suffer from dust effects, background and foreground contamination, and beam smearing. Previous studies (Moody et al. 2014; Snyder et al. 2015) have used the radiative transfer code SUNRISE to “observe” these simulated galaxies in a realistic way, e.g. for comparison with CANDELS data. Efforts are currently being made to use these mock-observations to compare the populations of clumps found in this work to observed clumps found using the method of Guo et al. (2015). This will greatly assist in relating the simulations to observations, and devising observational tests to distinguish between LLCs and SLCs, as well as between in situ clumps and mergers, allowing us to devise a

new theory-motivated classification scheme for high- z galaxies, which explicitly accounts for VDI.

8 CONCLUSIONS

We have studied the lifetime, evolution and properties of giant clumps formed in high- z disc galaxies using two suites of high-resolution cosmological simulations, run with and without radiative-pressure feedback from young stars. Our main goals were to address the effect of radiation pressure on the formation and survival of clumps, and to devise observable signatures of clump evolution during their inward migration. While the RP feedback used here is relatively weak compared to what is often assumed in other works, our predictions regarding observable differences between long-lived, migrating clumps and short-lived disrupting clumps, when combined with observations, can be used to place constraints on clump migration and the efficiency of feedback. Our main results can be summarized as follows:

(i) RP feedback lowers the galactic stellar mass by a factor of ~ 2 at $z \sim 2$ and by up to a factor of ~ 10 in low mass galaxies at high redshift. While our stellar-to-halo mass ratios are still roughly a factor of ~ 2 above the Behroozi, Wechsler & Conroy (2013) relation, they appear consistent with recent observations of SFGs at $z \lesssim 2$ residing in halos of mass $M_v \lesssim 4 \times 10^{11} M_\odot$ (Burkert et al. 2015, figure 5).

(ii) RP has only a mild effect on the sizes of discs, increasing the thickness by $\sim 30\%$ and the radius by $\lesssim 10\%$. The cold fraction within the disc radius increases when RP is included due to delayed star-formation and increased gas fractions. However, the Toomre Q parameter is comparable in both feedback models, showing that one is not inherently more unstable than the other. In both feedback models, the ISM density transitions from a log-normal distribution, dominated by supersonic turbulence at low densities to a power law distribution, dominated by self-gravity, at high densities of $n \gtrsim 10 \text{ cm}^{-3}$. In the RP simulations, the fraction of mass in dense self-gravitating gas is reduced by a factor of ~ 2 .

(iii) There is a bi-modality between short-lived clumps (SLCs) and long-lived clumps (LLCs), separated at a lifetime of ~ 20 free-fall times. While RP only mildly suppresses the total number of clumps that form, it greatly reduces the number of LLCs. There is also a large population of low-mass clumps with virial parameters $\alpha_v \sim 10-1000$ that never formed significant stellar populations in them (zero-lifetime clumps, ZLCs). These were likely never bound structures and are not included in our analysis.

(iv) The majority of clumps have densities $n_c > 10 \text{ cm}^{-3}$, in the self-gravitating regime of the ISM density distribution, and circular velocities $V_{\text{circ},c} > 20 \text{ km s}^{-1}$. Below this value, clumps are rapidly disrupted by supernova feedback even without RP. The

clump mass function flattens when these two thresholds meet, below $M_c \sim 10^{7.3} M_\odot$.

(v) When RP is included, it introduces a scale in surface density, with most clumps having surface densities $\Sigma_c > 200 - 300 M_\odot \text{pc}^{-2}$. This threshold meets the threshold in clump density of $n_c > 10 \text{cm}^{-3}$ at a mass of $M_c \sim 10^{8.2-8.5} M_\odot$. Above this mass, RP does not disrupt clumps and there are comparable numbers of LLCs in both simulation suites.

(vi) In addition to in situ clumps, formed by VDI, we identify ex situ mergers as part of the off centre clump population. RP greatly reduces the relative number of ex situ clumps, likely by reducing their central density prior to merging with the main galaxy and making them more susceptible to tidal disruption and stripping. Ex situ clumps tend to be more massive than in situ clumps. Among off-centre clumps in the RP simulations with $M_c > 10^7 M_\odot$, ex situ clumps are $\sim 5\%$ in number, $\sim 37\%$ in mass and $\sim 29\%$ in SFR.

(vii) The distribution of clump masses and SFRs normalized to their host disc is very similar at all redshifts. They exhibit a power-law at the bright end, with a slope slightly shallower than -2 and a cutoff at high masses and SFRs. The cutoff is at a higher mass at higher redshifts, so individual clumps become less dominant dynamically as time goes on. The shape of these distributions, including their slopes and the trend of cutoff value with redshift, are similar to observed luminosity functions of high- z clumps (Guo et al. 2015).

(viii) The fraction of clumpy galaxies is $\sim 40 - 60\%$ over a broad range of redshift and stellar mass, with a tendency to decrease towards lower redshift and for low mass galaxies. The general trends and percentages are similar to observations, within the uncertainties. Among clumpy galaxies, clumps contribute $\sim 3 - 30\%$ to the total SFR, and $\sim 0.1 - 3\%$ to the total stellar mass, though the contribution for massive galaxies can be higher. There is only a very weak dependence of these fractions with redshift, where clumps contribute a larger fraction of the stellar mass and a smaller fraction of the SFR at higher redshift.

(ix) Long-lived-clumps tend to migrate towards the disc centre over a migration time of $\sim 10 - 30$ disc dynamical times, and can be found at distances as small as $\sim 0.1 R_d$. SLCs are mostly located near the disc edge, and this is predicted to be the case in post-compactification discs. The two populations are well separated in the plane of age-sSFR, where LLCs are older and with lower sSFR values. LLCs exhibit radial gradients in age, mass, sSFR, gas fraction and metallicity, becoming older, more massive and metal-enriched but with lower gas fraction and sSFR closer to the disc centre. The SLCs show flatter gradients in age and gas fraction, steeper gradients in metallicity, and no significant gradient in mass or sSFR. Ex situ clumps tend to have older stellar ages and higher masses than the in situ clumps, especially near the disc edge. However, their gas fraction, metallicity and sSFR values are similar to the LLCs. These differences are in principle observable, and can be used to distinguish long-lived migrating clumps from short-lived, rapidly disrupting clumps and ex situ

mergers, and can place strong constraints on the origin and fate of observed giant clumps at high- z .

ACKNOWLEDGMENTS

We thank the anonymous referee for comments that have greatly improved this manuscript. The simulations were performed at the National Energy Research Scientific Computing centre (NERSC), Lawrence Berkeley National Laboratory, and at NASA Advanced Supercomputing (NAS) at NASA Ames Research centre. The analysis was performed on the Astric cluster at HU. This work was supported by ISF grant 24/12, by BSF grant 2014-273, by GIF grant G-1052-104.7/2009, by the I-CORE Program of the PBC, ISF grant 1829/12, by CANDELS grant HST-GO-12060.12-A, and by NSF grants AST-1010033 and AST-1405962. DC has been partly funded by the ERC Advanced Grant, STARLIGHT: Formation of the First Stars (project number 339177).

REFERENCES

- Agertz O., Teyssier R., Moore B., 2009, MNRAS, 397, L64
 Aubert D., Pichon C., Colombi S., 2004, MNRAS, 352, 376
 Behrendt M., Burkert A., Schartmann M., 2015, MNRAS, 448, 1007
 Behroozi P. S., Conroy C., Wechsler R. H., 2010, ApJ, 717, 379
 Behroozi P. S., Wechsler R. H., Conroy C., 2013, ApJ, 770, 57
 Birnboim Y., Dekel A., 2003, MNRAS, 345, 349
 Bond J. R., Cole S., Efstathiou G., Kaiser N., 1991, ApJ, 379, 440
 Bournaud F., Dekel A., Teyssier R., Cacciato M., Daddi E., Juneau S., Shankar F., 2011, ApJ, 741, L33
 Bournaud F., Elmegreen B. G., 2009, ApJ, 694, L158
 Bournaud F., Elmegreen B. G., Elmegreen D. M., 2007, ApJ, 670, 237
 Bournaud F. et al., 2012, ApJ, 757, 81
 Bournaud F. et al., 2014, ApJ, 780, 57
 Bryan G. L., Norman M. L., 1998, ApJ, 495, 80
 Burkert A. et al., 2015, ArXiv e-prints
 Cacciato M., Dekel A., Genel S., 2012, MNRAS, 421, 818
 Ceverino D., Arribas S., Colina L., Rodríguez Del Pino B., Dekel A., Primack J., 2016a, MNRAS, 460, 2731
 Ceverino D., Dekel A., Bournaud F., 2010, MNRAS, 404, 2151
 Ceverino D., Dekel A., Mandelker N., Bournaud F., Burkert A., Genzel R., Primack J., 2012, MNRAS, 420, 3490
 Ceverino D., Dekel A., Tweed D., Primack J., 2015, MNRAS, 447, 3291
 Ceverino D., Klypin A., 2009, ApJ, 695, 292
 Ceverino D., Klypin A., Klimek E. S., Trujillo-Gomez S., Churchill C. W., Primack J., Dekel A., 2014, MNRAS, 442, 1545

- Ceverino D., Primack J., Dekel A., 2015, *MNRAS*, 453, 408
- Ceverino D., Sánchez Almeida J., Muñoz Tuñón C., Dekel A., Elmegreen B. G., Elmegreen D. M., Primack J., 2016b, *MNRAS*, 457, 2605
- Chabrier G., 2003, *PASP*, 115, 763
- Conroy C., Wechsler R. H., 2009, *ApJ*, 696, 620
- Cresci G., Hicks E. K. S., Genzel R., Schreiber N. M. F., Davies R., Bouché N., Buschkamp P., et al., 2009, *ApJ*, 697, 115
- Daddi E. et al., 2010, *ApJ*, 713, 686
- Davis S. W., Jiang Y.-F., Stone J. M., Murray N., 2014, *ApJ*, 796, 107
- Dekel A., Birnboim Y., 2006, *MNRAS*, 368, 2
- Dekel A. et al., 2009, *Nature*, 457, 451
- Dekel A., Burkert A., 2014, *MNRAS*, 438, 1870
- Dekel A., Krumholz M. R., 2013, *MNRAS*, 432, 455
- Dekel A., Sari R., Ceverino D., 2009, *ApJ*, 703, 785
- Dekel A., Silk J., 1986, *ApJ*, 303, 39
- Elmegreen B. G., 2011, *ApJ*, 731, 61
- Elmegreen B. G., Bournaud F., Elmegreen D. M., 2008, *ApJ*, 688, 67
- Elmegreen B. G., Elmegreen D. M., 2005, *ApJ*, 627, 632
- Elmegreen B. G., Elmegreen D. M., Fernandez M. X., Lemonias J. J., 2009, *ApJ*, 692, 12
- Elmegreen D. M., Elmegreen B. G., Ravindranath S., Coe D. A., 2007, *ApJ*, 658, 763
- Federrath C., Klessen R. S., Schmidt W., 2008, *ApJ*, 688, L79
- Ferland G. J., Korista K. T., Verner D. A., Ferguson J. W., Kingdon J. B., Verner E. M., 1998, *PASP*, 110, 761
- Forbes J., Krumholz M., Burkert A., 2012, *ApJ*, 754, 48
- Forbes J. C., Krumholz M. R., Burkert A., Dekel A., 2014, *MNRAS*, 438, 1552
- Förster Schreiber N. M., Genzel R., Bouché N., Cresci G., Davies R., Buschkamp P., Shapiro K., et al., 2009, *ApJ*, 706, 1364
- Förster Schreiber N. M., Genzel R., Lehnert M. D., Bouché N., Verma A., Erb D. K., Shapley A. E., et al., 2006, *ApJ*, 645, 1062
- Förster Schreiber N. M. et al., 2011, *ApJ*, 739, 45
- Freundlich J. et al., 2013, *A&A*, 553, A130
- Gammie C. F., 2001, *ApJ*, 553, 174
- Genel S. et al., 2012, *ApJ*, 745, 11
- Genzel R., Burkert A., Bouché N., Cresci G., Förster Schreiber N. M., Shapley A., Shapiro K., et al., 2008, *ApJ*, 687, 59
- Genzel R. et al., 2014, *ApJ*, 785, 75
- Genzel R., Tacconi L. J., Eisenhauer F., Förster Schreiber N. M., Cimatti A., Daddi E., Bouché N., et al., 2006, *Nature*, 442, 786
- Genzel R. et al., 2015, *ApJ*, 800, 20
- Genzel R., et al., 2011, *ApJ*, 733, 101
- Green A. W. et al., 2014, *MNRAS*, 437, 1070
- Grogin N. A. et al., 2011, *ApJS*, 197, 35
- Guo Y. et al., 2015, *ApJ*, 800, 39
- Guo Y., Giavalisco M., Ferguson H. C., Cassata P., Koekemoer A. M., 2012, *ApJ*, 757, 120
- Haardt F., Madau P., 1996, *ApJ*, 461, 20
- Hopkins A. M., Beacom J. F., 2006, *ApJ*, 651, 142
- Hopkins P. F., 2013, *MNRAS*, 430, 1653
- Hopkins P. F., Kereš D., Murray N., Quataert E., Hernquist L., 2012, *MNRAS*, 427, 968
- Hopkins P. F., Quataert E., Murray N., 2011, *MNRAS*, 417, 950
- Hopkins P. F., Quataert E., Murray N., 2012, *MNRAS*, 421, 3488
- Immeli A., Samland M., Gerhard O., Westera P., 2004a, *A&A*, 413, 547
- Immeli A., Samland M., Westera P., Gerhard O., 2004b, *ApJ*, 611, 20
- Inoue S., Dekel A., Mandelker N., Ceverino D., Bournaud F., Primack J., 2016, *MNRAS*, 456, 2052
- Jonsson P., 2006, *MNRAS*, 372, 2
- Kennicutt, Jr. R. C., 1998, *ApJ*, 498, 541
- Kereš D., Katz N., Weinberg D. H., Davé R., 2005, *MNRAS*, 363, 2
- Koekemoer A. M. et al., 2011, *ApJS*, 197, 36
- Komatsu E. et al., 2009, *ApJS*, 180, 330
- Kravtsov A. V., 2003, *ApJ*, 590, L1
- Kravtsov A. V., Klypin A. A., Khokhlov A. M., 1997, *ApJS*, 111, 73
- Krumholz M., Burkert A., 2010, *ApJ*, 724, 895
- Krumholz M. R., Dekel A., 2010, *MNRAS*, 406, 112
- Krumholz M. R., Dekel A., 2012, *ApJ*, 753, 16
- Krumholz M. R., Thompson T. A., 2012, *ApJ*, 760, 155
- Krumholz M. R., Thompson T. A., 2013, *MNRAS*, 434, 2329
- Leitherer C. et al., 1999, *ApJS*, 123, 3
- Livermore R. C. et al., 2015, *MNRAS*, 450, 1812
- Madau P., Dickinson M., 2014, *ARA&A*, 52, 415
- Madau P., Pozzetti L., Dickinson M., 1998, *ApJ*, 498, 106
- Mandelker N., Dekel A., Ceverino D., Tweed D., Moody C. E., Primack J., 2014, *MNRAS*, 443, 3675
- Moody C. E., Guo Y., Mandelker N., Ceverino D., Mozena M., Koo D. C., Dekel A., Primack J., 2014, *MNRAS*, 444, 1389
- Moster B. P., Naab T., White S. D. M., 2013, *MNRAS*, 428, 3121
- Moster B. P., Somerville R. S., Maulbetsch C., van den Bosch F. C., Macciò A. V., Naab T., Oser L., 2010, *ApJ*, 710, 903
- Murray N., Quataert E., Thompson T. A., 2010, *ApJ*, 709, 191
- Newman S. F. et al., 2012, *ApJ*, 752, 111
- Noguchi M., 1999, *ApJ*, 514, 77
- Ocvirk P., Pichon C., Teyssier R., 2008, *MNRAS*, 390, 1326
- Oklopčić A., Hopkins P. F., Feldmann R., Keres D., Faucher-Giguere C.-A., Murray N., 2016, *ArXiv e-prints*
- Padoan P., Nordlund A., Jones B. J. T., 1997, *MNRAS*, 288, 145
- Press W. H., Schechter P., 1974, *ApJ*, 187, 425
- Price D. J., Federrath C., Brunt C. M., 2011, *ApJ*, 727, L21
- Rosdahl J., Schaye J., Teyssier R., Agertz O., 2015, *MNRAS*, 451, 34
- Rosolowsky E., 2005, *PASP*, 117, 1403

- Saintonge A. et al., 2011, MNRAS, 415, 32
 Scalo J., Vázquez-Semadeni E., Chappell D., Passot T., 1998, ApJ, 504, 835
 Shapiro K. L., Genzel R., Förster Schreiber N. M., 2010, MNRAS, 403, L36
 Shapiro K. L. et al., 2008, ApJ, 682, 231
 Shibuya T., Ouchi M., Kubo M., Harikane Y., 2016, ApJ, 821, 72
 Snyder G. F., Lotz J., Moody C., Peth M., Freeman P., Ceverino D., Primack J., Dekel A., 2015, MNRAS, 451, 4290
 Stark D. P., Swinbank A. M., Ellis R. S., Dye S., Smail I. R., Richard J., 2008, Nature, 455, 775
 Tacchella S., Dekel A., Carollo C. M., Ceverino D., DeGraf C., Lapiner S., Mandelker N., Primack J. R., 2016a, MNRAS, 458, 242
 Tacchella S., Dekel A., Carollo C. M., Ceverino D., DeGraf C., Lapiner S., Mandelker N., Primack Joel R., 2016b, MNRAS, 457, 2790
 Tacconi L. J., Genzel R., Neri R., Cox P., Cooper M. C., Shapiro K., Bolatto A., et al., 2010, Nature, 463, 781
 Tacconi L. J. et al., 2013, ApJ, 768, 74
 Tamburello V., Mayer L., Shen S., Wadsley J., 2015, MNRAS, 453, 2490
 Tomassetti M. et al., 2016, MNRAS, 458, 4477
 Toomre A., 1964, ApJ, 139, 1217
 Tweed D., Devriendt J., Blaizot J., Colombi S., Slyz A., 2009, A&A, 506, 647
 Vazquez-Semadeni E., 1994, ApJ, 423, 681
 Vázquez-Semadeni E., González R. F., Ballesteros-Paredes J., Gazol A., Kim J., 2008, MNRAS, 390, 769
 Williams J. P., McKee C. F., 1997, ApJ, 476, 166
 Wisnioski E. et al., 2015, ApJ, 799, 209
 Wuyts S. et al., 2012, ApJ, 753, 114
 Wuyts S. et al., 2013, ApJ, 779, 135
 Zanella A. et al., 2015, Nature, 521, 54
 Zolotov A. et al., 2015, MNRAS, 450, 2327

APPENDIX A: PARAMETER DEPENDENCE

The three main parameters in the clump finding algorithm are the resolution of the uniform grid, $\Delta = 70$ pc, the width of the Gaussian used to smooth the density field, $F_W = \min(2.5 \text{ kpc}, 0.5R_d)$, and the residual threshold to assign a cell to a clump $\delta_\rho^{\text{min}} = 10$. In Mandelker et al. (2014) we used a similar algorithm with $F_W = 2 \text{ kpc}$, $\delta_\rho^{\text{min}} = 15$ and $\Delta = 70$ pc, together with an additional narrow Gaussian having a FWHM of $F_N = 140$ pc, the residual defined as $\delta_\rho = (\rho_N - \rho_W)/\rho_W$. We find both the narrow smoothing and Δ to have no noticeable effect on any but the smallest clumps.

We examine the sensitivity of our clump finder to variations in F_W and δ_ρ^{min} using one of our clumpiest RP simulations, V13, shown face on at redshift $z = 1.5$ in Fig. 1. We experimented with values of $F_W = 2.0, 2.5 \text{ kpc}$ and $\delta_\rho^{\text{min}} = 5, 10, 15$. Since using $\delta_\rho^{\text{min}} = 5$ results in many small, low-mass, low-density clumps, and in any case we are only concerned with the effect

on larger clumps, we only considered for the purposes of this test clumps with at least 27 uni-grid cells, rather than the fiducial value of 8 used throughout the paper. We examined all in situ clumps found in this way in the redshift range $1.3 \lesssim z \lesssim 5$.

Figure A1 shows the distribution of clumps in the mass-size plane, for each of the six combinations of F_W and δ_ρ^{min} examined. The color represents the median value within each pixel of the clump shape, S_c , the red lines represent constant baryonic density, ranging from $n_c = 0.01 - 1000 \text{ cm}^{-3}$ in factors of 10, and the contour in each panel represents the number density of clumps per pixel, enclosing 50% of the total clump population. In each panel we list the parameters used and the total number of in situ clumps (including ZLCs).

Focusing on the bottom two rows, we see that increasing F_W from 2.0 to 2.5 kpc, or decreasing δ_ρ^{min} from 15 to 10, makes clumps larger and less dense as more background material is added to the clump. It also adds many low-mass, low-density clumps to the sample. However, in all cases, we learn from the contour that the bulk of the clump population follows a sequence of roughly constant density, $n_c \sim 1 - 10 \text{ cm}^{-3}$, and has prolate shapes with $S_c \lesssim 0.35$. In addition, we see a well defined population of dense, $n_c \sim 10 - 1000 \text{ cm}^{-3}$, and oblate, $S_c \gtrsim 0.6$ clumps, with radii $R_c \sim 300 - 400$ pc and masses $M_c \gtrsim 10^8 M_\odot$. These are the long-lived clumps, that have undergone gravitational collapse and remain bound. While raising F_W or lowering δ_ρ^{min} makes these clumps more extended, they remain well separated from the bulk of the population and their mass does not vary by much.

Using $\delta_\rho^{\text{min}} = 5$ reduces the median clump density to below 1 cm^{-3} and makes even the densest clumps much larger, significantly lowering their density. With such a low value for the residual threshold, most of these clumps become embedded in extended features of the ISM which are not bound. This blurs the distinction between the populations, and appears to be too low a value. This is to be expected, since most of the ISM volume is at densities $n < 1 \text{ cm}^{-3}$, but gas only becomes self gravitating at densities $n > 10 \text{ cm}^{-3}$ (Fig. 5).

In Fig. A2 we examine the mass functions for these 6 parameter combinations. The massive end, $M_c \gtrsim 10^8 M_\odot$, is virtually unaffected by increasing F_W from 2.0 to 2.5 kpc, and the effect on the low-mass end is less than a factor of ~ 1.5 in normalization, while the slope remains the same. Massive, oblate, bound clumps are unaffected by changing δ_ρ^{min} in the ranges 10 – 15. However, for $\delta_\rho^{\text{min}} = 5$ massive, compact clumps become embedded in extended, low density features that are not bound to the clump. This results in many more high mass, low-density clumps, which increase both the slope and the normalization of the mass function.

APPENDIX B: SELECTION EFFECTS

Many observational studies of clumps (e.g. Guo et al. 2012, 2015; Wuyts et al. 2012, 2013; Shibuya et al.

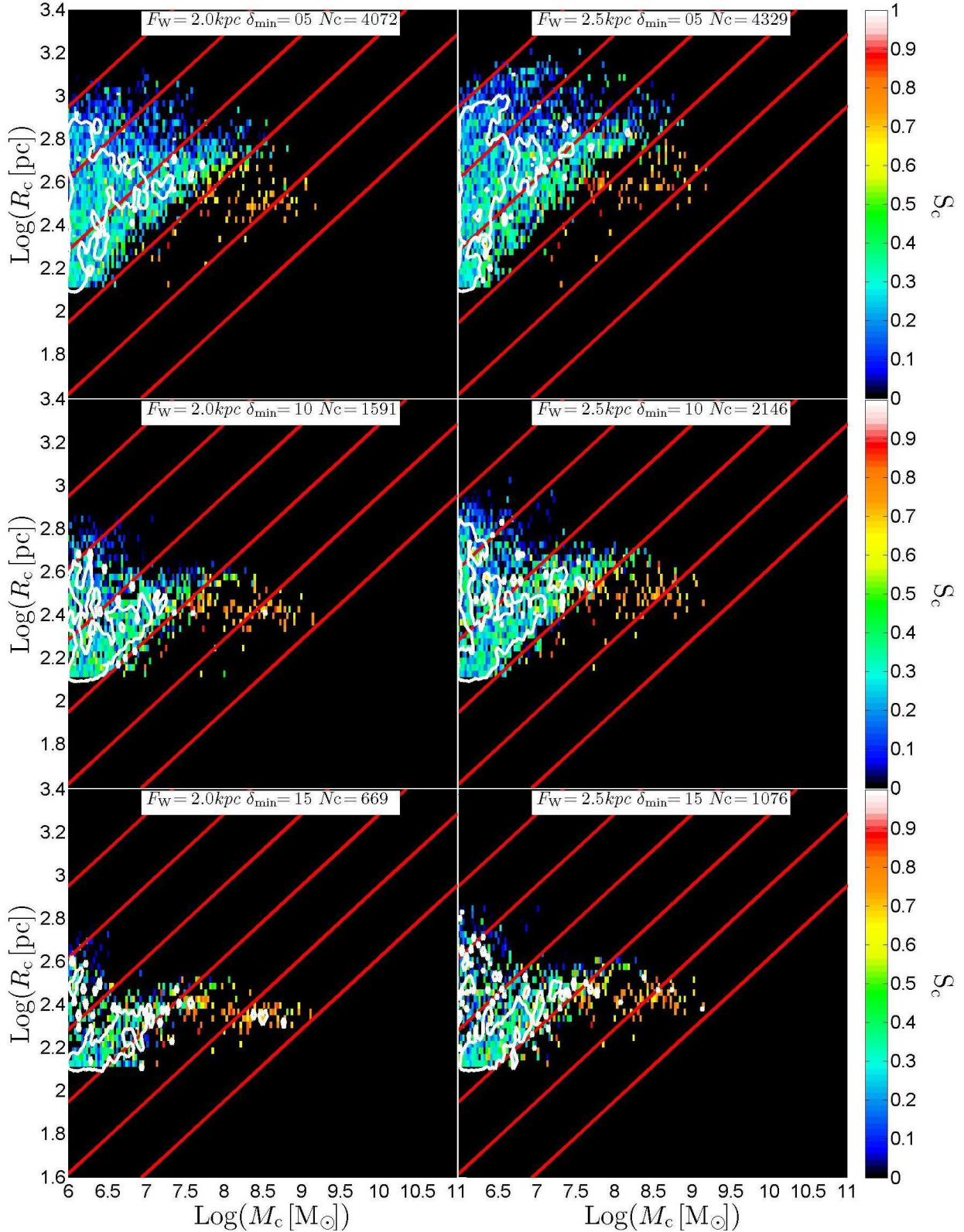


Figure A1. Dependence of clump masses, sizes and shapes, on the parameters of the clump finder. We show the distribution of in situ clumps identified in the RP version of V13 at $1.3 \lesssim z \lesssim 5$, in the mass-radius plane. The color is the median clump shape, S_c , per pixel. The white contours enclose the densest pixels in terms of number of clumps per pixel, that contain 50% of the clumps. The red lines are lines of constant density, $\log(n_c \cdot \text{cm}^{-3}) = -2, -1, 0, 1, 2, 3$ from top to bottom. The different panels are for different combinations of the parameters F_W and δ_ρ^{min} , as written at the top of each panel. The left (right) column refers to $F_W = 2.0 \text{ kpc}$ (2.5 kpc) while from top to bottom we have $\delta_\rho^{\text{min}} = 5, 10, 15$. Each panel also lists the total number of identified clumps. Lowering δ_ρ^{min} or raising F_W makes clumps larger and less dense by adding additional background material to the clumps, and it increases the number of low-mass, low-density clumps. As long as $\delta_\rho^{\text{min}} \gtrsim 10$, the population of massive, dense, bound clumps is not terribly sensitive to changes in the parameters. However, $\delta_\rho^{\text{min}} = 5$ embeds these clumps in large background features, making them appear much larger and less separated from the bulk of the population.

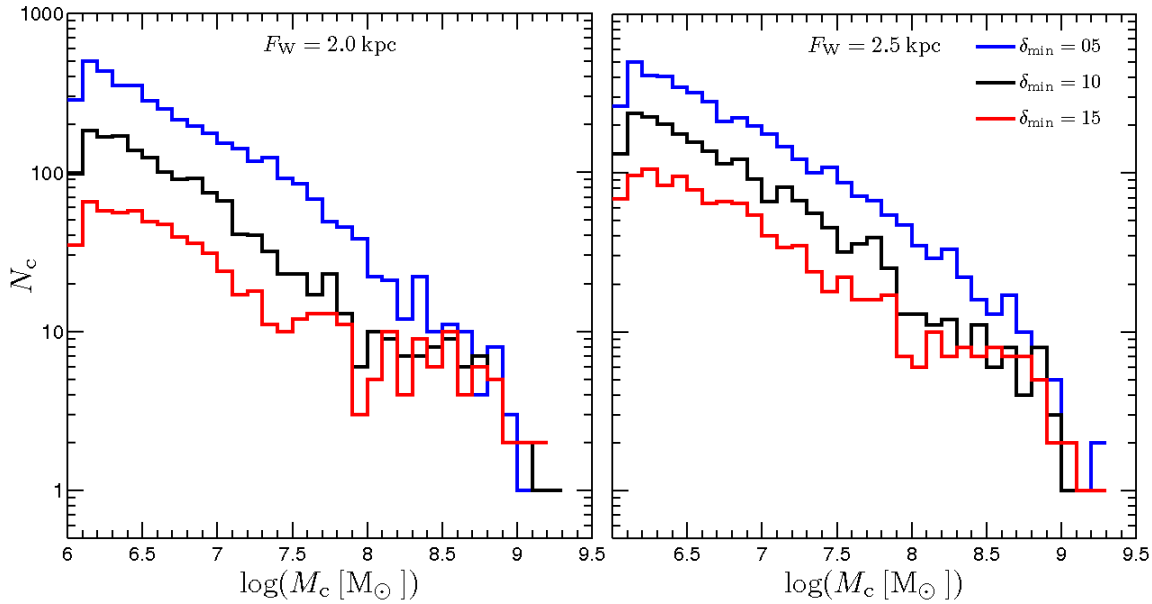


Figure A2. Mass function of in situ clumps in V13 for different combinations of parameters. The X axis shows the clump baryonic mass and the Y axis shows the total number of clumps per logarithmic mass bin. The left (right) panel represents $F_W = 2.0$ (2.5) kpc, and the blue, black and red lines represent $\delta_\rho^{\text{min}} = 5, 10,$ and 15 respectively. The high-end of the mass function is insensitive to changes in the range $F_W = 2 - 2.5$ kpc, $\delta_\rho^{\text{min}} = 10 - 15$, but a value of $\delta_\rho^{\text{min}} = 5$ changes both the slope and the normalization. At the low-mass end, decreasing δ_ρ^{min} or increasing F_W results in more low-mass, low-density clumps, but does not change the slope of the mass function.

2016) target UV bright clumps. Guo et al. (2015) is perhaps the most directly relatable study to our own. They observed a mass complete sample of several thousand SFGs in the CANDELS/GOODS-S and UDS fields, and used an automated clump finder very similar in spirit to the one used in this work, which detects local overdensities in the galaxy UV luminosity. They defined clumps as objects detected by their algorithm (“blobs”) containing at least 8% of the total galaxy UV luminosity. In order to compare with their results, we must modify our clump selection to mimic the observational bias of UV bright clumps.

Naively, a clump containing 8% of the galaxy UV light should contain $\sim 8\%$ of its SFR. However, clumps in their sample typically had lower dust extinction than the underlying discs, as was also pointed out by Wuyts et al. (2013). Moreover, comparison of the clumps found in this work to clumps found in mock-CANDELS images of our simulations reveals that for bright clumps, with $\gtrsim 5\%$ of the galaxy SFR, the contamination in the observed SFR from nearby sources is $\sim 30\%$, increasing a little towards higher redshift and brighter clumps (Guo et al, in preparation). This motivates selecting clumps with a fractional contribution to the galaxy SFR less than 8%. Comparing our clump SFR function (Fig. 9) to the UV luminosity functions of “blobs” for galaxies in a similar mass and redshift range (figures 7 and 8 from Guo et al. (2015)), we estimate that a threshold of $s = \log(SFR_c/SFR_d) \simeq -1.5$ is a good approximation to the observational selection. In any case, our results are insensitive to changes of $\lesssim 0.2$ dex in this threshold.

This is much higher than the threshold of $s = -3$ that was used in our analysis in §6.2 and §6.3 and it is worth checking how our results might change as a result of this selection.

It turns out that most of our results remain unchanged. The only major change is in the mass gradient. Selecting UV bright clumps introduces a mass gradient for SLCs as well as for LLCs. The clumps with the highest SFR are typically the most massive clumps, so this result suggests that the maximal fragmentation mass increases closer to the disc centre, presumably because of higher velocity dispersions can lead to higher Jeans masses. While a mass complete sample of clumps, as was studied above, avoids this issue, a UV flux (or SFR) limited sample will suffer from it, making the mass gradient a poor indicator of the longevity of clumps. However, all our other results are qualitatively unchanged, and LLCs can still be distinguished from SLCs by their gas fractions, sSFRs and stellar ages.

Fig. B1-Fig. B5 are the same as Fig. 10 - Fig. 16, but only using clumps with $s > -1.5$ rather than $s > -3$. The same mass threshold of $M_c > 10^7 M_\odot$ was used, as this is both our completeness limit for clumps, and roughly matches the lowest observable clump mass. We refer to this as our “observational” sample of clumps.

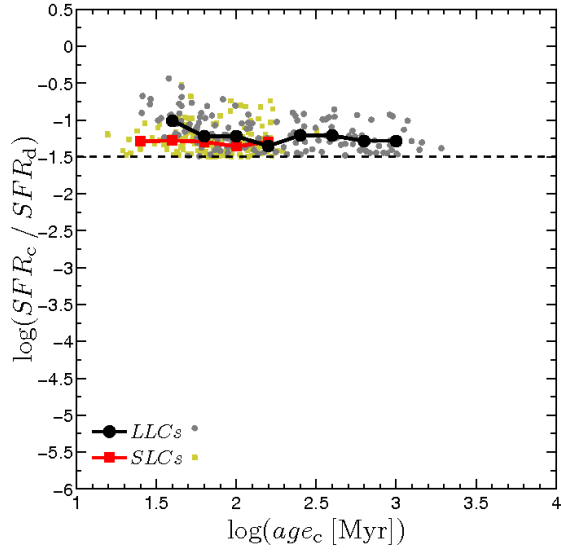


Figure B1. Same as Fig. 10, but using the “observational”, rather than the “clean”, sample of clumps.

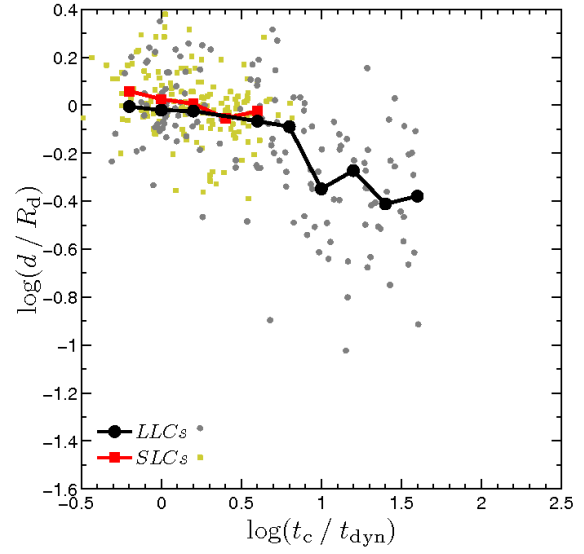


Figure B3. Same as Fig. 12, but using the “observational”, rather than the “clean”, sample of clumps.

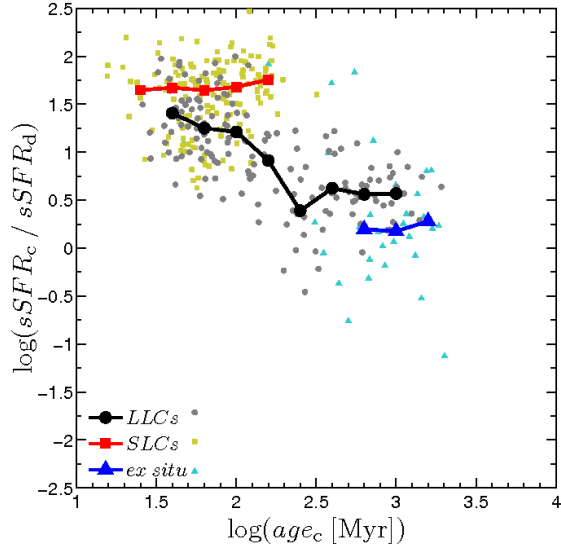


Figure B2. Same as Fig. 11, but using the “observational”, rather than the “clean”, sample of clumps.

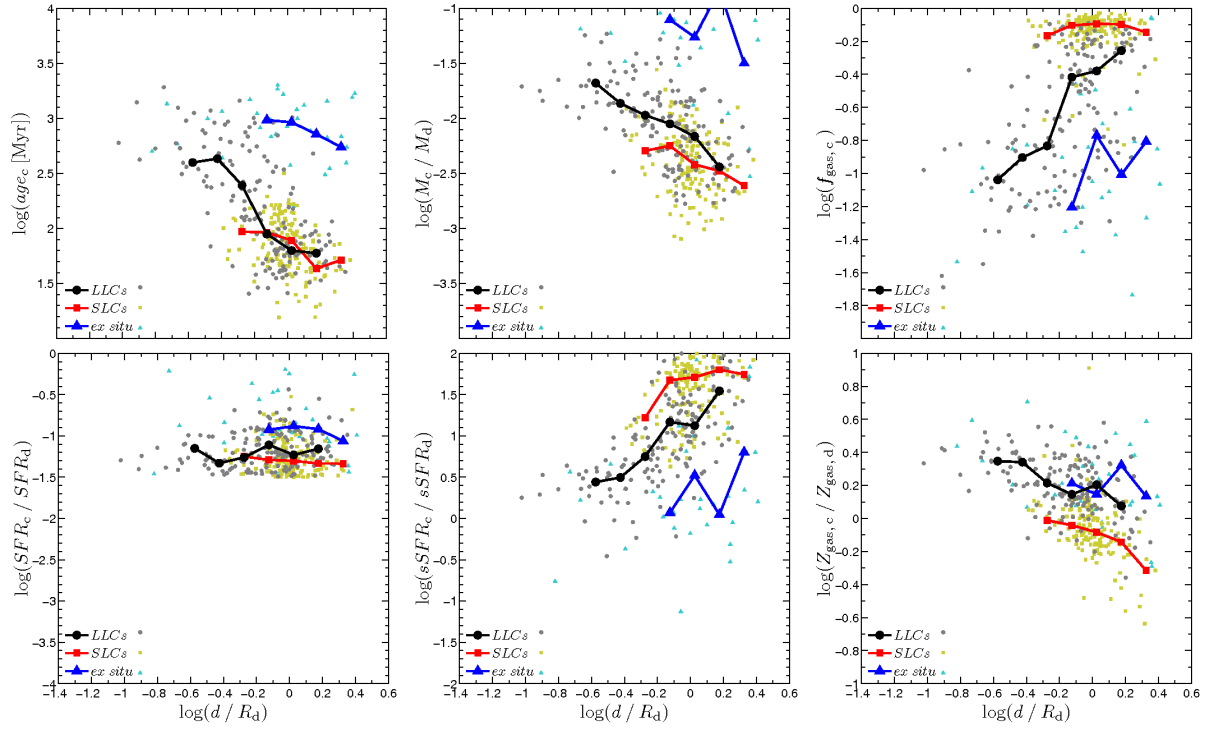


Figure B4. Same as Fig. 15, but using the “observational”, rather than the “clean”, sample of clumps.

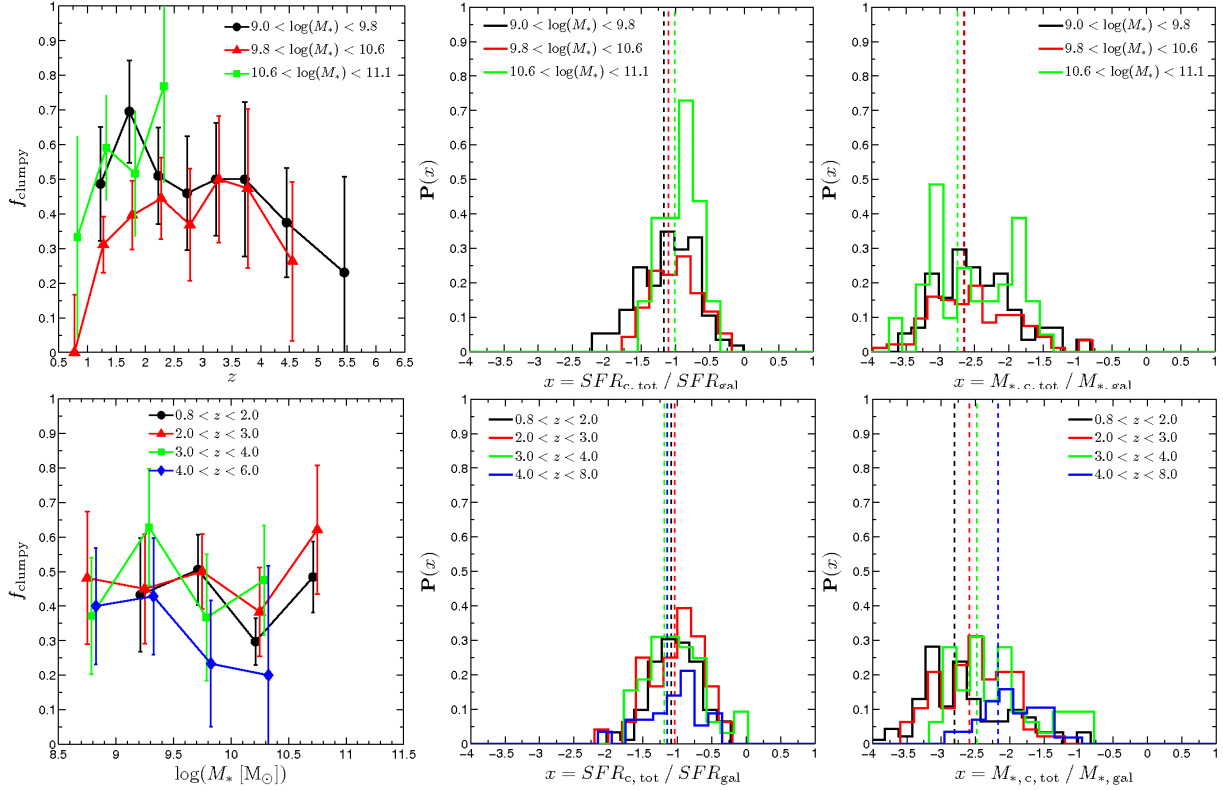


Figure B5. Same as Fig. 16, but using the “observational”, rather than the “clean”, sample of clumps.